Osaka University

Doctoral Thesis

Generation model of laser-driven magnetic field with consideration of warm-dense-matter properties

---

Author:
Hiroki Morita

Supervisor:
Prof. Shinsuke Fujioka

Institute of Laser Engineering
Department of Physics

March 10, 2021

OSAKA UNIVERSITY

Abstract

Graduate School of Science/Department of Physics

Doctor of Science

Generation model of laser-driven magnetic field with consideration of warm-dense-matter properties

by Hiroki MORITA

Magnetic field plays an important role in the fields of cosmic and astrophysical plasma phenomena and laser nuclear fusion study. A lot of researches with respect to a generation of a strong magnetic field for the "magnetized" plasma physics has been carried out. Especially, the method, "laser-driven coil" using high power lasers, can easily supply a strong magnetic field of over 100 T. In recent studies, researchers investigate the magnetized plasma phenomena within such a strong magnetic field by using this laser-driven coil.

In order to magnetize conductive materials such as metals and plasmas sufficiently, a lasting time of the applied magnetic field should be sufficiently longer than a diffusion time of the magnetic field into materials. One has to know the time scale of this magnetic diffusion to realize the sufficient magnetization.

On the other hand, the magnetic field of over 100 T will have a short duration to increase its strength. This intense magnetic pulse causes the induction heating inside the materials and changes the properties of the electric and thermal conduction drastically. The diffusion time of the magnetic field is proportional to the electrical conductivity of a material, thus we have to take into account the temperature dependence of the electrical conductivity in a wide range, 0.01 eV $\sim$ 100 eV to evaluate the magnetic diffusion time. However, a metal is heated up to several eV keeping a solid density during the intense magnetic diffusion. However, a metal heated up to several-eV keeps a solid density during the intense magnetic diffusion. A state that has middle-high temperature and high density is the intermediate state between solid and plasma states known as "*warm dense matter*"(WDM). The theoretical modeling of this state is still limited and also the the experimental data is poor in the WDM regime. Thus we need to evaluate the electrical conductivity based on "*ab-initio*" / "first principle" methods to calculate the magnetic diffusion time exactly.

The goal of this research is to reveal how fast the intense magnetic pulse generated by the laser-driven coil penetrates (diffuses) into a metal sample. In this dissertation, the author mainly investigated the three topics below.

1. Evaluation of electrical conductivity in the WDM regime.

2. Modeling of the laser-driven coil with considering the temporal evolution of the current density distribution and the electrical conductivity at the coil cross-section.

3. Magnetic pulse diffusion into a metal considering the temperature dependence of the electrical conductivity.

At first, the author numerically estimated the temperature dependence of the electrical conductivity in the WDM state. As explained above, the experimental data of the electrical conductivity is not enough and the model describing the WDM conductivity has still been investigated. Thus, in this research, the author used *ab-initio* molecular dynamics simulation which does not require the experimental data to evaluate the electrical conductivity. In addition, the author developed the electromagnetic-field dynamics simulation (EMD) including the heating mechanism which is the basis of this research and analyzes the dynamics of the electromagnetic field taking into account the temperature dependence of the electrical conductivity.

Second, the author modeled the laser-driven coil which is one of the methods to generate a strong magnetic field using the EMD simulation. The temporal evolution of the coil current in laser-driven coils is conventionally modeled on the basis of circuit equations. The author applied the EMD simulation to it and developed a model that handles the temporal evolution of the current density distribution and the temporal variation of the electrical conductivity accompanied by Joule heating. This model shows a good agreement with the experimental data compared to the conventional circuit model.

Finally, the author estimated numerically the magnetic pulse penetration into the metal in the generation process by the laser-driven coil, the resulting induction heating and change of the conductivity. The process of the magnetic diffusion plays an important role in the research regarding the nuclear fusion with assistance of strong magnetic fields. In recent studies of the laser fusion with the fast ignition scheme, a method is planned to improve the heating efficiency of the fuel plasma with application of the strong magnetic field generated by the laser-driven coil. To realize this method with the strong magnetic field, the magnetic field must magnetize the fuel plasma sufficiently within its lasting time. In the method improving the heating efficiency, the numerical evaluation of the pulsed magnetic diffusion which is tough to measure directly will promote the simulation modeling the realistic circumstance closer to the experiments, designing the principle-realization experiments, and analysis of the experimental results. This research will also contribute to the research area investigating the magnetized plasma with a laser-driven coil, not only the fusion research, but the cosmic and astrophysical phenomena.

Acknowledgements

First of all, I would like to express my appreciation and thanks to my supervisor, Prof. S. Fujioka, for his support of my Ph.D. related research and his guidance in helping me in writing this thesis. I also would like to thank the committee members of this thesis, Prof. M. Aoki, Prof. Y. Sentoku, Prof. M. Nakai, and Dr. Y. Arikawa, for the comments and suggestions during the defense. I am glad that I could do my research in the Institute of Laser Engineering (ILE), a facility with state-of-the-art intense lasers LFEX and GEKKO-XII. I would like to give special thanks to Prof. R. Kodama and Prof. Azechi, as director and former director of ILE.

I would like to thank Prof. N. Sato who provides me a lot of opportunities to acquire a broad perspective and rich academic knowledge through the Osaka University Honors Program for Graduate Schools in Science.

This work was supported by Grant-in-Aid for JSPS Research Fellow (No. 20J10496) from the Japan Society for the Promotion of Science.

I would like to thank Dr. F. Graziani (LLNL), Dr. T. Ogitsu (LLNL), Dr. S. Hu (Univ. Rochester, LLE) for their support and advice on the ab-initio molecular dynamics simulation work. The work in Chapter 2 was supported by the Osaka University Scholarship for Overseas Research Activities 2018, and Japan / U.S. Cooperation in Fusion Research and Development. I wish to thank the High Energy Density Science Center at Lawrence Livermore National Laboratory for hosting H. Morita on the Quartz Supercomputer where portions of this research were done. This material is based upon work partially supported by the Department of Energy National Nuclear Security Administration under Award Number DE-NA0003856, the University of Rochester, and the New York State Energy Research and Development Authority.

I would like to thank Dr. J. D. Moody (LLNL), Dr. B. B. Pollock (LLNL), Dr, C. S. Goyon (LLNL), Dr. G. J. Williams (LLNL), Dr. V. Tikhonchuk (CELIA) for their support and advice on the experiments, analysis, and simulation regarding B-field generation experiments at OMEGA-EP facility, and the technical support staff of the Laboratory for Laser Energetics at the University of Rochester for assistance with OMEGA-EP. The work in Chapter 3 was performed under the auspices of the U.S. Department of Energy by Lawrence Livermore National Laboratory under Contract DE-AC52-07NA27344. This work was partially supported by Japan/U.S. Cooperation in Fusion Research and Development, the Collaboration Research Program between the National Institute for Fusion Science and the Institute of Laser Engineering at Osaka University, and the Osaka University Scholarship for Overseas Research Activities 2018, KAKENHI (Grants Nos. 15KK0163, 16K13918, and 16H02245), the Matsuo Research Foundation, and the Research Foundation for Opto-Science and Technology.

I would like to thank Dr. A. Sunahara (Univ. Purdue) for their support and advice on the conductivity model and development of the electromagnetic simulation code, and the technical support staff of ILE at Osaka University for assistance with

the computer simulations. The work in Chapter 4 supported by the Collaboration Research Program between the National Institute for Fusion Science and the Institute of Laser Engineering at Osaka University (NIFS12KUGK057, NIFS15KUGK087, NIFS17KUGK111 and NIFS18KUGK118), and by the Japanese Ministry of Education, Science, Sports, and Culture through Grants-in-Aid, KAKENHI (Grants No. 15KK0163, 16K13918, and 16H02245).

I would like to thank A. Arefiev (Univ. California, San Diego), J. J. Santos (Univ. Bordeaux), T. Toncian (HZDR), A. Yogo, A. Morace for their support and advice on the experiments, analysis, and simulation regarding proton acceleration experiments at GXII-LFEX facility, and the technical support staff of ILE at Osaka University for assistance with the laser operation, target fabrication, and plasma diagnostics. The work in Chapter A was supported through Collaboration Research Programs by the Institute of Laser Engineering at Osaka University (Grant Nos. 2018A1-Arefiev and 2019A1-Arefiev) and the Collaboration Research Program between the National Institute for Fusion Science and ILE (NIFS12KUGK057, NIFS15KUGK087, NIFS17KUGK111, and NIFS18KUGK118), the Japanese Ministry of Education, Science, Sports and Culture through Grants-in-Aid, the Osaka University Scholarship for Overseas Research Activities 2018, the DOE Office of Science under Grant No. DE-SC0018312, KAKENHI (Grant Nos. 15KK0163, 16K13918, and 16H02245) and the Matsuo Research Foundation and Research Foundation for Opto-Science and Technology.

I would like to thank Prof. T. Jhozaki, Prof. Y. Mori, Prof. T. Sano, Prof. K. Shigemori, Prof. Y. Sakawa for their support and advice throughout all researches in this dissertation and my living in ILE.

Also, I would like to express my gratitude to Dr. N. Tanaka, Dr. S. Kojima, Dr. Y. Abe, Dr. S. Sakata, Dr. Y. Iwasa, Dr. T. Shiroto, Dr. H. Kato, Dr. S. Lee, Dr. H. Li, Dr. B. Zhu, Dr. K.Law, Dr. K. Matsuo, Dr. C. Liu, Mr. R. Takizawa, Ms. M. Takemura, Mr. S. Guo, Mr. J. Dun, Mr. H. Kishimoto, Mr. S. Kambayashi, Mr. Y. Ochiai, Mr. J. Nishibata, Mr. M. Ota, Mr. S. Egashira, Mr. D. Golovin, Mr. T. Mori, Mr. S. Shokita, Mr. N. Kamitsukasa, Mr. S. Matsubara, Mr. A. Yao, Mr. Y. Fukuyama for their friendliness and kindness.

Finally, I would like to thank my parents for their support and encouragement.

Contents

Chapter 1

Introduction

1.1 Generation of Strong Magnetic Field

The high-energy-density-plasma (HEDP) fields are investigated by using pico- and nano-second high power lasers. Recently a technique of generation of a strong magnetic field over 100 T evolves, as a result, various studies on the magnetized-HEDP physics are recently progressed with a strong magnetic field. Here we introduce some techniques of a strong B-field generation.

Various studies on the generation of a magnetic field in a steady and non-destructive manner have been conducted, and now a magnetic field of above 10 T can be stably supplied. These magnetic fields are usually applied to researches regarding condensed matter and astrophysical plasma. The steady magnet can now supply the magnetic field of 45 T at maximum. This magnet was achieved by a hybrid magnet that combines a superconducting magnet and a water-cooled magnet. The maximum magnetic field that can be generated by a superconducting magnet alone is limited to about 20 T due to the superconducting-paramagnetic transition in a strong magnetic field. In addition, the maximum magnetic field that can be generated by a water-cooled magnet alone is limited to financial problems, and the realized one is about 30 T. By using these magnets at the same time, the current 45 T was achieved[1)]. In addition, research and development of coils and wires that can withstand the Lorentz force due to the discharge current of the capacitor bank generated a non-destructive magnetic field of up to 80 T for several milliseconds[2)].

On the other hand, the strong magnetic field of over 100 T is an intensive pulse and accompanies with the destruction of the source. In addition, the pulse duration tends to be short to increase the magnetic-field strength as shown in Fig. 1.1. Here, we introduce some methods of generation of a magnetic field of over 100 T.

The compression method, one of the methods to generate a strong magnetic field, is often used in the fields of the condensed matter physics. A conductor tends to capture lines of magnetic field as explained later. Thus, when a conductor is compressed, the magnetic field captured in a conductor is also compressed, generating a strong magnetic field. There are several methods to compress the conductor using a bomb, pinching effect, high power laser, and so on. In a bomb implosion, the magnetic field of 2800 T lasting 2 μs was generated with 200-kg TNT (corresponding to 4 MJ)[3)],

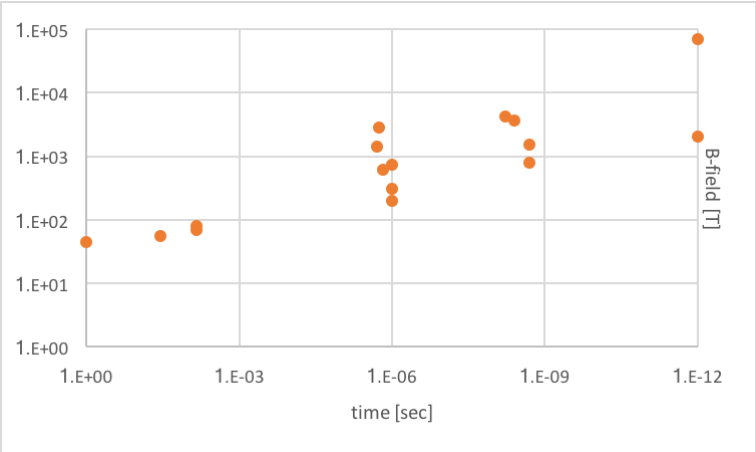

FIGURE 1.1: Relation of magnetic field strength and pulse duration. The pulse duration tends to short as the magnetic field becomes intense. Magnetic field of below 100 T is created by a non-destructive coil, and above 100 T is created by a destructive one.

but the bomb blew the facility off; it cannot be used for the condensed matter experiments. The maximum strength is limited to 1000 T for the physical experiments in this facility.

In the electromagnetic compression, lines of magnetic field are compressed via z- or θ pinching effects which occurs when a large current flows suddenly. This large current is often generated with the discharging of a large capacitor bank. In a famous method, for example, a single-turn coil has a metallic cylinder called as "*liner*" inside a coil as shown in Fig. 1.2(a). The pulsed magnetic field triggers the mutual induction in the liner; the liner is pushed inward by the Lorentz force. Accompanied by the liner pinching, the generated magnetic field is also compressed (θ-pinching), resulting in the strong field. Using this technique, the maximum strength of 710 T was achieved during 1 μs[4]. In addition, z-pinching gas puff, the maximum strength of 4 kT was recorded during 5 ns at Sandia National Laboratory[5].

In the laser implosion method, the magnetic flux can be compressed by a terrawatt high-power laser. The compressed material is usually plastic. Plastic is an insulator at room temperature, but becomes high-conductive material once ionized. Also, it can be compressed easily because of low density, resulting in strong magnetic compression. Compressing a plastic cylinder via the laser implosion method, the maximum magnetic field of 4 kT was generated during 1 ns[6].

In recent studies, a method to generate a strong magnetic field of < 100 T has been developed at large-scale laser facilities without any compression; the maximum magnetic field of 600-1500 T was generated by using the laser-driven coil that consists of two plates connected with a wire as shown in Fig. 1.2(b)[7, 8, 9]. After this report, a lot of researches regarding the magnetized HED physics have been investigated with the laser-driven coil target. However, the generation mechanism of such a strong field with the laser-driven coil is not completely understood yet because the experimental data are still poor. Thus, experimental and theoretical studies are investigated to

model the laser-driven coil which agrees with the experimental data[10),11),12)]. In the experimental works, the magnetic field has been generated with various conditions, and the dependences of the laser-intensity, laser-frequency, and pulse duration, have been investigated. Also, the physical properties have been measured such as the temporal evolution of the generated magnetic field, the plasma motion between the plates. The laser-driven coil is basically modeled with a lumped circuit element model considering the plasma expansion due to the laser-irradiation. The difficulty in this modeling is a treatment of the plasma expansion and the resistance variation due to Joule heating; these points have been investigated theoretically. Besides, the generation of stronger-field exceeding 10 kT is challenged by compressing the magnetic field generated with the laser-driven coil as seed field.

Korneev *et al.* predicted numerically that a strong magnetic field exceeding 20 kT would be generated when the intense laser ($> 10^{18}$ W/cm^2) irradiates the inner surface of an escargot-like micro-coil as shown in Fig. 1.2(c). The generated magnetic field forms an anti-parallel structure, resulting in a relativistic magnetic reconnection and particle acceleration accompanied with it. The experiment based on this concept was performed and the maximum magnetic field of 2.1 kT was observed within 1-ps duration by using the escargot-like micro coil[13)]. The laser-irradiated micro coil emits the energetic particles due to the relativistic magnetic reconnection. This experimental research helps the understanding of astrophysical phenomena such as galactic x-ray emission from the acceleration disk of black hole systems. The mechanism of magnetic field generation on this kind of coil is also not completely understood and is still investigated.

Besides, it was reported that the self-generated magnetic field of 70 kT was measured experimentally on a target surface irradiated by the intense laser[14)], but it seems tough to apply this self-generated magnetic field to the HED experiments.

1.2 Magnetized High-Energy-Density-Plasma Physics

The strong magnetic field plays an important role in a field of plasma physics and fusion sciences. The generation of strong magnetic field has been investigated and improved, then one can now test, observe, and investigate the "magnetized" plasma phenomena experimentally that have not been observed so far. For these motivations, magnetized plasma physics is an active area of research in the field of high-energy-density (HED) science. Here we introduce some of the interesting studies.

The collisional frequency of an ideal plasma is roughly calculated as

$$\nu_{ei} = 2.7 \times 10^{-10} \frac{n_e[\mathrm{cm}^3]}{T[\mathrm{keV}]^{1.5}} \ [\mathrm{sec}^{-1}]. \tag{1.1}$$

In studies of cosmic and astrophysical plasma, the temperature and density of the generated plasma are $10 < T < 100$ eV and $10^{17} < n_e < 10^{19}$ cm^{-3}, respectively[15, 16, 17, 18, 19)], and thus the collisional frequency can be estimated about $1 \sim 10 \times 10^{-10}$ sec^{-1}.

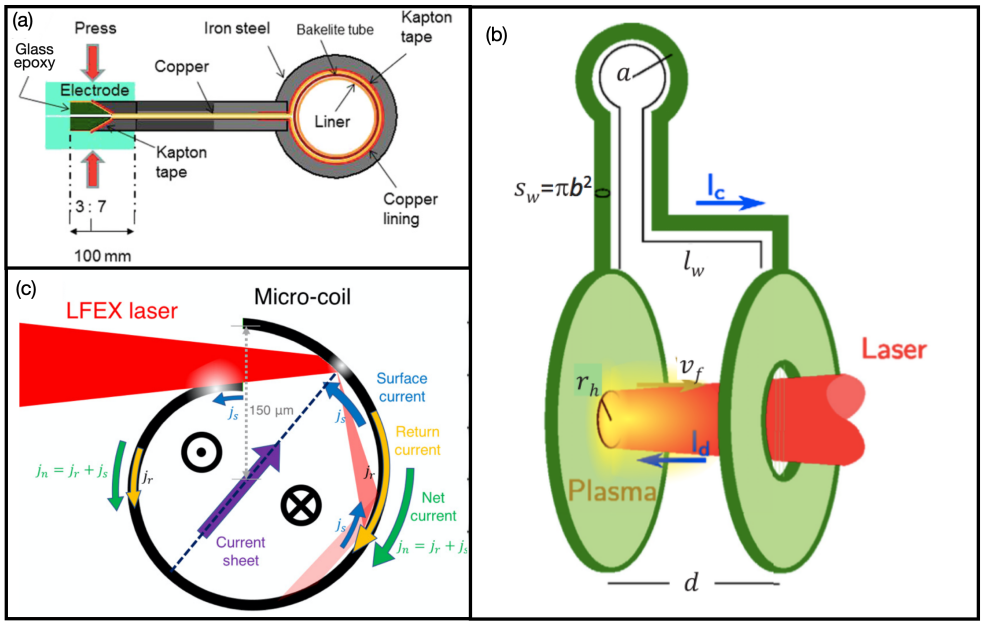

FIGURE 1.2: Three types of coils which can generate a magnetic field of above 100 T. (a) Magnetic compression coil can produce a magnetic field of about 1 kT by compressing a seed magnetic field of $\sim$ 10 T[4]. (b) Laser-driven coil can produce a magnetic field of 100-1000 T with a large potential gap due to the laser-irradiation.[12] (c) Escargot-like micro-coil can produce the anti-parallel magnetic field with electron flow and return current generated by the intense laser-irradiation.[13]

When the magnetic field of $\sim$ 10 T is applied to this plasma, the electron cyclotron frequency becomes greater than the plasma collisional frequency, and the plasma is sufficiently magnetized. On the other hand, in terms of the HED plasma such as cores of stars and planets, and fusion fuel of inertial confinement fusion, the plasma density and temperature are 1 keV $< T$ and 10^{21} cm$^{-3} < n_e$, respectively. Under the magnetic field of $\sim$ 100 T, the collisional frequency of this plasma and the electron cyclotron frequency (eB/m_e) become comparable ($\omega_c\tau \sim 1$). Then, for example, the thermal transport that is generally explained by the thermal diffusion of electrons is suppressed in a direction crossing the lines of magnetic field. This non-isotropic thermal conduction has been investigated computationally and theoretically, and this was verified experimentally in 2017[20]. In a central ignition scheme of inertial confinement fusion (ICF), Perkins *et al.* revealed that a strong magnetic field of 100 T would mitigate the thermal conduction across the magnetic field, resulting in the ion temperature to 36 keV on a scale of National Ignition Facility (NIF)[21].

Higher-strength $\sim$ 1 kT, magnetic field affects to a relativistic electron beam. The relativistic electrons splay with a large angle as the laser intensity increases[22, 23]. Cai *et al.* reported a simulation work (likely particle-fluid hybrid) that an external magnetic field of 1 kT suppresses the beam divergence of relativistic electrons accelerated by laser irradiation[24]. This splaying of relativistic electrons was a problem for the inertial confinement fusion study; in a fast ignition scheme, the relativistic electrons interact with a fuel plasma. In 2015 Johzaki *et al.* investigated a combination study

of a fast ignition with a strong magnetic field[25], and revealed that the ion temperature increases up to 5 keV using the full simulation that includes the compression of a magnetic flux, the beam transport, and the core heating[26]. Following these numerical study, Sakata *et al.* achieved the electron temperature of 2 keV using a laser-driven coil which potentially generates a magnetic field above 1 kT[27, 28].

The beam controlling by a strong magnetic field also provides a benefit to development of the high-energy-ion-beam source. A high-intensity laser ($> 10^{18}$ W/cm^2) interacts with a thin foil target, resulting in a high energy ion beam. Once electrons in the foil are accelerated by the laser-irradiation, electrons propagate through the foil, and generate a strong electric field ($\sim$ 1 GV/m) at a rear surface of the foil due to a charge separation[29, 30, 31]; this strong "*sheath*" electric field accelerates ions of contamination on a rear surface. This mechanism is well-known as target-normal-sheath-acceleration (TNSA). A strong magnetic field can confine the electrons in a lateral direction as explained above, consequently, the sheath field is enhanced to accelerate protons to high energy. This concept was proved with a particle-in-cell simulation[32].

Also in 1-kT magnetic field, a relativistic magnetic reconnection can be observed. The electron density of astrophysical plasma is $10^{17} \sim 10^{19}$ cm^{-3}. For the plasma of this density range, the Alfven velocity, $v_A = c(1 + (c/B)^2 \rho\mu)^{-0.5}$, which is a velocity of the longitudinal and transverse magnetic waves becomes comparable to the speed of light under the magnetic field of 1 kT. The relativistic reconnection has been investigated with such a strong field[33, 13].

A magnetic field becomes to affect to laser propagation at a strength above 10 kT. In a fundamental plasma physics, laser-light is reflected at a plane where a plasma density is equal to a critical density $\varepsilon_0 m_e/e^2\ \omega_L^2$, but a whistler mode is transparent to a magnetized plasma even its density is over critical one, where the whistler mode is a right-hand circular-polarized wave whose frequency is less than an electron cyclotron frequency (eB/m_e). A laser wavelength is generally 1053 nm (2.84×10^{14} Hz) because glass is often used for high power laser facilities. The electron cyclotron frequency in a magnetized plasma exceeds the laser frequency in the existence of a 10-kT magnetic field. Then, the laser can propagate in plasma as a whistler mode[34),35].

For other stuff, tiny electron Larmor radius causes some characteristic "quantum mechanical" phenomena such as non-linear Zeemann effect, Paschen-Back effect, Harper Broadening effect etc in a strong field[36, 37].

1.3 Magnetized Fast Ignition in inertial confinement fusion

It is the inertial-confinement-fusion (ICF) research that the most important topic in HEDP research explained above is. In ICF, the high density and temperature state is created within a short confinement time-scale by imploding the fuel with high-power laser. History and details of various ICF researches are summarized in Ref[38]. Here,

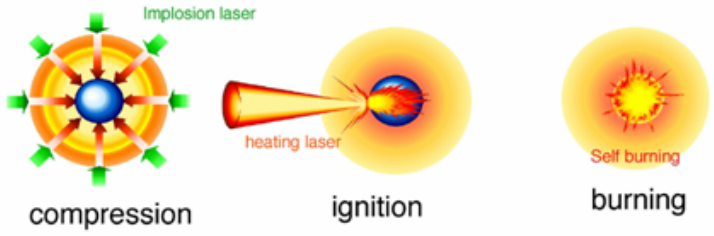

FIGURE 1.3: Basic concept of fast ignition introduced by [LANL]. In laser-driven fast ignition, the target is compressed to high density with a low implosion velocity and then ignited by a short, high-energy pulse of electrons or ions induced by a very short (a few picoseconds), high-power laser pulse.

we roughly introduce one of a ignition scheme – fast ignition[39] which is strongly related with this thesis.

The fast ignition scheme can be simply illustrated with three steps shown in Fig.1.3. In the compression phase, a fusion fuel is compressed to high-density state by the high-power laser irradiation. Following, in the ignition phase, the heating laser is irradiated to the compressed fuel and laser-accelerated high-energy electron or ions deposit their energy to the fuel core. Once the ignition condition is achieved, the fusion reaction takes place spontaneously, and enters to burning phase.

In the compression phase, ablation plasma is generated around the fuel due to the laser irradiation and might spoil the efficient fuel heating because the heating laser is possible absorbed and reflected in this ablation plasma. Thus, in the fast ignition scheme, a gold cone is attached to a spherical fusion fuel to exclude ablated plasma from the path of the heating laser pulse to the fuel as shown in Fig. 1.4[40, 41, 42]. A high-Z dense cone is required to prevent the cone wall from breaking by the ablated plasma and preheating caused by radiation and hot electrons. Relativistic laser-plasma interactions at the cone tip efficiently produce REB with average kinetic energy of >0.511 MeV[43, 44]. The laser-produced REB typically has a large full divergence angle of 100°[22], and this reduces energy coupling from the heating laser to the fuel core because a small portion of the diverged REB collides with the small fuel core.

Guidance of the diverging REB to the small fuel core is essential to demonstrate efficient fast-ignition. Application of a strong magnetic field to the REB generation and transport regions has been proposed by several authors[45, 24, 46, 25], and this scheme is referred to as magnetized fast ignition (MFI). A proof-of-principle experiment of the MFI scheme was conducted at the GEKKO-XII and LFEX facilities using a laser-driven coil, and efficient core heating was achieved[27, 28].

However, to improve the heating efficiency with the externally-applied magnetic field, the magnetic field must diffuse into the REB generation zone and REB transport region before producing the REB. In other ward, a lasting time of an applied magnetic

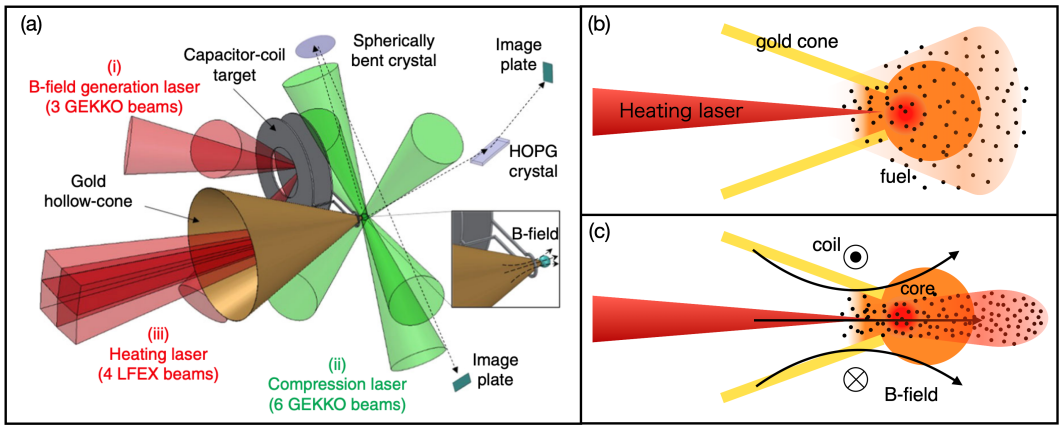

FIGURE 1.4: Basic concept of magnetized fast ignition. (a) Experimental setup of MFI experiments performed by Sakata *et al.*[27]. (b) Simple illustration of REB transport. (c) Simple illustration of REB guiding by magnetic field.

field should be longer than a diffusion time of the magnetic field into the guiding-cone. One has to know time-scale of this magnetic diffusion to realize the sufficient magnetization.

1.4 Magnetic diffusion

Here, we introduce a fundamental theory of the magnetic diffusion in conductive material, and estimate the diffusion time-scale of the applied magnetic pulse into conductive materials.

In magneto-hydro dynamics (MHD), a magnetic field is usually described as following induction equation.

$$\frac{\partial \vec{B}}{\partial t}(\vec{x},t) = \frac{1}{\mu_0 \sigma}\vec{\nabla}^2 \vec{B}(\vec{x},t) + \vec{\nabla} \times (\vec{v} \times \vec{B}(\vec{x},t)) \tag{1.2}$$

The first term of this equation represents magnetic diffusion, and the second term represents the advection of a magnetic flux. In terms of imploded and ablated plasma that moves fast, the advection term is dominant, thus the equation becomes

$$\frac{\partial \vec{B}}{\partial t}(\vec{x},t) = \vec{\nabla} \times (\vec{v} \times \vec{B}(\vec{x},t)) \tag{1.3}$$

neglecting the first diffusion term. This equation describes "Frozen-in", namely the advection of the magnetic flux with a motion of plasma. This is the principle of the magnetic compression explained above. For the resistive and slow plasmas, the magnetic flux are not completely frozen-in.

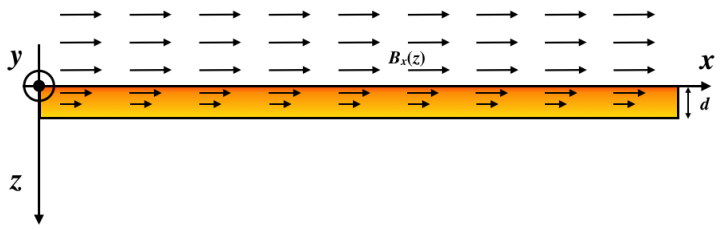

FIGURE 1.5: Simple illustration of magnetic diffusion. The infinity-wide conductive plate, whose thickness is d, is placed on x-y plane. A magnetic field is applied in x-direction outside of the conductor $0 < z$. This magnetic field causes eddy current in y-direction and diffuses into the conductive plate with causing the induction heating.

On the other hand, our study treats solid metal, thus the second advection term is negligible. In that case, (1.2) can be reduced to

$$\frac{\partial \vec{B}}{\partial t}(\vec{x}, t) = \frac{1}{\mu_0 \sigma} \vec{\nabla}^2 \vec{B}(\vec{x}, t). \tag{1.4}$$

This is the diffusion equation for the magnetic field. The diffusion time scale can be estimated from this equation. For instance, the magnetic field takes a time, $\mu_0 \sigma L^2$, to penetrate (soak-in) the conductor which has a thickness, L, and the conductivity, σ. For hollow cylinder geometry, the diffusion equation can be re-written as

$$\frac{\partial \vec{B}}{\partial t}(\vec{x}, t) = \frac{2}{\mu_0 \sigma a} \vec{\nabla} \times \vec{B}(\vec{x}, t), \tag{1.5}$$

where a is a cylinder radius. In this case, the magnetic field takes a time, $\mu_0 \sigma a L/2$, to penetrate (soak-in) the hollow cylindrical conductor which has a thickness, L. If the metal has a thickness of 10 μm and the conductivity of 10^7 S/m, the magnetic diffusion time is 1 ns. Once the conductivity drops an order, the diffusion time also drops and becomes 100 ps. The magnetic diffusion strongly depends on the electrical conductivity.

1.5 Effect of induction heating

The intense magnetic pulse such as laser-generated magnetic field would cause the induction heating in the conductor. We need to consider the temperature dependence of the electrical conductivity carefully to estimate the magnetic diffusion time. Here, we estimate how much the temperature increases in metal through the induction heating when the magnetic pulse is applied.

Assume that a parallel magnetic field in the x-direction is applied to the only outside ($z < 0$) of the conductor whose thickness is d as shown in Fig. 1.5. The high-frequency modes of this pulse magnetic field contribute the induction heating,

thus we just consider a mode of B_x [A/m s] expressed as

$$B_x(z;\omega) = b(z)e^{-i\omega t} = B(\omega)e^{-z/\delta(\omega)}e^{-i\omega t}. \tag{1.6}$$

To estimate the temperature increase, we can take the time-average of this mode as follow.

$$\bar{B}_x(z;\omega) = \frac{1}{\sqrt{2}}B(\omega)e^{-z/\delta(\omega)} \tag{1.7}$$

When the magnetic pulse is the Gaussian pulse having FWHM, τ, a mode of magnetic pulse, $B(\omega)$ [A/m s], is expressed as

$$\begin{aligned} B(\omega) &= B_0\tau\left(\tfrac{\pi}{4\ln(2)}\right)^{1/2}e^{-\frac{(\omega\tau)^2}{16\ln(2)}} \\ &= B_0\sqrt{4\pi A}e^{-A\omega^2}, \end{aligned} \tag{1.8}$$

where, $A = \tau^2/16\ln(2)$, and B_0 corresponds to a peak value of the magnetic pulse. Inside a conductor ($z < 0$), a mode of current density, $j_y(\omega)$ [A/m^2 s], is obtained from the Ampere's low.

$$\frac{1}{\mu_0}\frac{\bar{B}(\omega)}{\delta(\omega)}e^{-z/\delta(\omega)} \tag{1.9}$$

Besides, a mode of electric field, $E_y(\omega)$ [V/m s], can be obtained from Ohm's low.

$$\frac{1}{2}\omega\delta(\omega)\bar{B}(\omega)e^{-z/\delta(\omega)} \tag{1.10}$$

Using the equations (1.9) and (1.10), the current density, j_y [A/m], and the electric field, E_y [V/m], inside the conductor are expressed as follows.

$$j_y = \frac{1}{\mu_0}B_0\sqrt{4\pi A}\sqrt{\frac{\mu_0\sigma}{2}}\int_0^\infty \mathrm{d}\omega\ \sqrt{\omega}e^{-\alpha\sqrt{\omega}}e^{-A\omega^2} \tag{1.11}$$

$$E_y = \frac{1}{2}B_0\sqrt{4\pi A}\sqrt{\frac{2}{\mu_0\sigma}}\int_0^\infty \mathrm{d}\omega\ \sqrt{\omega}e^{-\alpha\sqrt{\omega}}e^{-A\omega^2} \tag{1.12}$$

Here, we replaced a depth z to a thickness d, and $\tau_{\mathrm{dif}} \equiv \mu_0\sigma d^2/2$, $\alpha = \sqrt{\tau_{\mathrm{dif}}}$. From these equations, the induction heating, $\vec{j}\cdot\vec{E}$ [W/m^3], accompanied with the magnetic diffusion can be expressed as

$$4\pi A\frac{B_0^2}{2\mu_0}\left(\int_0^\infty \mathrm{d}\omega\ \sqrt{\omega}e^{-\alpha\sqrt{\omega}}e^{-A\omega^2}\right)^2. \tag{1.13}$$

The integral in parentheses cannot be calculated analytically, so we expand $e^{-\alpha\sqrt{\omega}}$ as series as

$$e^{-\alpha\sqrt{\omega}} \sim \sum_n \frac{(-\alpha)^n}{n!}\omega^{n/2}. \tag{1.14}$$

Then, the integral can be written as

$$\sum_n \frac{(-\alpha)^n}{n!}\int_0^\infty \mathrm{d}\omega\ \omega^{(n+1)/2}e^{-A\omega^2}. \tag{1.15}$$

In terms of this integral, we can apply the following formula.

$$\int_0^\infty \mathrm{d}x\ x^{2k+1}e^{-ax^2} = \frac{\Gamma(k+1)}{2a^{k+1}} \tag{1.16}$$

where, $\Gamma(x)$ is the gamma function. Replacing as $k = (n-1)/4$, (1.13) is expressed as

$$\begin{aligned} & 4\pi A\frac{1}{2\mu_0}B_0^2\left(\sum_n \frac{(-\alpha)^n}{n!}\frac{\Gamma\big((n+3)/4\big)}{2A^{(n+3)/4}}\right)^2 \\ = \ & \frac{4\pi}{\tau}\frac{B_0^2}{2\mu_0}\left(\sum_n \frac{(-1)^n}{n!}\Gamma\Big(\frac{n+3}{4}\Big)\big(\ln(2)\big)^{(n+1)/4}\Big(\frac{\tau_{\mathrm{dif}}}{\tau}\Big)^{n/2}\right)^2 \end{aligned} \tag{1.17}$$

Neglecting the thermal diffusion effect, we can obtain the temperature increase as follow.

$$\begin{aligned} \Delta T &= \frac{4\pi}{c_{\mathrm{V}}\rho}\frac{B_0^2}{2\mu_0}\left(\sum_n \frac{(-1)^n}{n!}\Gamma\Big(\frac{n+3}{4}\Big)\big(\ln(2)\big)^{(n+1)/4}\Big(\frac{\tau_{\mathrm{dif}}}{\tau}\Big)^{n/2}\right)^2 \\ &= \frac{1}{c_{\mathrm{V}}\rho}\frac{B_0^2}{2\mu_0}\left(\sum_n C_n\Big(\frac{\tau_{\mathrm{dif}}}{\tau}\Big)^{n/2}\right)^2 \end{aligned} \tag{1.18}$$

The series expansion of C_n in (1.18) naturally gives accurate value with the high-order expansion. Here, we introduce a fitting function of the high-order expansion:

$$\left(\sum_n C_n\Big(\frac{\tau_{\mathrm{dif}}}{\tau}\Big)^{n/2}\right)^2 \approx 5\pi\frac{e^{-(\tau_{\mathrm{dif}}/\tau)^{0.36}}}{1+0.51(\tau_{\mathrm{dif}}/\tau)} \tag{1.19}$$

We finally get the approximated temperature increase as

$$\Delta T \approx \frac{1}{c_{\mathrm{V}}\rho}\frac{B_0^2}{2\mu_0}\frac{5\pi e^{-(\tau_{\mathrm{dif}}/\tau)^{0.36}}}{1+0.51(\tau_{\mathrm{dif}}/\tau)}. \tag{1.20}$$

The temperature increase, ΔT, expressed in (1.18) or (1.20) depends on the ratio between the diffusion time and pulse width, τ_{dif}/τ. The function (1.19) is a monotonically increasing function of τ_{dif}/τ. A long pulse (τ_{dif}/τ is small) can heat the conductor for a long time, causing a large temperature increase. On the other hand,

when the diffusion time is long ($\tau_{\rm dif}/\tau$ is large), the applied magnetic field does not soak into the conductor and not heat the inner surface of the conductor much. Also, (1.19) converges to 0 with a large value of $\tau_{\rm dif}/\tau$. This means that the applied magnetic field cannot penetrate the wall thickness, d, during the pulse duration and only heats the surface of the conductor. Consequently, the inner surface is not heated and does not show the temperature increase.

Finally, we estimate the temperature increase of a gold foil as an example. The specific heat and the density of solid gold are 129 J/(K kg) and 19.3 g/cm^3, respectively. When 1-ns Gaussian magnetic pulse of 600 T soaks into 10-μm thick gold, the temperature increase can be calculated to be 1.59 eV (1.85×10^4 K) using (1.20). If the electrical conductivity drops by an order due to this temperature increase, the diffusion time also drops by an order. Then, the estimated temperature increase is 20.7 eV (2.40×10^4 K). Note that the estimations above are just approximation and assumes that the specific heat, electrical conductivity, and density are constant during the heating, thus it should be an overestimation.

A state that has middle-high temperature and density such as solid-dense and several electron-volt is a kind of intermediate state between solid and plasma states known as "warm dense matter" (WDM): the ion-ion interaction and electron degeneracy affect the physical properties in the WDM state. The experimental data are poor in the WDM regime, especially in high-Z and high-dense material such as warm dense gold. The theoretical modeling of the WDM is still challenging work and has been investigated.

1.6 Goal and Outline of this Dissertation

The goal of this research is to reveal how fast the intense magnetic pulse generated by the laser-driven coil penetrates into a metal sample. In previous sections, we showed that the diffusion time-scale of the applied magnetic pulse is proportional to the electrical conductivity, and the conductivity varies over time due to the induction heating accompanied with the magnetic diffusion. Also in terms of the laser-driven coil, a large current heats the conductive wire and varies the coil resistance over time. Therefore, the evaluation of the wide-temperature-range electrical conductivity including WDM regime is a key study in order to estimate how long magnetic pulse generated with a laser-driven coil maintains its strength and how long the magnetic pulse diffuses into the guiding-cone.

The following three topics have mainly been investigated in this research.

1. *ab-initio* evaluation of electrical conductivity in the WDM regime.

2. Modeling of the laser-driven coil with considering the temporal evolution of the current density distribution and the electrical conductivity on the coil cross-section.

3. Magnetic pulse diffusion into a metal considering the temperature dependence of the electrical conductivity.

At first, the author numerically estimated the temperature dependence of the electrical conductivity in the WDM state using *ab-initio* molecular dynamics simulation. In addition, the author developed the electromagnetic-field dynamics simulation (EMD) including the heating mechanism which is the basis of this research and analyzes the dynamics of the electromagnetic field taking into account the temperature dependence of the electrical conductivity. Second, the author developed the "self-consistent circuit model" that handles the temporal evolution of the current density distribution and the temporal variation of the electrical conductivity accompanied by Joule heating with coupling the circuit model with the EMD simulation. Finally, the author estimated numerically the process that the magnetic pulse generated by a laser-driven coil penetrates to the guiding-cone target in the MFI scheme causing inductive heating and changing the conductivity.

This thesis consists of five chapters. This chapter (Chap. 1) introduced briefly the laser-produced high energy density plasma (HEDP) physics and its relation with a strong magnetic field.

Chapter 2 introduces briefly the theoretical models describing the electrical conductivity in the WDM state, and shows the calculation results of the temperature dependence of the electrical conductivity.

Chapter 3 describes the magnetic-field-generation experiments and the modeling of the laser-driven coil which agrees with the experimental data.

Chapter 4 describes the magnetic diffusion into a metal sample considering the temporal evolution of the electrical conductivity due to the induction heating.

Chapter 5 summarizes results in this dissertation, and describes tasks and outlooks in future researches.

In addition, the author investigated a proton acceleration mechanism in the existence of a strong magnetic field, one of the applications of the laser-driven coil. The result of this work is described in Appendix A.

In this research, the estimation of the electrical conductivity is a key topic. There are various models to evaluate the electrical conductivity. Appendix B summarizes the theoretical description of "classical approaches" of the electrical conductivity in WDM.

Chapter 2

Transport Properties of Warm Dense Matter State

2.1 Introduction

Gold has a large atomic number and a high density, as a result it is often used in the fields of the high energy density physics. For example, at some laser facilities such as LULI2000 and OMGEA-EP, a thin gold foil has been used as a source of proton beam via the target normal sheath acceleration mechanism driven by a high-intensity laser[8, 47]. A high-Z gold can make the proton beam high energy and stable rather than using the other materials. As described in Chap. 1, a strong magnetic field of above 1 kT would be able to enhance this TNSA mechanism; as the relativistic electrons are localized by the strong magnetic field, the sheath electric field accelerating the protons is also localized and enhanced, providing higher energetic protons. This concept was numerically investigated[32].

At the OMEGA-EP facility, gold has been used as a material of a laser-driven coil to generate a magnetic field of over 100 T besides a proton beam source[47]. Also at National Ignition Facility (NIF), gold is used as an x-ray radiation source (known as hohlraum target) that implode (compress) the fuel in a central ignition scheme of inertial confinement fusion (ICF). In addition, applying a magnetic field to this ignition scheme is planed at NIF to improve the heating of the fuel plasma: an initially applied magnetic field (seed) is compressed accompanied with the plasma compression, then the compressed magnetic field traps electrons heating the fuel locally, resulting in efficient plasma heating. At GEKKO-XII and LFEX facilities, gold is used as a guiding cone for ICF experiments using the fast ignition scheme. Recently, the efficient heating was achieved by applying a strong magnetic field in this research[27, 28].

The temperature of gold is increased and the properties of a material change in experiments; for instance, a magnetic diffusion into the guiding cone in the magnetized fast ignition (MFI) scheme, and the Joule heating in the laser-driven coil. Under the situation above, gold transitions to the warm dense matter (WDM) state, which is in the solid density and the several eV of high temperature. The treatment of the properties in the WDM state becomes more complex because of the affection of ionic

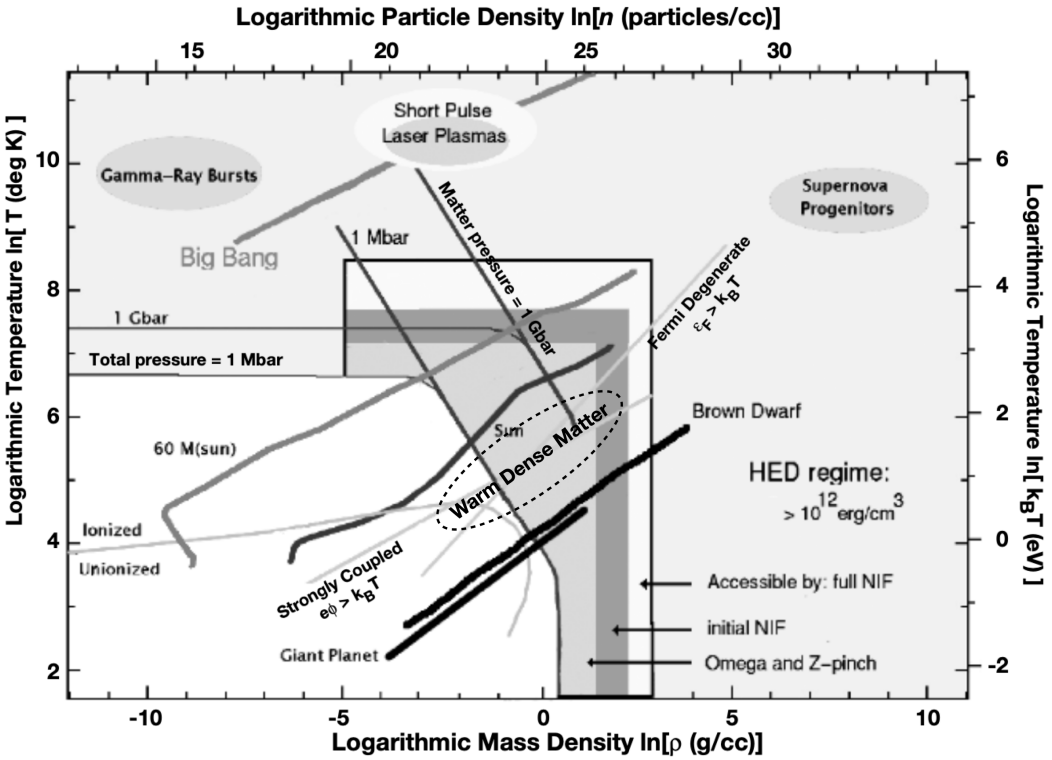

FIGURE 2.1: Temperature-Density phase diagram[48]. The WMD state is placed in the region of 0.1-100 g/cc and 10^4-10^7 K (0.1-10 eV) where the vicinity of the intersection between the degeneracy parameter $\Theta_e = 1$ and the ion coupling parameter $\Gamma_{ii} = 1$.

correlations and electron degeneracy. The transport properties in the WDM state is still a challenging topic, and has been investigated both experimentally and theoretically. The properties of the warm dense gold, especially the electric conductivity, is a key parameter to predict the magnetic diffusion in the magnetized fast ignition, and the time evolution of the current in the laser-driven coil. However, the conductivity at the solid density has not been measured much. The temperature dependence of the conductivity should be required for numerical simulations analyzing the experimental results. So far, the properties of WDM have been investigated; however, the WDM state is not understood completely.

Here we estimated the conductivity of the warm dense gold at the solid density, coupling the *ab-initio* quantum molecular dynamics (QMD) simulation based on the density functional theory (DFT) with the Kubo-Greenwood formula. The results showed that the conductivity of the warm dense gold takes a constant value of 10^6 S/m in the several-eV regime in the temperature.

2.2 Definition of warm dense matter

As noted above, the WDM state is roughly to say the intermediate state between solid and plasma. The WDM is the state that places on the region ranging its density of 0.1-100 g/cm^3 and its temperature of 10^4-10^7 K (0.1-10 eV) as shown in Fig. 2.1. In this

"middle-high density and temperature" region, a dense material is partially ionized; the effects of electron degeneracy and ion coupling arise which has not been seen in an ideal plasma (fully ionized, high temperature and low density). We introduce the WDM state comparing with general plasma theory.

Plasma is often noted as a quasi-neutral gas that exhibits collective behavior and treated with a classical theory, whereas solid metal is treated with a quantum theory. In a solid-state, free electrons are usually degenerated following the Fermi-Dirac distribution because of low temperature ($k_BT/\varepsilon_F \ll 1$). The ions are also Fermi particles, so they should obey the Fermi-Dirac distribution,

$$f(\varepsilon, T) = \frac{1}{1 + e^{(\varepsilon-\mu)/k_BT}} \tag{2.1}$$

On the other hand, system temperature is extremely high ($1 \ll k_BT/\varepsilon_F$) for classical plasma. Thus, the Fermi-Dirac distribution reduces to Boltzmann distribution.

$$f(\varepsilon, T) = e^{-\varepsilon/k_BT} \tag{2.2}$$

The collective behavior is generally a phenomenon that the ionic potential within plasma is canceled out immediately by a surrounding plasma. When a Z_i-fold ion is caused in plasma, surrounding electrons and ions satisfy the following Poisson's equation:

$$\nabla^2\phi(r) = -\frac{1}{\epsilon_0}\Big(+ Ze\delta(r=0) - n_e e \mathrm{e}^{+e\phi(r)/k_BT_e} + n_i(Z_ie)\mathrm{e}^{-(Z_ie)\phi(r)/k_BT_i}\Big) \tag{2.3}$$

The electrons and ions closer to the Z_i-fold ion get strongly influenced by its potential; The potential caused by the Z_i-fold ion would strongly affect a surrounding plasma (electrons and ions) at closer to the ion; however, the affection of the potential to surrounding plasma can be assumed as "weak" far from the ion. Then, the weak-potential approximation, $|e\phi|/k_BT_e,\ |e\phi|/k_BT_i \ll 1$, holds and the Poisson's equation at the far position can be approximated as

$$\nabla^2\phi(r) = \Big(\frac{n_e e^2}{\epsilon_0 k_B T_e} + \frac{n_i(Z_ie)^2}{\epsilon_0 k_B T_i}\Big)\phi(r) \tag{2.4}$$

The solution of this equation can be obtained immediately as follow.

$$\phi(r) = \frac{Ze}{r}\mathrm{e}^{-r/\lambda_D} \tag{2.5}$$

Here,

$$\lambda_D^{-2} = \Big(\frac{n_e e^2}{\epsilon_0 k_B T_e} + \frac{n_i(Z_ie)^2}{\epsilon_0 k_B T_i}\Big) \tag{2.6}$$

is the general Debye length that represents a screening effect of general plasma to the potential. When the electron and ion temperature is equivalent i.e. the system is in

the thermal equilibrium ($T_e = T_i$), the above formula is rewritten as

$$\lambda_D^{-2} = \frac{n_e e^2}{\epsilon_0 k_B T_e}(1 + Z_i), \tag{2.7}$$

and if the ion distribution does not change much by the potential, corresponding to $T_e \ll T_i$, (2.8) can be reduced to

$$\lambda_D^{-2} = \frac{n_e e^2}{\epsilon_0 k_B T_e}. \tag{2.8}$$

Now, we see what happens in the temperature-density region explained initially. For example, assume a state whose density and temperature are 10^{22} cm^{-3} and 1 eV, respectively and ionization degree is unity. The Fermi energy at this density is calculated to be 1.7 eV. The electron temperature is almost comparable to the Fermi energy and the electrons are Fermi-degenerated. In this case, for example, the electrons around the Fermi surface cannot decrease their energy, so that the electrons cannot get closer to the ion core. Then, the ion potential drops electrons off and ionizes naturally even at $T_e = 0$. This phenomenon is known as the pressure ionization due to the Fermi pressure. The inter-atomic distance is almost the Wigner-Seitz radius ($R_0 = (3/4\pi n_i)^{1/3}$) and calculated to be 3 Å at this density. The ionic potential is 4.8 eV at this inter-atomic distance. The potential is not shielded sufficiently as general plasma, resulting in the effective ionic correlation in plasma.

Therefore, the state within a temperature-density region shown in Fig. 2.1 is classified as the so-called warm-dense-matter state which differs from a classical plasma and from solid. Modeling the WDM state is one of the challenging works in fundamental plasma physics. The electron degeneracy and ionic correlation are key phenomena to model the WDM state. The effects of ion-ion coupling and electron degeneracy are determined by the following parameters.

$$\Gamma_{ii} = \frac{\phi_{ii}}{k_B T_i}, \tag{2.9}$$

$$\Theta_e = \frac{k_B T_e}{\varepsilon_F} \tag{2.10}$$

When these parameters are closer to unity, each effect works considerably. For references, in a solid state, $1 \ll \Gamma_{ii}$, $\Theta_e \ll 1$, and in a plasma $\Gamma_{ii} \ll 1$, $1 \ll \Theta_e$.

2.3 *ab-initio* molecular dynamics simulation

The Modeling of the transport properties in the WDM state, especially the electrical conductivity, requires the consideration of the electron degeneracy and the ionic correlation as explained above.

At a low-density WDM state, the electron degeneracy becomes dominant because the ions are not strongly correlated. In that case, the conductivity can be explained well with degenerate and partially-ionized plasma models. In these models, several

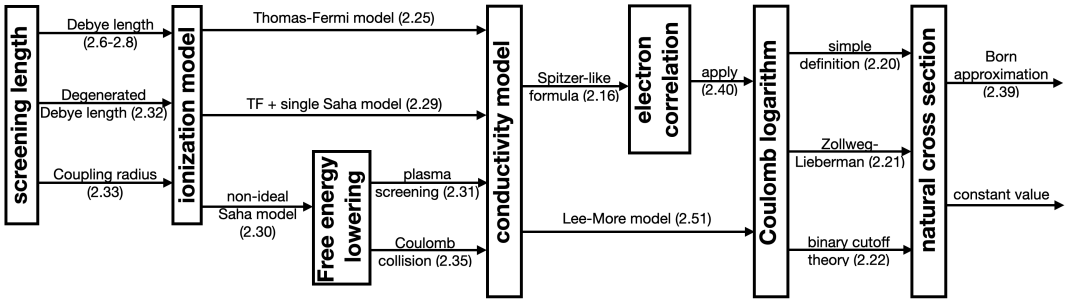

FIGURE 2.2: Flowchart of the classical conductivity models. The various approaches have been developed and modified to model the electrical conductivity of WDM state by assuming the degenerate and partially-ionized plasmas.

modifications extending the Spitzer conductivity,

$$\sigma(n_e, T, Z) = (4\pi\epsilon_0)^2 \frac{2^{5/2}}{\pi^{3/2}} \frac{(k_B T)^{3/2}}{\sqrt{m_e} e^2 Z \ln\Lambda(n_e, T, Z)}, \tag{2.11}$$

to the WDM have been developed[49, 50, 51], where Z and $\ln\Lambda$ are the ionization degree and the Coulomb logarithm. The ionization degree and the Coulomb logarithm are modified to describe the potential screening and electron degeneracy. The various approaches in the degenerate and partially-ionized plasma models are summarized in a flowchart shown as Fig. 2.2. This covers almost all of the modification methods. The detail description of the classical approaches are written in Appendix B.

However, at a high-density WDM state such as a solid density, the ionic correlation also becomes dominant; the plasma-based models explained above becomes inappropriate at this state. In order to reproduce the WDM state correctly considering both the electron degeneracy and ionic correlation, we used the *ab-initio* (quantum) molecular dynamics simulation. Here we introduce the *ab-initio* molecular dynamics simulation.

2.3.1 Ground-state calculation — Density Functional Theory

The Thomas-Fermi model [1] provides physical properties such as total energy only with the electron density. This theory is the basis of the density functional theory. The kinetic energy in the Thomas-Fermi model gives the incorrect value because this model is based on the free-electron gas (Fermi gas) model, thus the electrons correlation is neglected. The density functional theory (DFT) was developed to correct this point. The basic equation of the DFT is the Kohn-Sham equation,

$$\Big(-\frac{\hbar^2}{2m_e}\vec{\nabla}^2 + U_{ion}[n_e] + U_H[n_e] + U_{XC}[n_e] \Big)\psi = E_{tot}[n_e]\psi \tag{2.12}$$

[1] See Appendix B

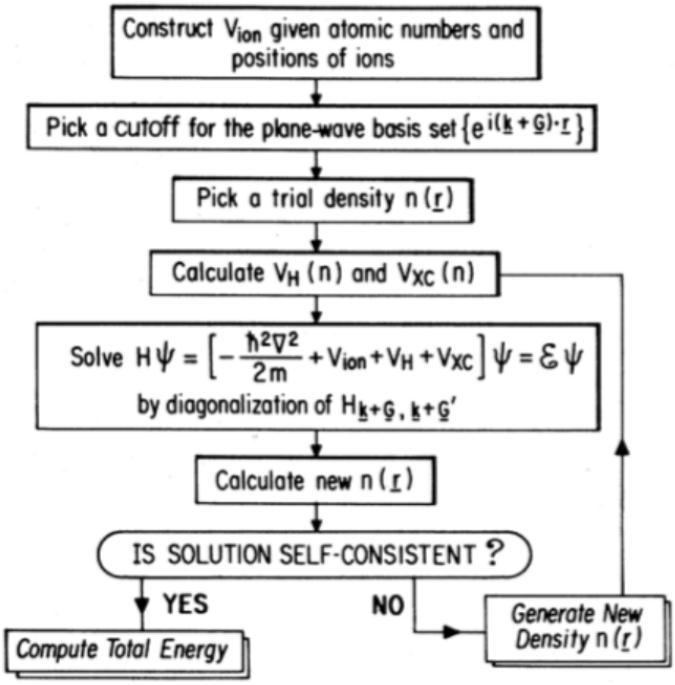

FIGURE 2.3: An iterative process of self-consistent field (SCF) calculation[52]. Kohn-Sham equations for each electron are solved iteratively until the electron density or total energy are converged sufficiently.

where, $U_{ion}[n_e]$, $U_H[n_e]$, $U_{XC}[n_e]$ are the ionic potential, the Hartree potential, and the exchange-correlation potential as functionals of the electron density, n_e, respectively. This Kohn-Sham (KS) equation also assumes the independent-electron approximation, instead, all of the exchange-correlation effect of electrons are included in $U_{XC}[n_e]$. The numerical solution of this KS equation provides various physical properties which agree with a lot of experimental data. The computation of electron states based on KS-DFT is known as "first-principle" band calculation, and often used in the condensed matter physics.

Figure 2.3 shows a self-consistent calculation process in KS-DFT. The KS equations for each electron are solved with the given electron density and ionic configuration. The results of electron states are used as the input parameter in the next step. This process is iterated until the calculation provides converged total energy or electron density. This iterative process is also known as "self-consistent field" (SCF) calculation.

2.3.2 Simulation parameters for ground-state calculation

The SCF calculation requires some physical parameters to provide converged results. In general, the *ab-initio* calculation uses the plane-wave basis $\{e^{i(\vec{k}+\vec{G})\cdot\vec{r}}\}$ to solve the KS equation under the periodic boundary condition, where $\vec{k}$ is the electron wave number and $\vec{G}$ is the reciprocal lattice vector. One should expand with infinite plane

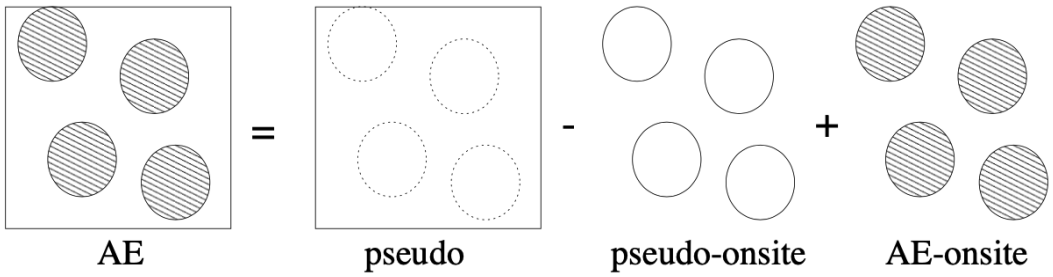

FIGURE 2.4: A simple illustration of the Projector-Augmented Wave (PAW) method. In the PAW method, the pseudo-potential can be obtained by replacing the core (on-site) potential with the results of all-electron (AE) calculation. Thus, the PAW method assumes "cold" core-electrons for a single atom.

waves to obtain the real electron states, but this is not realistic. Thus, the simulation requires a cut-off of the plane wave expansion to reduce a calculation cost. This is the cut-off energy, $\hbar^2/2m_e|\vec{k}+\vec{G}|^2$, which represents how many plane waves are used in the calculation. One should make sure how many plane waves give a converged result. The cut-off energy determines how much the wave function is fine. The wave function (electron orbitals) oscillates violently near the nucleus due to the deep potential. To reproduce this behavior of the core electrons orbital, the higher cut-off energy is required. However, a lot of physical properties and phenomena depend on the valence electrons not core electrons, and higher cut-off just wastes a calculation cost to reproduce core electrons behavior. The pseudo-potential method is that the calculation treats only the valence electrons i.e. reproduce the wave functions exactly only around the edge of the atom. In this method, the ionic potential that gives the accurate wave function far from the nucleus compared to the wave function with all-electron calculation is used in the SCF calculation. This can significantly reduce the required cut-off energy. There are some useful methods to create a pseudo-potential e.g. norm-conserved potential and ultra-soft potential[53]. Especially, the projector augmented wave (PAW) method which is often used recently provides the most efficient SCF calculation.[54, 55] For a quick explanation, this method replaces the wave function and potential of core electrons with the results of the all-electron calculation for a single atom as shown in Fig. 2.4. The PAW method assumes "cold core electrons for a single atom". For this reason, the PAW method does not provide exact results for high-temperature or high-density materials. At high electron temperature, core electrons would be excited thermally, and at high density, the electron wave functions possibly overlap for each PAW sphere. Basically, the PAW radius must be greater than the Wigner-Seitz radius. The PAW radius is usually about 2 a.u. ($\sim$ 1 Å), so the acceptable density is about 2×10^{23} cm^{-3}.

In addition to the cut-off energy, the SCF calculation requires a k-point sampling and the number of bands. For a microscopic system, physical properties are usually discussed in reciprocal space (k-space) not real space. The number of k-points corresponds to a spatial mesh of classical simulations. The number of bands represents

how many eigenstates are calculated in a k-point. A large number of bands provides higher energy levels. Note that the higher energy levels cannot be calculated when the number of bands is too large for the cutoff energy.

In the DFT calculation, the periodic boundary condition is imposed on a supercell. The k-points are sampled within the reciprocal space of the supercell i.e. within the Brillouin zone. The Brillouin zone becomes tiny. When the size of a supercell is large (corresponding to low density or a large number of atoms), a small number of k-points gives accurate results because the Brillouin zone becomes tiny for a large system. Instead, a large number of bands is required for a large supercell because an energy gap between levels narrows.

Figure 2.5 shows an illustration of the relation between the number of bands, the number of k-points, density of state, and electron occupation. Figure 2.5 (a) is the band structure (dispersion relation) of solid copper; the vertical and horizontal axes represent energy and k-points. The number of eigen energies at one k-point corresponds to the number of bands, and the number of red points in one band (solid black) corresponds to the number of k-points. The density of state shown in Fig. 2.5 (b) corresponds to the number of eigenstates integrated within an energy bin shown in the orange rectangle. This density of state is just the number of states which would be occupied by electrons, kind of like the number of seats. The Fermi-Dirac distribution function represents a percentage of electrons occupying the density of states, not just an energy distribution. The actual energy distribution of electrons is a product of the density of state and Fermi-Dirac occupation, and the total number of electrons is expressed as

$$n_e = \int_{-\infty}^{+\infty} \mathrm{d}\varepsilon \; D(\varepsilon) f(\varepsilon, T) \tag{2.13}$$

2.3.3 *ab-initio* molecular dynamics

Physical properties of cold and crystal structured materials are often discussed in a condensed matter physics, and it can be solved only with ground-state calculation. However, in addition to electron ground states, the thermal motion of ions should also be treated for high-temperature material such as WDM. This point can be achieved with the *ab-initio* (quantum) molecular dynamics (QMD) simulation. A classical molecular dynamics can calculate trajectories of a vast number of atoms by using an approximated inter-atomic potential such as the Lenard-Jones potential, Morse potential as well. Whereas, the QMD treats the inter-atomic potential as the sum of the ionic pseudo-potential, electron (Hartree) potential. A simple illustration of the QMD process is shown in Fig. 2.6. First, the electron states and the inter-atomic potential are calculated with a given ionic configuration (DFT process), and then the ionic trajectory is calculated with the obtained potential. The SCF cycle is calculated between MD steps, thus the QMD takes large calculation cost. Instead,

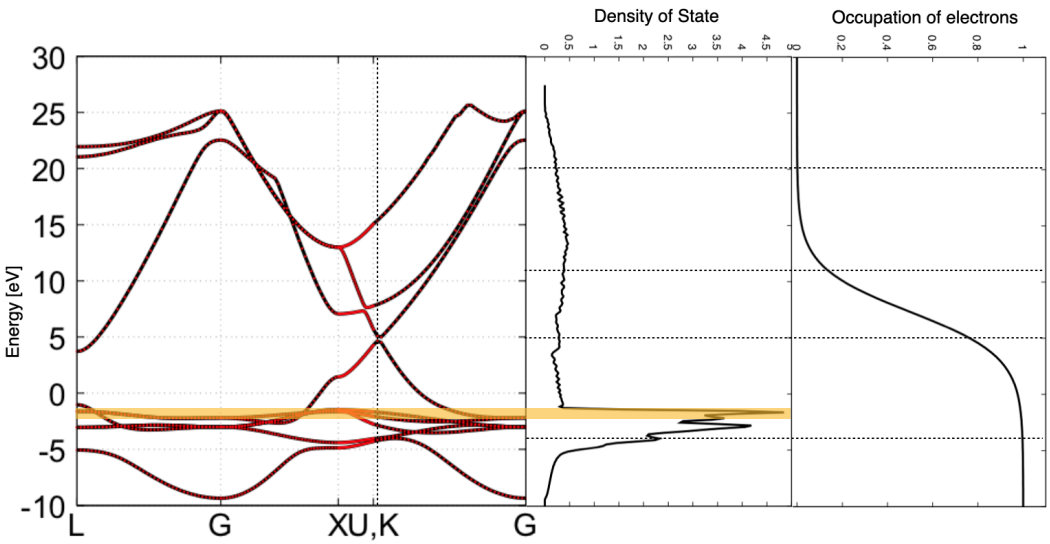

FIGURE 2.5: Calculation parameters for SCF calculation using band structure of copper crystal as an example. The number of bands and k-points correspond to a number of eigenstates in a single k-point and a number of sampling in a single-band, respectively. The density of state represents a number density of total eigenstates in an energy bin $\varepsilon \sim \varepsilon + \delta\varepsilon$.

it provides an exact results. Several techniques are applied in the QMD to reduce a calculation cost. In general, the QMD reduces the calculation cost assuming the Born-Oppenheimer approximation that the atoms are immobile during the ground-state calculation, otherwise, electron states and ionic trajectories must be solved at the same time. And in each DFT step, to reduce the calculation cost, a single "special point" representing several k-points is often used instead of multiple k-points sampling. The original idea of a special point is to reduce the k-points sampling based on the symmetry of the crystal structure, but this method is also applicable to a kind of liquid-like structure such as WDM empirically[56, 57].

2.4 Kubo-Greenwood formula

As described above, the WDM state where the electron degeneracy and ionic correlation are dominant can be modeled with the QMD simulation. The Kubo-Greenwood formula is widely used in the WDM fields to calculate the electrical conductivity (or other transport properties) by coupling with the QMD results. This approach was originally proposed by Desjarlais[59]. Using the Kubo-Greenwood formula, we can obtain the electrical conductivity as

$$\sigma(\omega) = \frac{2\pi e^2\hbar^2}{3m_e^2\Omega\omega} \sum_{n,m,\vec{k}} \left(f(\varepsilon_m^{\vec{k}}) - f(\varepsilon_n^{\vec{k}})\right) \left|\langle\psi_n^{\vec{k}}|\vec{\nabla}|\psi_m^{\vec{k}}\rangle\right|^2 \delta(\varepsilon_n^{\vec{k}} - \varepsilon_m^{\vec{k}} - \hbar\omega). \tag{2.14}$$

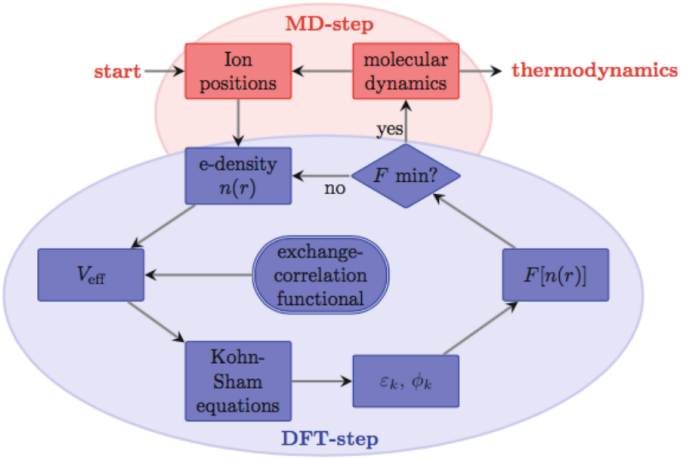

FIGURE 2.6: An iterative process of *ab-initio* (quantum) molecular dynamics (QMD) simulation[58]. The ionic configuration and electron states are solved alternately, and calculated iteratively until the total energy or total pressure of the system are converged.

The Kubo-Greenwood conductivity represents an optical response to external excitation, namely, optical conductivity. This formula depends on the photon energy (light frequency) not only the electron temperature. The static conductivity can be obtained by taking a limiting process of $\omega \to 0$ same as Drude conductivity.

The Kubo-Greenwood formula treats the conduction electrons as the electrons which can transition to upper levels by external stimulation, not as all of the free electrons of n_e. Figure 2.7 shows a simple illustration of the Kubo-Greenwood formula. Assume that the electrons in energy level, ε_n, transition to a higher level, ε_m, by the optical excitation, $\hbar\omega$. In this situation, the occupation rate of the electrons that would transition is $f(\varepsilon_m) - f(\varepsilon_n)$. The transition rate of these electrons can be expressed as the Fermi's golden rule, and is proportional to $\left|\langle n|\hat{H}|m\rangle\right|^2 \delta(\Delta\varepsilon - \hbar\omega)$, where $\hat{H}$ is the perturbed Hamiltonian of the external stimulation. Thus, the electrons responding to the external stimulus can be simply expressed as

$$\Big(f(\varepsilon_m) - f(\varepsilon_n)\Big)\left|\langle n|\hat{H}|m\rangle\right|^2 \delta(\varepsilon_n - \varepsilon_m - \hbar\omega). \tag{2.15}$$

In actual, the energy levels of electrons degenerate and this expression should be integrated by the density of state, thus, (2.14) includes the summation with respect to k-vectors and states.

2.5 Electrical conductivity of warm dense gold

We estimated the electrical conductivity of warm dense gold over wide-temperature-range 300 K - 100 eV combining the QMD simulation with the modified Spitzer model. Figure 2.8 shows the dependence of gold conductivity on the temperature used for this calculation.

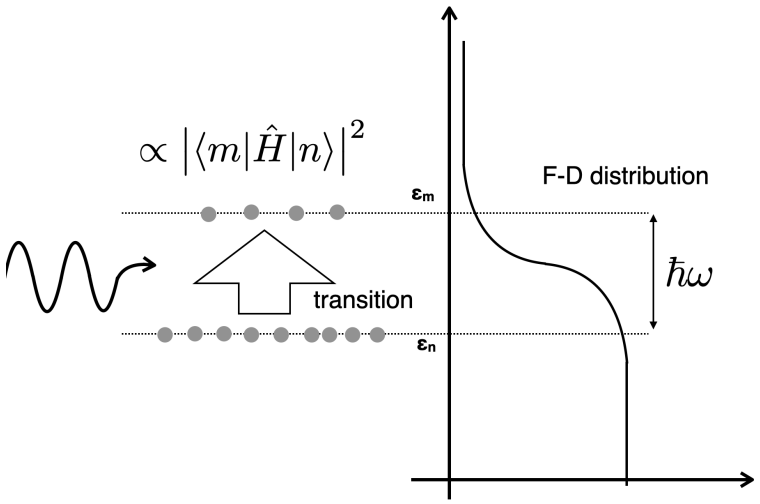

FIGURE 2.7: A simple illustration of the KG formula. Only the excited electrons contributes the electrical conduction in KG formula.

Here, For $T < 0.27$ eV, the experimental data were used. For $0.27 < T < 7$ eV, the conductivity was calculated by the QMD simulation. For 7 eV $< T$, the conductivity was calculated with the modified Spitzer formula. The details are described below.

The conductivity below $T_\mathrm{b} = 0.27$ eV of the boiling point was calculated with the empirical fitting formula αT^{-n} based on experimental results[60], where α and n are fitting parameters. For solid phase i.e. temperature less than melting temperature $T_\mathrm{m} = 0.12$ eV, $\alpha = 6.90 \times 10^5$ and $n = 1.14$. For liquid phase i.e. temperature less than boiling temperature $T_\mathrm{b} = 0.27$ eV, $\alpha = 7.91 \times 10^5$ and $n = 0.65$.

In a temperature range of $0.27 < T < 7$ eV, we estimated the electrical conductivity of warm dense gold with the *ab-initio* molecular dynamics simulation.

The quantum molecular dynamics (QMD) simulation was performed to determine the atomic configuration with *Viena Ab-initio Simulation Package* (*VASP*)[61, 62]. The atomic trajectory was calculated through the QMD based on the Nosé-Hoover thermostat[63]. Then, the electron orbitals and the eigen energies for the transport properties were calculated through the plane-wave Kohn-Sham density functional theory (DFT) with *ABINIT* code[64]. The QMD calculations were performed during 2-4 ps with 2 fs of a time step. 32 atoms were treated in a supercell. For each atom, 11 electrons ($5d^{10}6s^1$) under the projected augmented wave (PAW) pseudo-potential were taken into account in this calculation. The cutoff energy was set to be 600 eV, and the special point was used instead of a bunch of k-points for MD steps. The generalized gradient approximation (GGA) using Perdew-Burke-Ernzerhof (PBE) functional was used as the exchange-correlation potential.[65] Following, the ground-state of electrons were calculated with five snapshots of atomic configurations. In the ground-state calculation, the k-points were sampled by 2^3 in the Brillouin zone with the Monkhorst-Pack scheme.

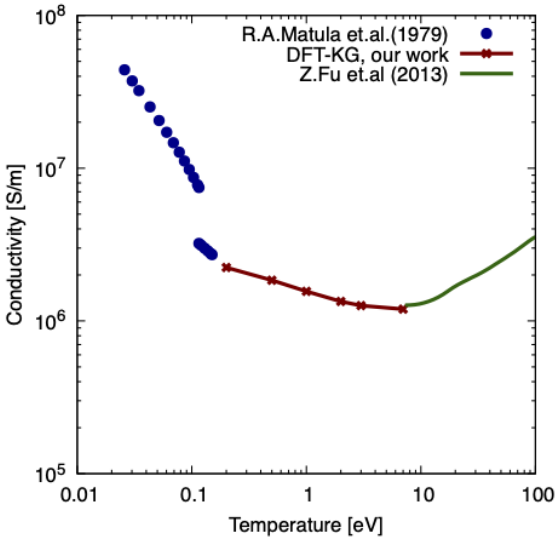

FIGURE 2.8: Temperature dependence of the electrical conductivity of solid-dense gold. For $T < 0.27$ eV, the experimental data were used. For $0.27 < T < 7$ eV, the conductivity was calculated by QMD simulation. For 7 eV $< T$, the electrical conductivity was calculated with the modified Spitzer formula.

The electrical conductivity was evaluated as the DC limit ($\omega \to 0$) of the Kubo-Greenwood formula (2.15). The delta function in (2.15) was replaced with the following Gaussian

$$\frac{1}{\sqrt{\pi}\Delta}\mathrm{e}^{-(x/\Delta)^2} \tag{2.16}$$

in this calculation. The parameter, Δ, was set to be 0.05 Ha (1.36 eV). The values are averaged for five snapshots in an MD trajectory to reduce statistical error.

In order to obtain the DC conductivity, we extrapolated the DC limit with the Drude conductivity curve which represents the free-electron contribution. In theory, a difference between each eigen energy have to be small to take the DC limit exactly following the selection rule. In many cases; however, the convergence of the DC limit requires a vast number of atoms such as 1000 to increase the range of the periodic boundary at the same density[66]. The calculation with a large number of atoms is not realistic for high-Z material such as gold. The minimum difference of energy was approximately 0.1 eV in this calculation; therefore the conductivity below 0.1 eV does not have a physical meaning. Note that the obtained electron number density and relaxation time as fitting parameters should not be actual values because the Drude model assumes all of the electrons are free and it cannot account for the temperature dependence. Also note that the Kubo-Greenwood expression only accounts for the vertical transitions. At the low temperature in which the atoms are ordered periodically, the electron-phonon scattering (especially the Umklapp scattering), which changes the momentum, takes place dominantly. In that case, the Kubo-Greenwood expression for the DC limit is no longer valid[67, 68].

We confirmed that the DC limit of optical properties is converged numerically with 54, 108 atoms and with 3^3, 4^3 k-point samplings. The numerical fluctuation of the optical conductivity at a low frequency can be reduced with a large number of k-points. The statistical error with 2^3 k-points sampling was reduced by taking an average of five snapshots. Also, the optical conductivity with 32 atoms gives almost the same results compared to the one with 54 atoms. Our results also agree with the conductivity with 108 atoms calculated by another author[69].

The PAW method, which assumes the cold core electrons for a single atom, does not provide exact results for high-temperature. For this reason, we evaluated the electrical conductivity with *ab-initio* MD until 7 eV.

Above a temperature of 7 eV, the electrical conductivity was calculated on the basis of the modified Spitzer-Härm formula used in Ref.[51], described as

$$\sigma(T) = \gamma_e(Z_{\rm ion}) \frac{T^{1.5}}{38 Z_{\rm ion} \ln \Lambda} \tag{2.17}$$

where γ, $\ln\Lambda$, and $Z_{\rm ion}$ are the electron correlation factor, the Coulomb logarithm, and the ion charge state, respectively. The electron correlation factor[70] describes the effect of electron degeneracy. The Coulomb logarithm in this model was calculated with classical-binary cut-off theory[49].

The ionization state was calculated with the non-ideal Saha equation which contains the continuum lowering due to the electron screening effect.

$$\frac{n_z n_e}{n_{z-1}} = 2\frac{U_z}{U_{z-1}} \Big(\frac{2\pi m_e k_B T}{h^2} \Big)^{3/2} \exp\Big(- \frac{I_z^{\rm eff}}{k_B T} \Big), \tag{2.18}$$

where h, n_z, and U_z are the Planck constant, number density, and internal portion function for z-fold ions. $I_z^{\rm eff}$ is the effective ionization energy i.e. $I_z - \Delta I_z$ from $(z-1)$ to z. The correction of the ionization energy, ΔI_z, (potential lowering) was calculated from,

$$\Delta I_z = \frac{(z+1)e^2}{\sqrt{\lambda_D^2 + (\frac{2}{3}a_z)^2}} \tag{2.19}$$

where λ_D and a_z are Debye length and ion sphere radius for z-fold ion respectively. Note that the excited state data such as U_z, I_z in (2.18) come from the database compiled by the National Institute of Standards and Technology[71].

2.6 Summary

In summary, we estimate the electrical conductivity of warm dense gold over wide-temperature-range 300 K - 100 eV combining the QMD simulation with the modified Spitzer model. For the techniques of strong magnetic-field generation such as a laser-driven coil, a large current of $\sim$ 100 kA causes Joule heating in the coil and changes the coil resistance during the pulse. Also in the magnetized HEDP experiments with

intense magnetic pulse, temperature of sample materials increase drastically due to the induction heating accompanied with the magnetic diffusion, and the electrical and thermal conduction also changes over time. The temperature dependence of the transport properties such as the electrical conductivity in wide-temperature range is essential to evaluate the intense-field dynamics described above numerically. Our result will promise significant contributions to a modeling of the high-power laser-driven coil and estimation of the intense magnetic diffusion.

Chapter 3

Dynamics of laser-generated magnetic fields using long laser pulses

We report on the experimental investigation of magnetic field generation with a half-loop gold sheet coil driven by long-duration (10 ns) and high-power (0.5 TW) laser pulses. The amplitude of the magnetic field was characterized experimentally using proton deflectometry. The field rises rapidly in the first 1 ns of laser irradiation, and then increases slowly and continuously up to 10 ns during further laser irradiation. The transient dynamics of current shape were investigated with a two-dimensional (2D) numerical simulation that included Ohmic heating of the coil and the resultant change of electrical resistivity determined by the coil material temperature. The numerical simulations show rapid heating at the coil edges by current initially localized at the edges. This current density then diffuses to the central part of the sheet coil in a way that depends both on normal current diffusion as well as temporal changes of the coil resistance induced by the Ohmic heating. The measured temporal evolution of the magnetic field is compared with a model that determines a solution to the coil current and voltage that is consistent with a plasma diode model of the drive region and a 2D simulation of current diffusion and dynamic resistance due to Ohmic heating in the laser coil.

3.1 Introduction

Experimental study of magnetized plasma dynamics is an active area of research in the field of high-energy-density (HED) science. The generation of strong magnetic fields has been developed at several facilities and is being applied to HED experiments. There are several techniques for generating a strong magnetic field. For example, non-destructive single-turn and Helmholtz coils driven by pulsed-power devices are typically used to generate magnetic fields below ∼100 T for a long-time (> 1 μs) and large-scale (> 1 mm^3)[72, 73, 74, 75]. These coils have been successfully used in astrophysical HED experiments such as the formation of plasma jets[16, 18] and shocks[17, 19]. Above 100 T these coils explode and emit debris which can put

diagnostics and laser optics at risk. A laser-driven coil does not require a separate pulsed power system, and it has been shown in a number of experiments to produce B $\geq$ 100 T at high-power laser facilities such as GEKKO-XII[7, 9], OMEGA-EP[76, 47], LULI2000[8], and Shenguang-II[77]. The temporal and spatial scales of the magnetic field generated by the laser-driven coil tend to be shorter time ($\sim$ 1 ns) and smaller volume ($\sim$ 1 mm^3) compared to the conventional devices. However, the laser-driven coil itself is small and has less debris generation. Thus, it can be easily implemented in laser-based HED experiments and is good for the maintenance of a laser laboratory composed of expensive optical elements. Because of these advantages, the laser-driven coils have been used and are planned to be used in numerous HED experiments such as those on magnetic reconnection[78], magneto-hydrodynamic instability[20], charged-particle beam control[24, 32, 79], laser-plasma interactions[34, 35, 80], and inertial confinement fusion[21, 25, 27, 28]. Despite the significant number of HED studies performed with laser-driven coils, the mechanism of magnetic field generation is still not fully understood.

A widely used laser-driven coil consists of two plates and one loop-coil connecting the plates. The plates supply voltage and a magnetic field is generated by the current flowing in the coil. The laser-driven coil was first demonstrated by Korobkin and Motylev using a 1054-nm laser[81]. Seely *et al.*[82] and Daido *et al.*[83] improved the understanding of this coil. Courtois *et al.* proposed a model based on a lumped-element RLC circuit[10]. In their model, the laser generates a space-charge current between two plates, which charges the two-plate capacitor to a voltage that corresponds to a few times the temperature of the non-thermal hot electrons generated by the laser drive. The voltage on this capacitor then drives a current through the coil. The current begins to decay even during the laser-irradiation once the accelerated ion front crosses the gap between the two plates and reaches the cathode plate. The time scale for this decay is d/C_s, where d and C_s are the separation distance between the plates and the sound speed of the plasma, respectively. This model was modified by Goyon *et al.* to include the self-consistent charging of the plate capacitor, the space-charge current generated by the hot electrons, and the temporal evolution of the capacitance due to Debye shielding by the plasma between the two plates[47]. Fiksel *et al.*[11] proposed a model based on a lumped-element RLC circuit that considers thermal electron and ion currents in addition to the non-thermal hot-electron current. This model gives a lower magnetic field amplitude compared to that observed in experiments.

Tikhonchuck *et al.* developed a laser-driven diode model[12] that predicts the magnetic field remains during the laser-pulse, unlike the prediction by the above models. In this model, the plasma initially exhibits one-dimensional planar expansion from the laser-irradiated plate as described by Mora[84]. The planar expansion transitions to a spherical expansion after the expansion front travels a distance equal to the laser spot radius. This spherical expansion is stationery in time and generates a plateau potential distribution in the gap. This potential remains during the laser irradiation, allowing the current to keep flowing. The current, i.e. electron flow, is limited by the

potential distribution (space-charge limit) and by the self-generated magnetic field (self-magnetization limit) that is similar to the Alfven limitation mechanism. These two mechanisms of the electron current limit are considered in this model. This model also considered the change of coil resistance and the modification of the coil geometry due to ohmic heating. The model explains fairly well several experiments obtained at different laser facilities using a laser intensity of $> 1 \times 10^{15}$ W/cm^2 and a pulse duration of ~ 1 ns. Recently the laser-driven diode model was experimentally tested at a low laser intensity ($\leq 10^{14}$ W/cm^2) and a pulse duration ranging from 0.5 to 20 ns[85]. In this experiment, the generated voltage and current were measured directly. The results showed that the voltage and current are retained during the laser irradiation. These results can be explained by assuming that the laser drive creates a voltage source that is approximately equal to the laser-heated electron temperature, $k_B T_e$. The relatively small (< 100 A) current means that the Ohmic heating effect on coil resistance was negligible. The behavior of the laser-generated magnetic field in the transition from a single-temperature thermal electron energy distribution to a non-thermal hot-electron component has not been explored because there is little to no hot-electron component for this low-intensity laser drive.

The motivation of our study is to generate a magnetic field of > 100 T lasting up to 10 ns by using a 10-ns and 0.5-TW high-power laser. In this paper, we show the experimental results for laser-generated magnetic fields with long-duration (10 ns) and high-power (0.5 TW) laser pulses, and we present an advanced theoretical model of the laser-driven magnetic field that includes current dynamics by the laser-drive, current diffusion, and ohmic heating all self-consistently. We discovered that a laser-driven coil can maintain a magnetic field of a few hundred tesla during the laser pulse duration (at least 10 ns and possibly much longer) even after low-density plasma fills the vacuum gap between the plates. During laser irradiation, the magnetic field strength increases gradually after ramping up quickly. Further, our numerical simulations are done for the duration of the experiment and show spatial and temporal changes of the magnetic field topology. We attribute these changes to transient current diffusion and Ohmic heating induced by the dynamic evolution of current density in the coil. We show that the experimental results can be reproduced with a theoretical model that accounts for the laser drive, the current diffusion, and the temporal evolution of the resistance of the half-loop sheet coil. This is a useful result for HED experiments; an extension of the magnetic field pulse longer than 1 ns is required for the investigation of the magnetized HED plasma dynamics, which generally takes place in a nanosecond time scale, e.g., magnetized inertial confinement fusion and collisionless shock experiments. For these HED experiments, the laser-driven coil has to drive a current even with sample materials inside a loop during the pulse. This should be investigated in future experiments.

3.2 Measurement methods of Magnetic field

In the field of the HEDP physics, following three methods are primary used to measure a strong magnetic field: pick-up coil (as know as B-dot probe), Faraday rotation, and proton radiography (deflectometry). The pick-up coil detects a temporal variation of a magnetic field $\partial B/\partial t$ as a voltage signal via the Faraday's electromagnetic induction mechanism. Thus, the detected voltage signal should to be integrated in time to convert the magnetic field. Note that the pick-up coil should be placed at far from a source of the magnetic field if one tries to measure the magnetic field of over 100 T. Otherwise, the pick-up coil or the receiver would be broken. In the Faraday rotation method, as it's named, a magnetic field is measured via the Faraday rotation effect. A magnetized crystal has different refraction index for left and right hand circular polarization. One can estimate the magnetic field from the rotation of the polarization. Also in this method, the crystal should be placed at far from the source like the pick-up coil. If the crystal is placed near the source, the crystal would be heated and changes its physical properties; the crystal becomes opaque to visible light. In the two methods above, one should extrapolate the magnetic field near the source position.

The proton radiography is the method to measure the magnetic field directly. The charged particles are deflected by the electromagnetic field via the Lorenz force; one can estimate the spatio-temporal evolution of the electromagnetic field from this deflection. This method is often used in the field of HEDP physics. However, this method has the restriction that the plausible magnetic field distribution should be assumed in advance to estimate the magnetic field distribution. Therefor, we cannot estimate the magnetic field only with the experimental data. In addition, the plasma also affects the proton deflection in HEDP experiments. (This make the analysis quite difficult...) This disadvantage is considered as problem in the measurement of the strong magnetic field. Thus the algorithm to reconstruct the magnetic field distribution from only the experimental data are investigated in several approaches: the algorithms using neural network[86], Lloyd's algorithm[87], and others have been investigated. However, there is no successful progress that one has reconstructed the electromagnetic field distribution from only experimental data and even also the simulated patterns. The difficulty in the reconstruction of the field is that both the field distribution and the proton trajectories cannot be determined as the same time. One should know the particle trajectories in the field to reconstruct the field distribution, but the particle trajectories depend on the field distribution. Thus this inverse problem is generally impossible to solve.

The field distribution can be reconstructed when the electric and magnetic fields are weak enough to be able to assume the particle trajectories are liner. Kugland et al proposed this reconstruction method theoretically[88]. Here, we introduce this mtehod in short.

The protons propagates distance l and pass thorough the region that the magnetic field are imposed, then the protons are deflceted and recorded at the position away

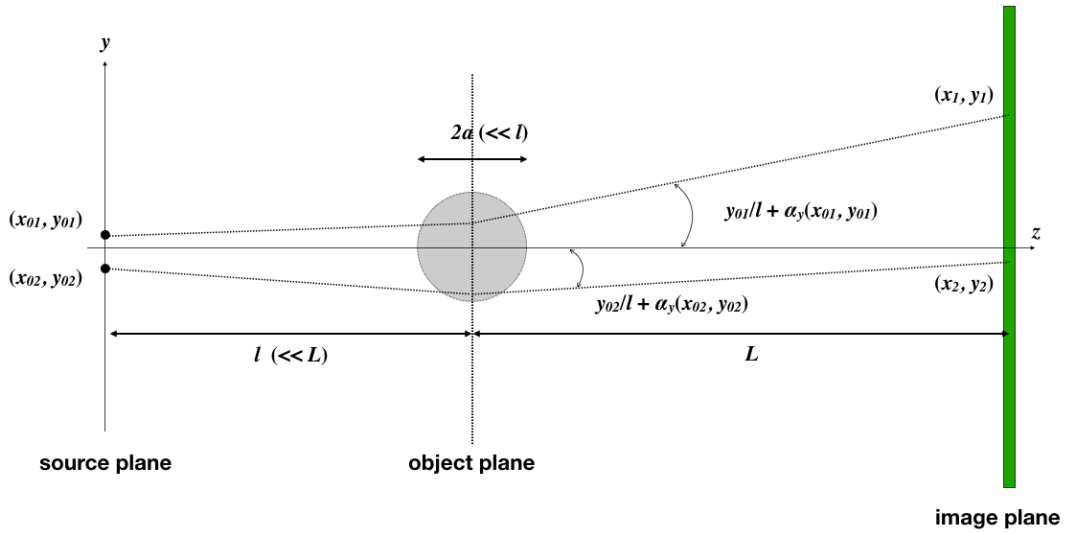

FIGURE 3.1: A simple illustration of proton beam reconstruction. The proton which propagate l from the position (x_{01}, y_{01}) on source plane passes through the cylinder region with radius a, where the electromagnetic fields are imposed, and is deflected by the Lorentz force; the proton propagate L, and is observed at the position (x_1, y_1) on the image plane. For a liner-approximation, $2a \ll l \ll L$ should be satisfied. This approximation allows analytical expression.

L from there, as shown in Fig. 3.1. The region that the imposed magnetic field influences the particle trajectory is limited within the cylindrical region with diameter of $2a$. This spatial scale is relatively small ($2a \ll l$), and the detector is placed at far ($l \ll L$). The proton that positioned at $\vec{x}_0$ initially is detected at

$$\vec{x} = \left(\frac{\vec{x}_0}{l} + \vec{\alpha}(\vec{x}_0)\right) L \tag{3.1}$$

on the observation plane. The first term represents the trajectory that ignores the magnetic field, and the second term represents a small deflection due to the magnetic field. A deflection vector is obtained from the equation of motion in the assumption that the proton propagates linearly in z direction (small deflection). The deflection vector takes different expression for electric and magnetic fields. The deflection vector for the magnetic field is expressed as

$$\vec{\alpha}_B(\vec{x}_0) = -\frac{e}{\sqrt{2m_p c^2 \varepsilon_p}} \vec{\nabla} \Phi_B(\vec{x}_0) \ , \tag{3.2}$$

$$\Phi_B(\vec{x}_0) = \int_{-\infty}^{+\infty} \mathrm{d}z_0 \ A_z(\vec{x}_0) \tag{3.3}$$

While, the deflection vector for the electric field is expressed as

$$\vec{\alpha}_E(\vec{x}_0) = -\frac{e}{2\varepsilon_p} \vec{\nabla} \Phi_E(\vec{x}_0) \ , \tag{3.4}$$

$$\Phi_E(\vec{x}_0) = \int_{-\infty}^{+\infty} \mathrm{d}z_0 \ \phi(\vec{x}_0) \tag{3.5}$$

where, ε_p is the kinetic energy of the proton, and the deflection potential $\Phi_B(\vec{x}_0)$ and $\Phi_E(\vec{x}_0)$ are defined for both electric and magnetic fields for the mathematical conveniences. A key point in the equations above is that $\vec{\alpha}_B(\vec{x}_0)$ is proportional to $\varepsilon_p^{-0.5}$, whereas $\vec{\alpha}_E(\vec{x}_0)$ is proportional to ε_p^{-1}. The deflections due to the electric and magnetic fields can be distinguished using this energy dependence of the deflection vectors. Assuming that proton beam pattern $I_0(\vec{x}_0)$ is observed when the magnetic field vanishes, the pattern

$$I(\vec{x}_0) = \frac{I_0(\vec{x}_0)}{|J(\vec{x}_0, \vec{x})| + \epsilon} \sim I_0(\vec{x}_0)\Big(1 - l\vec{\nabla}_0 \cdot \vec{\alpha}(\vec{x}_0)\Big) \tag{3.6}$$

is observed when the weak magnetic field are applied, where, J is Jacobi's determinant to $\vec{x}_0, \vec{x}$, and ϵ is a resolution parameter. This is the theoretical analysis for the "weak" fields. The active research is to developed the algorithm solving the inverse problem when the electromagnetic field is strong enough is investigated.

In some special cases, one can solve the inverse problem and obtain the field distribution with (3.6). Using (3.2) and (3.6), one can obtain the following Poisson equation to $\Phi_B(\vec{x}_0)$

$$\vec{\nabla}^2\Phi(\vec{x}_0) = -4\pi\left(\frac{\varepsilon_p}{2e\pi}\Big(\frac{I(\vec{x}_0)}{I_0(\vec{x}_0) - 1}\Big)\right) = -4\pi P(\vec{x}_0) \tag{3.7}$$

The values of ε_p, $I(\vec{x}_0)$, and $I_0(\vec{x}_0)$ are observable experimentally, thus the deflection potential $\Phi_B(\vec{x}_0)$ can be obtained from experiments. The potential (3.3) includes the information of the magnetic field (or the vector potential), basically one can reconstruct the field distribution from this deflection potential (or deflection vector). Especially, when the applied magnetic field is axial-symmetric and parallel in x-direction, namely $B_x(r)$, the deflection vector is a line integral crossing the cylindrical magnetic field, and is just the Abel transform. Thus, the inverse Abel transform is applicable to the deflection vector, and the magnetic field is calculated as

$$B_x(\vec{x}_0) = \frac{1}{\pi}\int_{+\infty}^{r} \mathrm{d}r' \ \frac{1}{\sqrt{y^2 - r'^2}}\frac{\partial \alpha_{yB}}{\partial y}(\vec{x}_0). \tag{3.8}$$

3.3 Experimental setup

The experiments were conducted at the OMEGA-EP facility. Figure 3.2 shows the experimental setup. One of two OMEGA-EP beams, whose pulse shape is square (100-ps rise time) and duration is 10 ns, passes through holes on the front plate and irradiates the back plate of a half-loop gold sheet coil with a 25-degree off-normal incidence angle. The laser energy, intensity, and wavelength are 5 kJ, 2.2×10^{15} W/cm^2, and 351 nm, respectively. The surface of the back plate is coated with a 10-μm-thick plastic layer to increase the plasma scale length, resulting in higher-energy electron generation via laser-plasma interactions. The radius, thickness, and width of the half-loop sheet coil are 250 μm, 12.5 μm, and 1.15 mm, respectively.

In our experiment, the coil has three through holes on the front plate and three exit slots on the back plate, which allow the field amplitude to be observed at three points along the central axis of the coil. A previous experiment using a similar target[47] quantified the magnetic field strength at the center of the coil; however, the target had only one hole-slot pair for proton deflectometry. The front side faces the proton source. Protons passing through the holes are deflected downward by the magnetic field in the coil. The deflected protons exit through the slots toward the detector. The wide sheet coil used in this experiment is unlike the thin-wire coils used in other laser-driven magnetic field studies. The wide coil enhances the current diffusion effects and non-uniform Ohmic heating in the magnetic field generation process, which are not observed clearly in a thin-wire coil. The initial circuit parameters for the coil, which are calculated based on the geometry and tabulated normal gold properties, are $R = 5.4$ mΩ, $L = 0.4$ nH, and $C = 0.06$ pF.

Proton deflectometry is the primary method used to measure the amplitude of the magnetic field in this experiment. A 1-ps 1054-nm pulse with an intensity of 8×10^{18} W/cm^2 is focused onto 10-μm-thick gold foil to generate protons that range from a few to 30 MeV of energy via the target normal sheath acceleration mechanism[29, 89]. The proton source is placed 6.5 mm from the laser-driven coil. Deflected protons are detected using radiochromic film (RCF) stacks located 80 mm from the coil. A stack of eight RCFs is used to detect protons up to 29.4 MeV[90]. A copper screen with a 65-μm wire spacing in a square grid is used to track the deflection of protons across the entire image.

3.4 Analysis methods

Figure 3.3 shows the experimental (right half) and simulated (left half) proton images in the case of (a) no laser-irradiation and images obtained at (b) 0.62, (c) 1.15, and (d) 7.08 ns after the beginning of the laser irradiation, respectively. The time origin is defined at the half-maximum of the rising edge of the coil-driving laser pulse. The protons detected by the RCF layer shown in Figs. 3.3 (c)-(d) have an energy of 29.4 MeV.

3.4.1 Width measurement

The magnetic field strength is estimated from the proton deflection pattern and then compared to that in simulated proton images, as shown in Fig. 3.3. The field amplitude at the edges of the coil (defined as the edge magnetic field) can be inferred from the width of the proton shadow indicated by the red arrow. Measurement of the proton shadow width can provide the time evolution of the edge magnetic field for a long time duration. The protons are primarily subjected to the fringing magnetic field around the coil. Here, we estimated the edge magnetic field by matching the width (edge to edge length) of the simulated proton image to the experimental image. In this analysis, the current density in the target was unknown from the experiment,

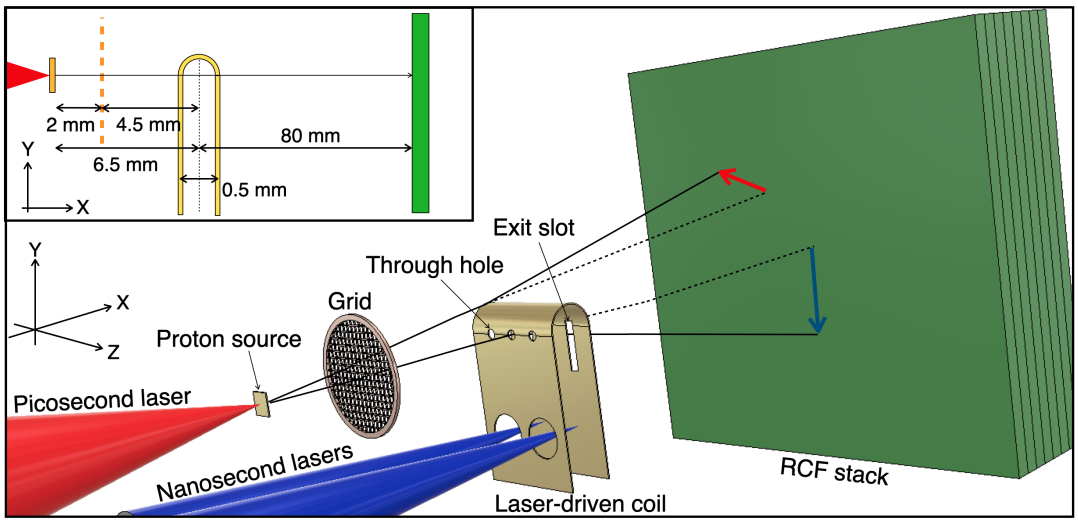

FIGURE 3.2: Experimental setup of proton deflectometry for the measurement of the magnetic field which is illustrated in 3-D and 2-D. The magnetic field is generated with a half-loop gold sheet coil driven by one of two nanosecond OMEGA-EP beams that have an energy of 5 kJ, a power of 0.5 TW, and a duration of 10 ns. The generated magnetic field is toward in z-direction. The protons are generated from the thin gold foil irradiated with a picosecond OMEGA-EP beam, which have an intensity of 8×10^{18} W/cm^2. The proton beam imprint by the grid is deflected by the generated magnetic field and detected by radiochromic films.

thus we used two limiting cases to estimate the edge magnetic field: (1) a uniform current density and (2) an edge-peaked current density. The uncertainty in the edge magnetic field is caused by three sources: proton energy resolution corresponding to an RCF layer, the uncertainty in current density distribution (uniform or edge peaked), and scattering of protons by plasma and the coil itself. The errors in the width are estimated by fitting both edges using a Gaussian error function shown as Fig. 3.4 The fitting Gaussian error function is given as

$$y = \frac{a}{2}\left(1 \pm \mathrm{erf}\left((x - x_0) \times \frac{2\sqrt{\ln 2}}{\delta}\right)\right) + y_0, \tag{3.9}$$

where a, x_0, y_0 are fitting parameters and y corresponds to a signal intensity on an RCF. The full width at half-maximum (FWHM) of the Gaussian function, δ, corresponds to the error of the width. This error automatically includes the energy resolution corresponding to an RCF layer, the scattering effect by surrounding plasma, and the coil. The widths of the proton shadows were converted to magnetic field strengths with a formula relating the shadow width and the magnetic field strength. The errors due to the uncertainty of the current density distribution appear in the magnetic field through this conversion. The temporal evolution of the estimated magnetic field is discussed in Sec. 3.7.

The right-half images of Figs. 3.3(a)-(d) show computed proton images obtained

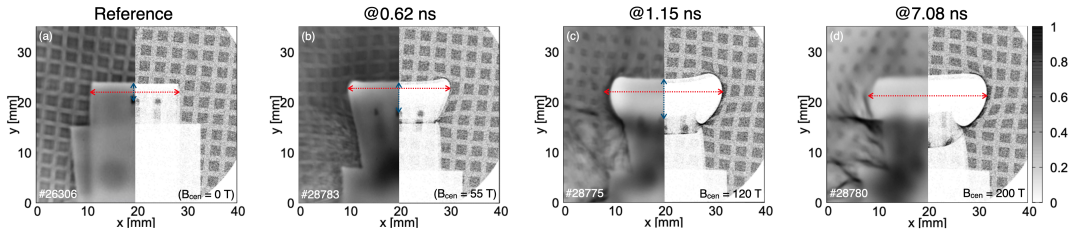

FIGURE 3.3: Comparisons between the experimental (right half) and computed (left half) proton images in case of (a) no laser-irradiation (cold target) and images obtained at (b) 0.62, (c) 1.15, and (d) 7.08 ns after the beginning of the laser irradiation. The computed image reproduces well the experimental proton image. The small difference in the shape of the coil shadow between left and right comes from the difference in coil shape, namely half-loop in the experiment and cylinder in the calculation.

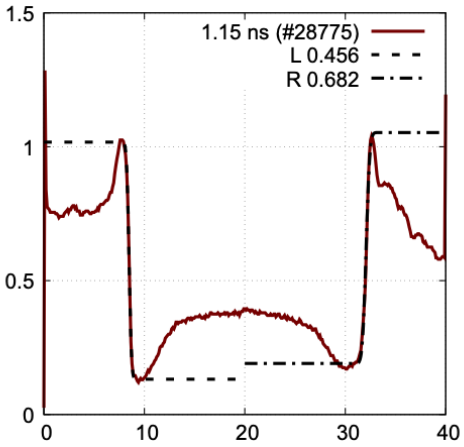

FIGURE 3.4: An example of error estimation at 1.15 ns. The error of the width is estimated by fitting the left and right edges with the Gaussian error function. The total width error at this time is estimated to be 0.536 cm.

using 2D (r and z) cylindrically symmetric magnetic fields instead of the actual half-loop geometry. The proton image shown in Fig. 3.3(a) corresponds to a cold reference of the proton deflection which is calculated without any magnetic fields. The right proton images shown in Figs. 3.3(b) and (c) were calculated with the edge-peaked current distribution, where the strengths of a magnetic field at the center of the coil are set to be 55 T for (b) and 120 T for (c). The right proton image in Fig. 3.3(d) was calculated with the uniform current distribution, where the magnetic field is set to be 200 T at the center of the coil. These computed images (right-half) reproduces well the experimental proton image (left-half). The small difference in the shape of the coil shadow between left and right comes from the difference in a coil shape, namely a half-loop in the experiment and a cylinder in the calculation. The proton beam pattern became worse at later timings because the TNSA source was preheated by radiation from the coil itself. This simplified 2D geometry is a good surrogate for the experimental coil geometry (half-cylinder attached to two plates) and is estimated to

have current diffusion time scales similar to those in the experiment. The cylinder geometry is also more easily modeled and can provide useful insight for understanding the experimental results. The geometrical error for the edge field between the 2D cylinder and the three-dimensional half-loop coil is less than 10%[47] . The simulation uses a Monte-Carlo method with 10^6 particles to generate the proton images from a magnetic field table; this was calculated from a prescribed current density in the coil.

3.4.2 Deflection measurement

The magnetic field at the three holes can be estimated from the vertical shifts of the proton dots indicated by the blue arrow. The vertical shift of the dots corresponds to the integral of the Lorentz force along the full trajectory of the protons. The proton dots corresponding to the three through holes can be clearly seen at relatively early times, as shown in Figs. 3.3(b) and (c). However, the proton dots become quite weak at later times, as shown in Fig. 3.3(d). This occurs because the protons are deflected so much downward and possibly with a slight asymmetric deflection to the side that they cannot escape from the inside of the coil region through the exit slots. We can place a lower bound on the magnetic field amplitude at these axial locations; however, the uncertainty in these data makes this unsuitable for precisely quantifying the magnetic field and, as we discuss later, the local current density due to the current diffusion in the central coil region. Future experiments should extend the holes further downward and widen them to accommodate larger proton shifts in both directions and obtain a better signal from the through holes.

We also evaluated if the plasma filled between the plates affects on the proton image, and conclude that the proton slowing-down due to collisions with electrons and small-angle-scattering due to collisions with ions are negligibly small in this measurement. Here we evaluated the plasma effects as follows.

The electron stopping power in plasma can be approximately calculated with

$$-\frac{\mathrm{d}E}{\mathrm{d}x} = \frac{1}{4\pi\epsilon_0}\left(\frac{Ze\omega_p}{v_p}\right)^2\Big(H(v_p/v_{th})\ln\left(v_p/v_{th}\right) + G(v_p/v_{th})\ln\left(\lambda_D/r_0\right)\Big) \tag{3.10}$$

where, v_p and v_{th} are energy of the projectile and thermal electrons, respectively[91]. Functions $H(x)$ and $G(x)$ are expressed as follows.

$$G(x) = \mathrm{erf}\left(\frac{x}{\sqrt{2}}\right) - \sqrt{\frac{2}{\pi}}x\mathrm{e}^{-x^2/2} \tag{3.11}$$

$$H(x) = \frac{x^4}{x^4+12} - \frac{x^3\mathrm{e}^{-x^2/2}}{3\sqrt{2\pi}\ln\left(x\right)} \tag{3.12}$$

Using the results from Goyon et al., we approximate the parameters for the plasma filling the region between the plates as $n_e = 10^{20}$ cm^{-3}, $T_e = 10$ keV, and $Z = 50$. A 29.4-MeV proton is estimated to be slowed down (due to electron collisions) at a rate

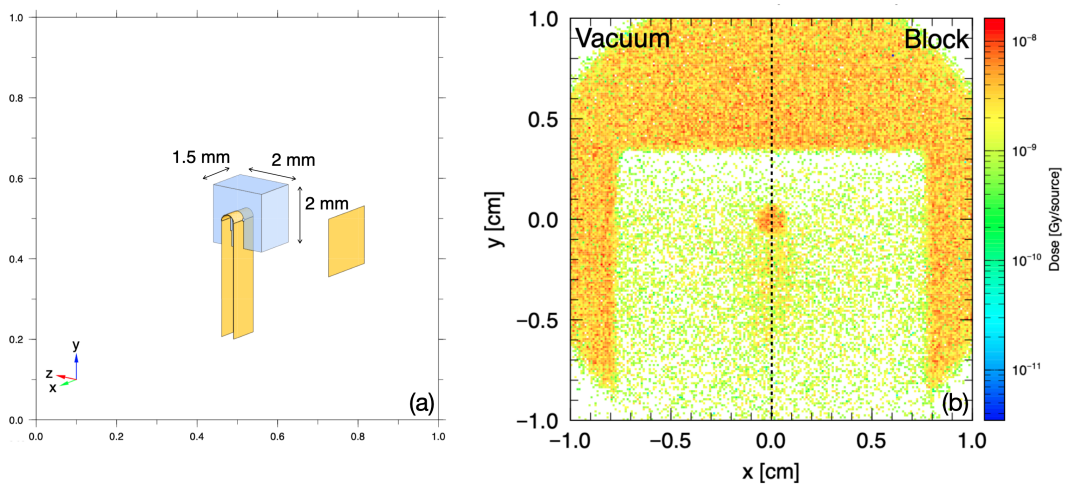

FIGURE 3.5: (a) Calculation geometry of *PHITS* code. Left-half region is vacuum and right-half region is filled with a plastic block mimicking filled plasma whose volume is 1.5 × 2 × 2 mm. (b) Comparison of proton images with/without a low-dense plastic block. We can identify the central proton dot on both images.

of -15 MeV/cm with (3.10). The spatial scale length of this plasma is about 2 mm so that the energy loss is calculated to be 3 MeV. This value would be an overestimate since there is CH in the plasma with lower Z. If we set Z to be 10, the energy loss can be calculated to be 0.14 MeV.

On the other hand, we estimated the effect of small angle scattering on plasma ions by putting a low-density solid gold instead of a gold plasma plume because the plasma is quasi-neutral. Figure 3.5 shows the 29.4-MeV proton image on the 8th RCF layer calculated by a Monte-Carlo based particle transport simulation code *PHITS* including Coulomb scattering[92]. The left half image shows the dose distribution of protons through a vacuum. Whereas, the right half image shows the dose distribution of the protons transmitted through a 2-mm gold block whose ion density is 10^{20} cm^{-3}. We can identify the central proton dot in the coil shadow in the two images despite the right side having a high-density plasma.

3.4.3 Dose variation measurement

In addition we attempted to evaluate the edge magnetic field from the dose variation of the accumulated protons at the edges seen in Fig. 3.3: this method was performed by Lancia et al[93]. However, it is tough to distinguish the cause of the intensity variations in the proton images between either a magnetic field or the non-uniform initial pattern of laser-produced protons. As a result, any analysis of the experiment relying on the proton intensity would be subject to large uncertainty and therefore not useful in our experiments. Below we provide more details on how we reached this conclusion.

Energetic ions passing though the RCFs deposits a fraction of energy to RCF, then RCF is colored depending on the deposited energy. The shade of this color

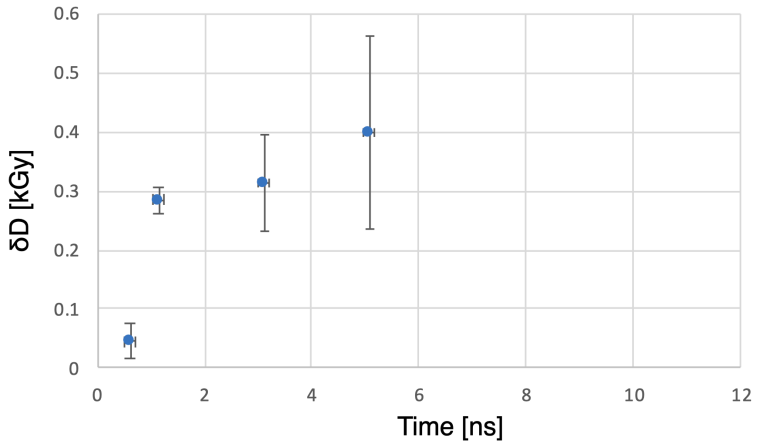

FIGURE 3.6: Temporal evolution of the dose variation between one at the edge and background dose. The result is fairly similar to the temporal evolution of the magnetic field strength evaluated from the shadow width.

on the scanned RCF corresponds to the absorption rate of the scanning laser and also absorbed dose on the RCF. This color shade is usually quantified as the "optical density" in fields such as imaging and spectroscopy. Thus, scanning films corresponds to measuring the optical density. The optical density is generally defined as the following formula,

$$OD(I_{film}) = -a \log\left(\frac{I_{film} - I_0}{I_{100} - I_0}\right), \tag{3.13}$$

where, I_{100}, I_0, and I_{film} are maximum and minimum signal intensities, and the signal intensity on a scanned film. The RCF is originally colored and the background signal is observed when it is scanned. To evaluate the absorbed dose due to the energetic protons on the RCF, we used the effective optical density as $OD_{eff} = OD(I_{sig}) - OD(I_{bg})$. The relations between the absorbed dose and optical density depends on types of films and color channels. We used the HD-V2 of RCF in this experiments and estimated the absorbed dose from a red channel. For a red channel of HD-V2 film, the relation between dose D [kGy] and OD_{eff}^{red} is given as following expression[94].

$$OD_{eff}^{red}(D) = \frac{9.58 \times 10^6 D + 7.52 \times 10^4 D^2}{3.34 \times 10^6 + 4.33 \times 10^6 D + 2.95 \times 10^4 D^2} \tag{3.14}$$

Figure 3.6 shows the estimated dose variation between the signal at the edge and background. The result shown in Fig.3.6 is fairly similar to the temporal evolution of the magnetic field strength evaluated from the shadow width. Note that the dose variation was quite weak at 0.6 ns. This is because the magnetic field strength is not enough strong to create a non-linear proton accumulation known as a "caustics structure" [88]. At later timings after 5 ns, we could not observe a clear difference at the edge because the TNSA source was irradiated by x-ray radiation from the

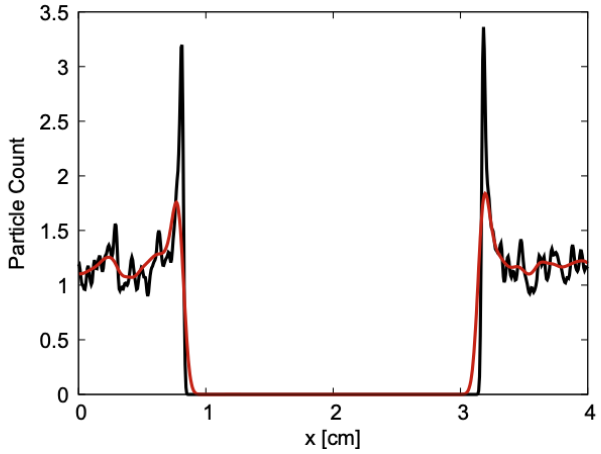

FIGURE 3.7: Line-outs of simulated proton images. A black line represents the line-out without any plasma, whereas a red line represents the line-out convoluted with the Gaussian function which has FWHM of 0.1 cm.

U-shaped coil itself and the proton beam pattern degraded. This degraded proton beam pattern is the major reason why there is no clear difference at the coil edge after 5 ns. The smoothing on the proton accumulation cannot be explained only with the plasma density effect. Figure 3.7 shows two line-profiles of synthesized proton images. The black curve corresponds to the profile without any plasma. Whereas the red curve corresponds to the profile convoluted with a Gaussian function, whose FWHM is 0.1 cm, this is how we model the scattering effect of plasma. This FWHM was obtained from the experimental proton images after 5 ns. The plasma mass density is evaluated to be 5×10^{-2} g/cm^3 (corresponding to an ion number density of 5×10^{21} cm^{-3}) if this spreading is caused only by the scattering due to plasma. A clear difference at both edges is observable even if such a dense plasma filled the space and caused proton scattering.

3.5 Current diffusion and ohmic heating

The current diffusion along only the axial direction was considered in the evaluation of the diffusion time in previously reported OMEGA-EP laser-driven coil experiments. The diffusion time was calculated with a one-dimensional diffusion model for a conductor[95]. The axial diffusion time is much longer (> 1000 ns) than the laser pulse (1 ns), and thus static current and magnetic distributions were assumed in the previous analysis. However, simple estimates show that the radial current diffusion time is approximately $4\mu_0\sigma d^2/\pi^2 = 3.2$ ns which is much shorter than the axial diffusion time and pulse duration (10 ns) in our experiment, where σ is the electrical conductivity of gold (the common reference value is 4.09×10^7 S/m at 300 K). Thus, the current diffusion dynamics must be considered here.

In addition to the current diffusion, the large current (~ 100 kA) resistively heats the gold coil, leading to a temporal change in coil resistivity, as described in a previous

study[96]. Note that current diffusion is typically a linear process, but it becomes non-linear in cases with significant Ohmic heating[96, 97]. The current redistribution resulting from these effects allows a significant current density to flow in the entire coil region even at an early time in the laser pulse. The current diffusion also affects the total resistance $R(t)$, changing the time evolution of the current density and the generated magnetic field. In this section, we show the results of a simulation that models current diffusion and the material temperature change from Ohmic heating.

We investigated the effects of current diffusion and Ohmic heating using a 2D cylindrical transient simulation[98]. This 2D simulation does not model the gap in the target cylinder where the plates attach and does not include the plates, as was done by Goyon[47]. The most important effects we included here are the radial and axial current diffusion and the Ohmic heating effects on current density. These effects can be well modeled in two dimensions.

The modeled cylinder is pure gold, with an inner radius of a =250 μm, a thickness of 12.5 μm, and a length of 1.15 mm. This matches the dimensions of the half-loop coil used in the experiments. Null current and room temperature are set as the initial conditions. In the laser-driven coil, the voltage is supplied by the laser drive between the two flat plates. We implemented this voltage by imposing a slowly time-varying electric field defined as $E_{back,\phi}(r,z,t) = E_0(t)r/a$ throughout the solution volume. The total electric field is expressed as $\vec{E} = \vec{E}_{back} + \vec{E}_{ind}$ where $\vec{E}_{ind}$ is the electric field that results from the time changing magnetic field. Note that the background electric field vanishes at $r = 0$ and is used to drive the current in the conductor. Similarly, the total magnetic field is expressed as $\vec{B} = \vec{B}_{back} + \vec{B}_{ind}$. The time-varying part $E_0(t)$ is determined by iterating to a consistent solution between the numerical simulation and the circuit model that we describe in the next section. This background electric field generates a spatially-uniform background magnetic field such that $B_{back,z}(t) = -\int_0^t \mathrm{d}t'(\vec{\nabla} \times \vec{E}_{back}(t'))_z = -\int_0^t \mathrm{d}t' 2E_0(t')/a$. Here, we focus on the magnetic field generated by the current in the cylinder, and thus we subtract the background magnetic field from the calculated magnetic field. In this transient simulation, the electric and magnetic fields are numerically calculated from the following Maxwell's equations:

$$\frac{\partial \vec{E}_{ind}}{\partial t} = \frac{1}{\mu\varepsilon}\vec{\nabla} \times \vec{B}_{ind} - \frac{\sigma}{\varepsilon}(\vec{E}_{back} + \vec{E}_{ind}) - \frac{\partial \vec{E}_{back}}{\partial t} \tag{3.15}$$

$$\frac{\partial \vec{B}_{ind}}{\partial t} = -\vec{\nabla} \times (\vec{E}_{ind} + \vec{E}_{back}) - \frac{\partial \vec{B}_{back}}{\partial t} = -\vec{\nabla} \times \vec{E}_{ind} \tag{3.16}$$

The induced electric and magnetic fields were solved over a whole solution volume with the applied background electric field. Ohmic heating is included as $c_V \rho \partial T/\partial t = \sigma(T)|E_\phi + E_{back,\phi}|^2$ where c_V and ρ are the isochoric specific heat and density of gold, respectively. Thermal diffusion is too small to matter at the experimental timescale. The detailed description was discussed in Ref.[98]. Simulations were run in a 1000 μm

$\times$ 2000 μm calculation boundary with a 2-μm mesh size.

The simulation used the conductivity table of gold produced with *ab-initio* calculations.[99] Here, we assumed an isochoric ohmic heating process during the pulse. The conductivity of gold decreases with temperature in the solid phase. As the temperature approaches 1 eV, gold transitions to the warm-dense-matter phase and the conductivity tends to be a constant value of about 10^6 S/m. At higher temperature (i.e., in the plasma phase), the conductivity begins to increase. We will discuss the details in a separate work.

Figures 3.8(a) - (c) show line-outs of the current density integrated in the radial direction and 2D distributions of the coil temperature at times of (a) 0.6 ns, (b) 1.1 ns, and (c) 3 ns. At 0.6 ns, the simulated current density has a strong peak at the edges of the coil. This current rapidly heats the coil edges, which decreases both the conductivity and current in this region. Because the central region of the coil is still at room temperature and has high conductivity, the peak of the current density shifts inward to the cold central coil region, as shown by the line-out for 1.1 ns. In addition to the conductivity change caused by Ohmic heating, the radial current diffusion contributes to the redistribution of the current density, as shown in the line-outs for 1.1 and 3 ns. At 3 ns, the entire coil is heated and the fine structure of the current density is smoothed to a roughly spatially uniform value. At still later time, the current gradually increases as the entire coil heats and the conductivity increases. Figure 3.8(d) plots the magnetic field amplitude at the three times normalized by the value at the coil center. The magnetic field on the axis spreads widely due to the edge-peaked structure of the current density at 0.6 ns. As the current diffuses, the width of the magnetic field narrows due to the shift of the current peak and the increase in current flow in the inner part. Later, the width of the magnetic field becomes narrower because the current density distribution approaches the uniform distribution. However, the edge magnetic field shows a fairly weak sensitivity to the spatial distribution of current. We conclude that it would be difficult to experimentally verify current diffusion from only a measurement of the spatial dependence of the edge magnetic field in this geometry. Rather, accurate measurements of the field in the center region of the coil are needed.

The transient simulation can be used to estimate a time-dependent resistance which is needed to form an accurate circuit model of the laser coil. In the next section, we discuss how we model the temporal evolution of the coil current and include the time-dependence resistance.

3.6 Laser-driven diode model

If the plates supply a voltage $V(t)$, simple lumped-circuit equations for the coil current are given by

$$C(t)\frac{\mathrm{d}V}{\mathrm{d}t}(t) = I_d(t) - I(t), \tag{3.17}$$

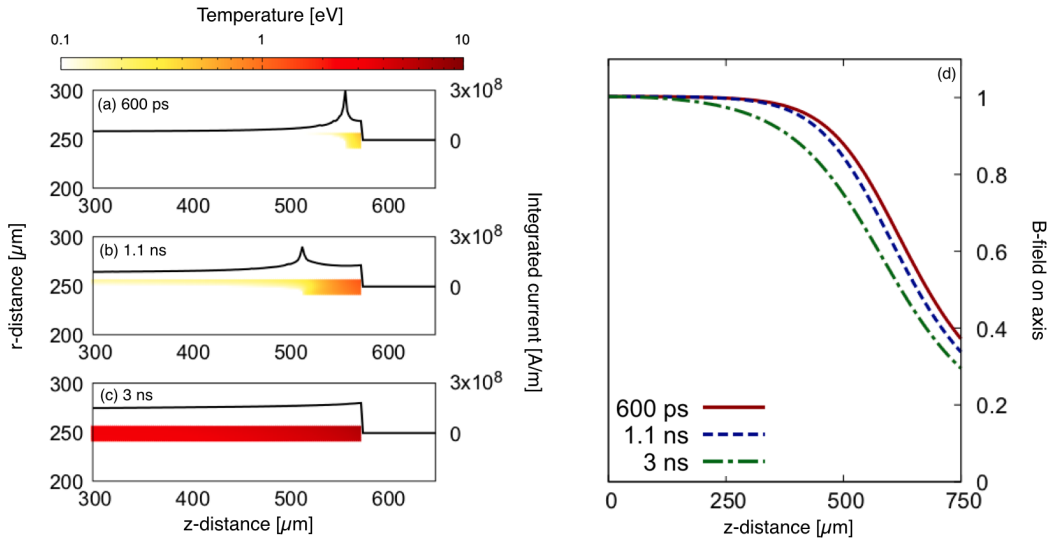

FIGURE 3.8: Line-outs of the integrated current density and 2D distribution of the coil temperature at (a) 0.6 ns, (b) 1.1 ns, and (c) 3 ns after laser irradiation from the transient simulation. We also plot in (d) a line-out of the magnetic field distribution along the central axis. The integrated current density approaches a uniform distribution accompanied by current diffusion and heating from the edges to the whole body. The width of the magnetic field narrows because of the current density diffusion. The magnetic fields are normalized by the value at the center.

$$V(t) = L(t)\frac{\mathrm{d}I}{\mathrm{d}t}(t) + I(t)R(t) \tag{3.18}$$

where $L(t)$ is the coil inductance and $R(t)$ is the time-dependent coil resistance. Equation (4.1) is important only for a creation of the supplied voltage at early time. Note that if the capacitance, $C(t)$, is small, we can reduce the equations to only (4.2) because the coil current becomes equivalent to the drive current, $I_d(t)$, which is described later. The capacitance in this experiment is small, thus we used only (4.2) to calculate the temporal evolution of $I(t)$ and $V(t)$.

The coil inductance initially determines the rate of current increase; therefore, the current in the coil starts out small even though a large voltage is applied to the coil in the start-up phase. As the current in the circuit increases, it is limited by one of two possible mechanisms that are active in the laser drive region: (1) space charge limitation or (2) self-magnetization limitation. The plasma diode model[12] provides a description of the conditions that cause the two current limitations.

Throughout the laser drive, the voltage-current relation in the space-charge-limited region is given by

$$I_d = I_0 \mathrm{e}^{-eV/k_B T_{hot}}. \tag{3.19}$$

The quantity I_0 is the maximum possible current for a given laser intensity and is defined as $I_0 = en_h\pi r_L^2 v_h$, where r_L, n_h, and v_h are the laser focal radius, the hot electron density, and the hot electron velocity, respectively, which give an I_0 value

of 50 MA for our condition. As the current through the coil increases, the voltage decreases according to (3.19). This limit does not include the normal energy distribution of hot electrons, and thus the current limit at low eV/k_BT_{hot} is overestimated. Including a Maxwellian energy distribution for the hot electrons,

$$f(v) \propto v^2 \mathrm{e}^{-mv^2/2k_BT_{hot}}, \tag{3.20}$$

gives the modified space-charge current limit equation. The electrons that has energy lower than the potential gap, V_0, between the capacitor plates should be pulled back to the plate. Then, the drive current including the Maxwellian energy distribution can be written as

$$I_d = n_e e^2 \Big(\int_{v_0}^{\infty} \mathrm{d}v f(v) v \Big) \pi r_L^2, \tag{3.21}$$

where $v_0 = \sqrt{2eV_0/m_e}$ corresponds to the electron velocity that can overcome the potential V_0. Assuming a fraction of the laser intensity, hI_L, is converted to the hot-electron energy flux, we can obtain the following equation,

$$hI_L = \int_0^{\infty} \mathrm{d}v f(v) \Big(\frac{1}{2} n_e m_e v^2 \Big) v. \tag{3.22}$$

Substituting the electron density, n_e, of (3.22) into (3.21) gives

$$I_d = \frac{2}{m_e} ehI_L \pi r_L^2 \frac{\int_{v_0}^{\infty} \mathrm{d}v f(v) v}{\int_0^{\infty} \mathrm{d}v f(v) v^3} = I_c (1 + eV/k_BT_{hot}) \mathrm{e}^{-eV/k_BT_{hot}}, \tag{3.23}$$

This is the modified space-charge current limit proposed by Courtois[10]. Here, I_c is the maximum current defined as $I_c = ehI_L\pi r_L^2/(2T_{hot})$. The values I_L and h are the laser intensity and the conversion rate from the laser to hot electrons, respectively. We find from our analysis that the conversion rate of $h = 0.1$ shows good agreement with our experimental results.

The self-magnetization limit is caused by the prohibition of a large current by the self-generated magnetic field. The maximum current and voltage relation in this case is given by[100] $I_m = V/Z_D$, where

$$Z_D = \sqrt{\frac{\mu_0}{2\epsilon_0}} \frac{\lambda_h}{\pi \alpha r_L}. \tag{3.24}$$

In this formula, λ_h is the Debye length for hot electrons. The parameter α is a geometrical factor (maximum value = 1) that corresponds to the divergence angle of hot electrons that emit from the back plate. We estimate the hot electron temperature in our experiment to be 7 keV[101], giving an effective impedance of $Z_D = 0.034\ \Omega$ using $\lambda_h = 3.2 \times 10^{-6}$ m and $\alpha = 1$. The number density of hot electrons is calculated

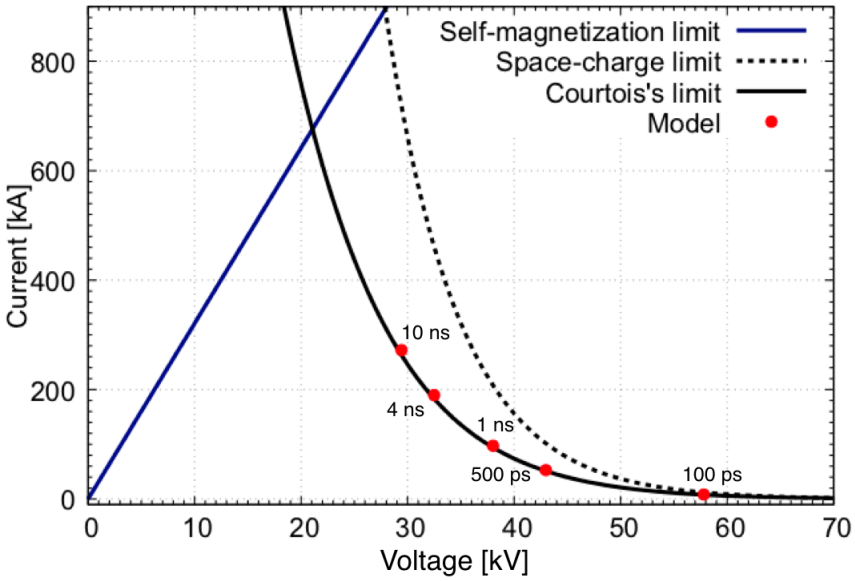

FIGURE 3.9: Relation between voltage and current (V-I) based on the laser-diode model. The current in a laser-driven coil is limited by the space-charge potential (solid and dashed black lines) and the self-magnetization of hot electron flow (blue line). The maximum current is limited to 680 kA at 21 kV. The red points show the temporal change of the V-I relation in this experiment. The calculated current is mainly limited by the space-charge potential labeled as Courtois's limit.

as

$$\frac{n_h}{n_c} = 0.2\left(\frac{I_L \lambda_L^2}{T_{th}}\right) \tag{3.25}$$

assuming 5.7 keV for the thermal electron temperature[102]. Here, n_c and λ_L are the critical density and wavelength of the incident laser, respectively. The maximum current possible in the coil is obtained by setting $\alpha = 1$ and substituting $V = I_m Z_D$ in (4.3). Solving for the maximum current gives $I_{max} = 680$ kA and $V = 21$ kV. This is the maximum current that would flow in the drive region if the two capacitor plates were shorted with no additional impedance.

Figure 3.9 shows the Courtois space-charge-limited V-I relation (4.3) for this experiment in solid black. The dotted black curve is the simple space-charge limited V-I relation (3.19). The blue line shows the magnetization limit. Figure 3.9 also plots the V-I relation solved using the self-consistent iteration method as red points. It can be seen easily now that the calculated circuit current and supplied voltage are located in the Courtois's space-charge limited region. Note that at 10 ns, the experiment is still on the space-charge limited curve. Thus, space-charge is the dominant mechanism that limits the current in the drive region and in the circuit for our experimental conditions.

We wish to find a self-consistent solution for the circuit voltage, current and resistance in (4.2) and (4.3) that is also consistent with the numerical solution to the cylindrical simulation that accounts for current diffusion and coil heating. Here

we developed an iterative method which starts with a time-constant voltage applied to the cylinder simulation. From this constant voltage, we obtain a current density, $j_\phi(r,z,t)$, and a magnetic field, $\vec{B}(r,z,t)$, in the cylinder which we use to determine the total current, $I(t)$, the effective resistance, $R(t)$, and inductance, $L(t)$, that can be used in (4.2). The total current, $I(t)$, can be obtained by integrating $j_\phi(r,z,t)$ over the cross-section. The time-dependent resistance and inductance for the cylinder coil can be calculated from the transient simulation with following relations:

$$R_{cyl}(t) = \int_{coil} \mathrm{d}V\ \sigma(T)|E_\phi(r,z,t)|^2 \Big/ I(t)^2 \tag{3.26}$$

and,

$$L_{cyl}(t) = \frac{1}{\mu_0} \int \mathrm{d}V\ |\vec{B}(r,z,t)|^2 \Big/ I(t)^2. \tag{3.27}$$

Consequently, we can estimate the time-dependent resistance for the actual half-loop coil, $R(t)$, using the relation $R(t) = R_{cyl}(t) \times l_U/l_{cyl}$, where the geometrical factor l_U/l_{cyl} is calculated to be 3.71 mm / 1.57 mm = 2.36. For the inductance, we use a constant value of 0.4 nH in the model calculation because we find that the temporal change of the inductance estimated by (3.27) is negligibly small (< 0.01 nH), and will not affect the temporal evolution of $I(t)$ much. Now that we have $R(t)$ which includes current diffusion and Ohmic heating, we can solve (4.2) for the current time history in the half-loop coil. Continuing to the second iteration we now obtain a new voltage $V(t)$ from (4.1). This voltage, $V(t)$, is converted to the cylinder voltage for use in the simulation using the relation $V_{cyl}(t) = V(t) \times l_{cyl}/l_U$ (corresponding to $E_0(t) = V(t)/l_U$). This $V_{cyl}(t)$ is now used in the cylinder simulation to solve for the new $R(t)$. Iterating this loop until $V(t)$, $I(t)$ and $R(t)$ converge well between iterations, and it yields the self-consistent solution which includes space-charge limited current flow, circuit inductance, current diffusion and Ohmic heating. We note that using the geometrical scaling between the cylinder and the actual half-loop coil, where we multiply $V(t)$ and $R(t)$ by a factor l_{cyl}/l_U, gives the same ohmic heating per unit mass for the cylinder and coil target.

3.7 Temporal evolution of magnetic field

We finally consider the temporal evolution of the magnetic field for times up to 10 ns. Figure 3.10(a) shows the edge magnetic field (filled squares) evaluated from the measurements and the modeled magnetic field time history, which includes current diffusion and Ohmic heating (solid black). Here the edge magnetic field means the field amplitude at the edges of the coil. One can see that the estimated magnetic field increases rapidly during the first 1 ns. This rapid turn-on of the field has also been observed in 1-ns pulses[47)] and low-power laser experiments[85)]. The field after 1 ns shows a slower increase until the end of the laser drive. Based on our analysis, we explain the gradual increase in the magnetic field between 1 and 10 ns as the result

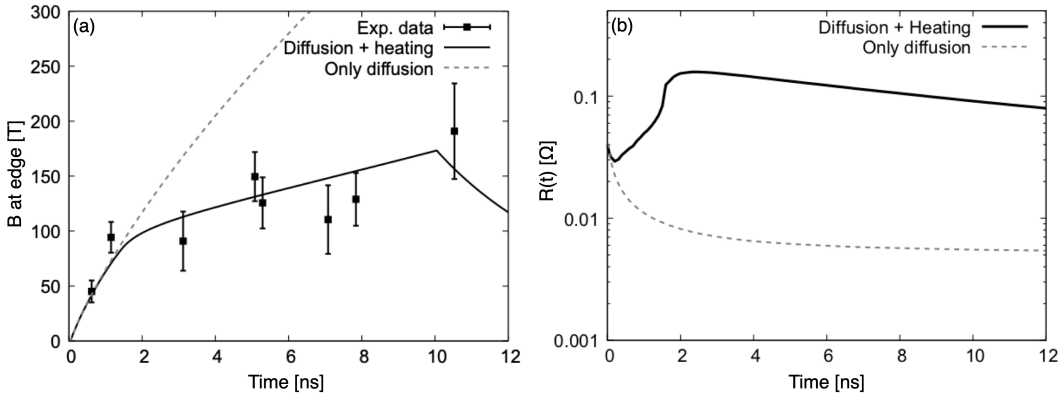

FIGURE 3.10: Time evolution of (a) the edge magnetic field estimated from the experiment (filled squares) and calculated using the circuit model (solid black curve), (b) the effective resistance calculated with the 2D transient simulation. We also show the predicted magnetic field resulting from including only the current diffusion (resistivity is temperature independent). The circuit model with the time-dependent resistance estimated from the transient simulation has good agreement with the experimental data.

of the coil resistance decreasing due to the Ohmic heating. The lower resistance leads to a longer L/R time constant, causing the gradual increase in the magnetic field.

The modeled magnetic field strengths (solid black) shows good agreement with the measured value. The temporal behavior of the field after laser shut-off at 10 ns was not investigated in these experiments. Nevertheless, we estimated the magnetic field time dependence after laser shut-off shown in Fig. 3.10(a) using the expected L/R decay of the current in the target and neglecting any capacitative effects. Based on the work of Goyon *et al.*[47] and Williams *et al.*[85], we acknowledge that the magnetic field time dependence after laser shut-off is more complex than this because there is likely a capacitive effect from the front and rear target plates. The details of this effect require further measurements before it can be included in our model.

Figure 3.10(a) also plots the modeled magnetic field considering only the current diffusion, i.e., where we assume the resistivity is independent of material temperature (dashed gray). In this case, the coil resistance just decreases due to the current diffusion and the resulting magnetic field (and total current) increases. This result does not match the experimental data, and it shows the importance of including the effects of Ohmic heating. Note that the edge magnetic field amplitude was estimated from the diode model using the formula $B_{edge} = 0.6 \times I$ within $\pm 10\%$ error, which was obtained from the results of the transient simulation.

Figure 3.10(b) shows the temporal evolution of the scaled time-dependent resistance, which is calculated from our transient simulation by considering current diffusion and Ohmic heating (solid black), and only the current diffusion (dashed gray). At the beginning (< 100 ps), both resistances decrease due to the current diffusion. If only the current diffusion takes place, the resistance continues decreasing and converges to 5.4 mΩ. However, the conductor is heated enough to significantly

change the resistivity in this experiment. As a result, the increase in resistance due to heating is faster than the resistance decrease due to the diffusion. The coil conductor begins to melt around 1.6 ns, causing its resistance to jump to 0.15 Ω. After melting, the coil resistance slowly decreases due to continued ohmic heating. This slow decrease of the resistance causes the gradual increase of the modeled magnetic field.

3.8 Summary

In summary, we show the measurements of a laser-generated magnetic field with a long-duration (10 ns) and high-power (0.5 TW) laser pulse. The results of proton deflectometry measured at different timings indicate that the magnetic field rises rapidly in ~ 1 ns and then increases slowly for the remainder of the laser pulse. The laser-driven diode model coupled with the simulation of ohmic heating and current diffusion shows good agreement with the experimental data. These are the results of modeling the laser driven coil with an iterative solution method that includes dynamic resistance, current diffusion and space-charge current limitation self-consistently. The dynamics of current diffusion and ohmic heating are simulated with a 2D transient model using cylindrical geometry. The simulation results show that the localized current at the coil edges heats the edges immediately, causing the current density to shift inward as a result of reduced conductivity by ohmic heating.

The central deflection of the proton beam could not be accurately measured at later times in this experiment because the protons could not escape through the exit slots on the coil. We recommend that in future experiments the exit slots should be made large enough to accommodate the significant vertical and horizontal deflections of the protons. Future experiments with larger exit slots will be able to characterize the evolving magnetic field topology and draw conclusions about the dynamics of current diffusion experimentally with the through-hole method.

Chapter 4

Numerical Analysis of Pulsed Magnetic Field Diffusion Dynamics in Gold Cone Target

Strong magnetic fields from a few hundred to a thousand tesla have been produced in a laboratory by using high-intensity laser beams. This strong magnetic field in a laboratory becomes a powerful tool to perform experiments in the fields such as laboratory astrophysics and nuclear fusion research. The diffusion dynamics of a pulsed magnetic field in a target is a key phenomenon for experiments with the laser-produced magnetic field. Here we have developed two-dimensional (2D) electromagnetic dynamics simulation code with consideration of inductive heating to simulate spatiotemporally resolved 2D profiles of the applied magnetic field in a target. Application of an external kilo-tesla-level magnetic field to a gold-cone-attached target is a promising scheme for the enhancement of heating efficiency of the fast-ignition inertial confinement fusion scheme. Our simulation revealed that the magnetic field heats the gold cone due to the inductive heating and penetrates the gold cone during its pulse duration. The developed simulation code is generally useful for designing and analyzing experiments using the strong magnetic field.

4.1 Introduction

Strong magnetic fields from a few hundred to a thousand tesla have been produced in the laboratory using capacitor-coil targets that are irradiated by high-intensity laser beams[83, 10, 7, 8, 9, 76, 47]. These strong magnetic fields have already been applied to plasma physics research, such as magnetic field reconnection[78], control of relativistic electron beams (REBs)[79], magnetohydrodynamic instability[20], and fast-ignition inertial confinement fusion[27].

In particular, for fast-ignition inertial confinement fusion[39], a relativistic-intensity laser pulse is used to instantaneously heat a pre-compressed fusion fuel. A gold cone is attached to a spherical fusion fuel to exclude ablated plasma from the path of the relativistic laser pulse to the fuel[?]. A high-Z dense cone is required to prevent the cone wall from breaking by the ablated plasma and preheating caused by radiation

and hot electrons. Relativistic laser-plasma interactions at the cone tip efficiently produce REB with average kinetic energy of >0.511 MeV[43, 44]. The laser-produced REB typically has a large full divergence angle of 100°[22], and this reduces energy coupling from the heating laser to the fuel core because a small portion of the diverged REB collides with the small fuel core.

Guidance of the diverging REB to the small fuel core is essential to demonstrate efficient fast-ignition. Application of a strong magnetic field to the REB generation and transport regions has been proposed by several authors[45, 24, 46, 25], and this scheme is referred to as magnetized fast ignition (MFI). A proof-of-principle experiment of the MFI scheme was performed at the Institute of Laser Engineering, Osaka University using a laser-driven capacitor-coil target[27]. The laser-produced magnetic field must diffuse into the REB generation zone and REB transport region before producing the REB.

However, the MFI scheme may thus be spoiled by the slow diffusion of the externally applied magnetic field. The thickness and open angle of the gold cone used in the experiment[27] were 7 μm and 45°, respectively. The cone tip has a hole with a diameter of 100 μm. A 500 μm diameter coil made of 50 μm diameter nickel wire was located 225 μm away from the center of the fuel core (see Fig. 4.8). The magnetic pulse duration was approximately 1.5 ns of the full width at half maximum (FWHM)[9]. On the other hand, the magnetic field diffusion time for a cylindrical material is given as $\tau_{\rm dif} = \mu_0 \sigma r l/2$, where μ_0, σ, r, and l are the permeability, electrical conductivity, cylinder radius, and thickness, respectively. The electrical conductivity σ of gold is 4×10^7 S/m under the standard state. The diffusion time $\tau_{\rm dif}$ is calculated to be 8.8 ns for $r = 50$ μm and $l = 7$ μm, which is much longer than the magnetic pulse duration of 1.5 ns.

Under practical conditions, the strength of the magnetic field produced using the laser-driven capacitor-coil scheme alters rapidly in time. This rapid change of the magnetic field strength drives a large inductive current in the cone, and the inductive current heats the cone ohmically. The electrical conductivity of a material is strongly dependent on its temperature and weakly dependent on its density. A temporal change of the electrical conductivity has a significant effect on the magnetic field diffusion dynamics. This self-consistent magnetic field diffusion dynamics is also important for some experiments in a strong magnetic field besides the MFI experiments. For example, the central ignition with a compressed magnetic field[21] and the ion acceleration in a strong magnetic field[32].

The temperature increment ΔT caused by external application of a strong magnetic field pulse can be roughly evaluated as $c_{\rm V}\rho\Delta T = B_0^2/2\mu_0$, where c_V, ρ, μ_0, and B_0 are the isochoric specific heat, density, permeability, and maximum magnetic field strength, respectively. The specific heat of gold under typical conditions is $c_{\rm V} = 129$ J/(K kg) and its solid density is $\rho = 19.3$ g/cm^3. If a magnetic field of 500 T is applied to a gold cone, then its increase in temperature is evaluated to be 3.4 eV. The solid density material at 3.4 eV is in a so-called warm dense matter (WDM) state.

The electrical conductivity of gold at 3.4 eV was calculated to be 4.73×10^5 S/m by using the models described in Ref.[51]. The diffusion time $\tau_{\rm dif} = 104.6$ ps at 3.4 eV is two orders of the magnitude shorter than $\tau_{\rm dif} = 8.8$ ns at the normal temperature. Therefore, the conductivity of the WDM must be considered to calculate properly the magnetic field diffusion dynamics.

The magnetic diffusion dynamics was investigated numerically with consideration of the electrical conductivity dependence on the inductive heating and temperature[98]. However, in the previous analysis of the magnetic diffusion, the current in the laser-driven coil is assumed to be the Gaussian pulse whose FWHM is 1 ns independently to the incident drive laser. Further, the electrical conductivity in WDM state was modeled by the modified Spitzer model which is not adequate in a temperature range 0.1-10 eV at high density. In this section, we improved the previous analysis of the magnetic diffusion: we evaluated the temporal evolution of the coil current by using the self-consistent circuit model described in Sec. 3, and calculated the electrical conductivity of solid-dense gold in a temperature range 0.1-10 eV with the *ab-initio* molecular dynamics simulation.

4.2 Effect of laser pulse shape on circuit model

A coil current in the laser-driven coil is usually modeled with the following circuit equations

$$C(t)\frac{\mathrm{d}V}{\mathrm{d}t}(t) = I_d(t) - I(t), \tag{4.1}$$

$$V(t) = L(t)\frac{\mathrm{d}I}{\mathrm{d}t}(t) + I(t)R(t), \tag{4.2}$$

where I_d is a drive current generated by laser-irradiation and expressed as

$$I_d(t) = eh\frac{I_L\pi r_L^2}{2T_{hot}}\Big(1+\frac{eV(t)}{k_BT_{hot}}\Big)e^{-eV(t)/k_BT_{hot}}. \tag{4.3}$$

A square pulse is often used for the incident laser of the laser-driven coil, thus a laser intensity, I_L, and a hot electron temperature, T_{hot}, can be considered as a constant value during the laser pulse. Whereas in the GEKKO-XII facility a Gaussian pulse is used for the incident laser for some technical issues. In this case, I_L and T_h become time-dependent parameters. Here we implemented effects of a laser pulse shape into the circuit model.

In this analysis, we assume that the electron temperature of the plasma generated by the laser-irradiation depends on only the laser intensity at a moment, and the plasma in a past does not affect the current plasma, i.e.,

$$T_{hot}(t) = 12\Big(I_L(t)\lambda_L^2\Big)^{0.42}[\mathrm{keV}]. \tag{4.4}$$

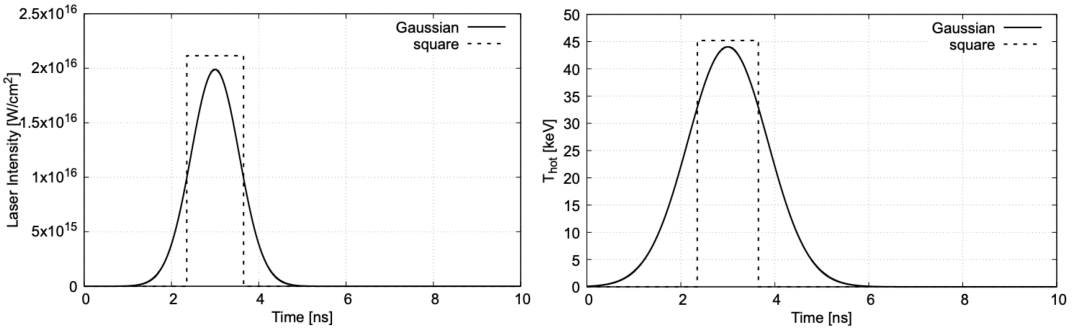

FIGURE 4.1: Temporal evolution of (a) incident laser pulse and (b) hot electron temperature. When the incident laser is the Gaussian pulse, the FWHM of the hot electron temperature extends.

Figure 4.1 (a shows temporal evolutions of laser intensity for square and Gaussian pulse. Here we set the total energy and the pulse duration of the incident laser to be 540 J and 1.3 ns, respectively. A single GXII beam provides this laser pulse[9]. To keep the total energy of the incident laser, the peak intensity of Gaussian pulse is obtained from a relation, $0.94E_0/\tau_L = P_{Gauss}$. Figure 4.1 (b) shows the temporal evolutions of the electron temperature of the generated plasma. Temporal evolution of the electron temperature is surely the same as one of the incident pulse when the waveform is a square pulse. When the waveform is Gaussian pulse, the temporal evolution of the electron temperature is also Gaussian, but the pulse duration becomes long: the pulse duration is 2.0 ns. This comes from the above scaling, $T_h \propto I_L^{0.44}$. Note that this scaling was obtained from low-power (values) laser facilities, thus this would be inaccurate for the high-power lasers such as GXII. Using (4.1) and (4.2) with these laser intensity and electron temperature, we calculated the temporal evolutions of driven voltage and current with two different time constants R/L.

Figure 4.2 (a) shows the temporal evolutions of the generated voltage for square and Gaussian pulses with a coil resistance of 3 Ω. In this case, the time constant L/R is shorter than the pulse duration of the incident laser, thus the generated voltage and coil current are strongly influenced by the pulse form. For a square pulse, the source current is driven instantly, generating the fast-rise voltage. Once the voltage is generated, the generated current i.e. hot electron flow is limited by this potential gap, then the voltage converges a constant value during the pulse. On the other hand, for a Gaussian pulse, the source current increases slowly accompanied with the gradual increase of the electron temperature. Thus, the voltage also increases gradually. The temporal evolution of the generated voltage takes almost the Gaussian form, but the peak comes a bit earlier. Figure 4.2 (b) shows the temporal evolutions of the generated coil current for both pulses. For a square pulse, the coil current rises and decays with the time constant, $L/R = 0.46$ ns. Whereas for the Gaussian pulse, the response speed of the generated current (L/R) is faster than the temporal evolution of the electron temperature and the voltage, thus the temporal evolution of the coil current also takes Gaussian form. Note that the peak time delays with 1.3 ns due to the response.

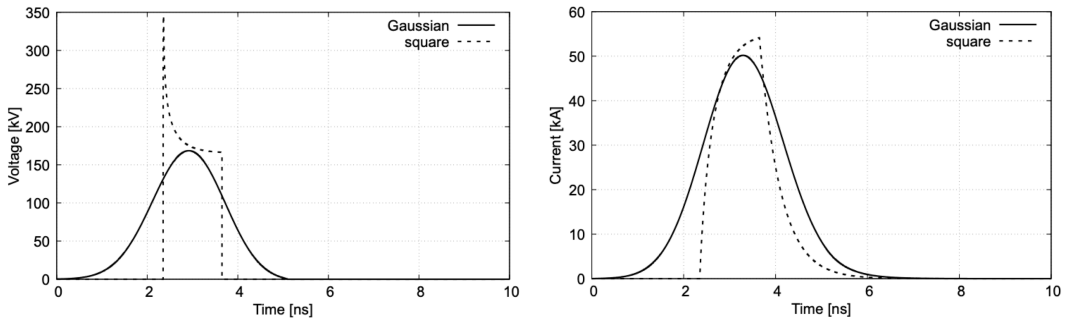

FIGURE 4.2: Calculation results of (a) voltage and (b) current for both square and Gaussian pulse for $R = 3.0\ \Omega$. The FWHM of the voltage extends to 1.8 ns depending on the temporal evolution of hot-electron temperature. The FWHM of the current also extends to 2.1 ns. The current reaches the maximum at 3.3 ns; the peak time of the current is delayed by 0.4 ns compared to the voltage.

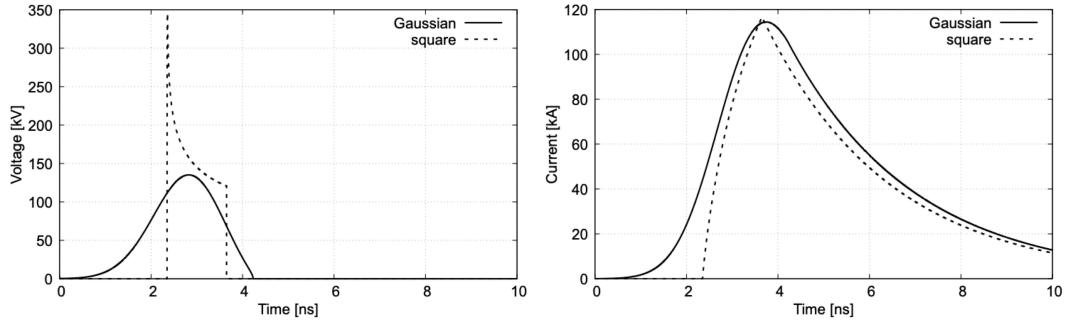

FIGURE 4.3: Calculation results of (a) voltage and (b) current for both square and Gaussian pulse for $R = 0.5\ \Omega$. The FWHM of the voltage extends to 1.8 ns, similar to the calculation with $R = 0.5\ \Omega$. Where as the current does not forms the Gaussian shape because of a long time constant ($L/R \sim 2.7$ ns). The current reaches the maximum at 3.7 ns; the peak time of the current is delayed by 0.9 ns compared to the voltage.

Figure 4.3 (a) shows the temporal evolutions of the generated voltage for square and Gaussian pulses with a coil resistance of 0.5 Ω. In this case, the time constant L/R is longer than the pulse duration of the incident laser, thus the generated voltage and coil current are strongly influenced by the coil inductance. The voltage also takes a totally Gaussian form. The voltage decreases to 0 faster than the Gaussian in the latter half, but this does not affect the coil current much. This fast decay comes from $I_d - I$. Figure 4.3 (b) shows the temporal evolutions of the generated coil current for both pulses. For a square pulse, the coil current does not saturate like Fig. 4.2 (b) in the first half because the time constant is longer than the pulse duration. In the latter half, the coil current decays with the time constant, $L/R = 2.7$ ns or a Gaussian pulse, the temporal evolution of the coil current is similar to one for a square pulse and seems that the current for the square pulse is convoluted with the Gaussian.

4.3 Temporal evolution of coil current

4.3.1 self-consistent circuit model

In the proposed self-consistent circuit model, the coil current can be obtained so that the current obtained by the circuit model and the current obtained by the numerical simulation are self-consistent. This process allows that the circuit model includes the current diffusion and Joule heating. First, temporal evolution of the coil resistance, $R(t)$, can be calculated with the numerical simulation considering the current diffusion and Joule heating. We can solve the circuit equations with the obtained coil resistance to model the coil current, $I(t)$, and voltage, $V(t)$. The obtained voltage, $V(t)$, is now imposed in the numerical simulation to solve for the new $R(t)$. Iterating this loop until $I(t)$ converges sufficiently between iterations provides the self-consistent coil current which includes current diffusion and ohmic heating.

As explained above, the generated voltage becomes almost a Gaussian pulse when the incident laser is a Gaussian pulse. Thus, we imposed the electric field as the Gaussian as a function of temperature initially. The imposed electric field is defined as $E_{back,\phi}(r,z,t) = E_0(t)r/a$, where $E_0(t)$ forms the Gaussian function. The total electric field is expressed as $\vec{E} = \vec{E}_{back} + \vec{E}_{ind}$ where $\vec{E}_{ind}$ is the electric field that results from the time changing magnetic field. The background electric field generates a background magnetic field such that $B_{back,z}(t) = -\int_0^t \mathrm{d}t'(\vec{\nabla} \times \vec{E}_{back}(t'))_z = -\int_0^t \mathrm{d}t' 2E_0(t')/a$. When the imposed electric field, $E_0(t)$, is given by the Gaussian function, the integral in $B_{back,z}(t)$ can be calculated with the Gaussian error function as follow.

$$\int_0^t \mathrm{d}t' e^{-(\alpha t')^2} = \frac{1}{\alpha}\int_0^{\alpha t} \mathrm{d}t' e^{-t'^2} = \frac{\sqrt{\pi}}{2\alpha}\mathrm{erf}(\alpha t) \tag{4.5}$$

The total magnetic field is expressed as $\vec{B} = \vec{B}_{back} + \vec{B}_{ind}$. Here, we focus on the magnetic field generated by the current in the coil $\vec{B}_{ind}$, and thus subtract the background magnetic field, $\vec{B}_{back}$, from the calculated magnetic field, $\vec{B}$.

In this transient simulation, the electric and magnetic fields are numerically calculated from the following Maxwell's equations:

$$\frac{\partial \vec{E}_{ind}}{\partial t} = \frac{1}{\mu\varepsilon}\vec{\nabla} \times \vec{B}_{ind} - \frac{\sigma}{\varepsilon}(\vec{E}_{back} + \vec{E}_{ind}) - \frac{\partial \vec{E}_{back}}{\partial t} \tag{4.6}$$

$$\frac{\partial \vec{B}_{ind}}{\partial t} = -\vec{\nabla} \times (\vec{E}_{ind} + \vec{E}_{back}) - \frac{\partial \vec{B}_{back}}{\partial t} = -\vec{\nabla} \times \vec{E}_{ind} \tag{4.7}$$

Here, the finite differential time domain (FDTD) method[103] was used to solve the Maxwell equations above in a cylindrical coordinate. Yee's algorithm is commonly used in the FDTD method; however, Yee's algorithm is known to generate an incorrect electric field in a conductor. We used the exponential time differential (ETD) method instead of Yee's algorithm to calculate a correct electric field in a conductor. The

azimuthal electric field E_ϕ was calculated with the following difference equation,

$$E^n_{\phi,ind}(i,j) = +e^{-\frac{\sigma}{\epsilon_0}\Delta t}\Big(E^{n-1}_{\phi,back}(i,j) + E^{n-1}_{\phi,ind}(i,j)\Big) + \frac{1-e^{-\frac{\sigma}{\epsilon_0}\Delta t}}{\sigma}\Big(\frac{\partial H_r}{\partial z}(i,j) - \frac{\partial H_z}{\partial r}(i,j)\Big)^{n-\frac{1}{2}}. \tag{4.8}$$

The radial and axial magnetic fields H_r and H_z were calculated with Yee's algorithm as,

$$H^{n+\frac{1}{2}}_{r,ind}(i,j) = H^{n-\frac{1}{2}}_{r,ind}(i,j) + \frac{\Delta t}{\mu_0}\frac{\partial E^n_\phi, ind}{\partial z}(i,j), \tag{4.9}$$

$$H^{n+\frac{1}{2}}_{z,ind}(i,j) = H^{n-\frac{1}{2}}_{z,ind}(i,j) - \frac{1}{r(j)}\frac{\Delta t}{\mu_0}\frac{\partial}{\partial r}\Big(r(j)E_{\phi,ind}(i,j)\Big). \tag{4.10}$$

Simulations were run from 0.0 ns to 10.0 ns. The computation boundary and mesh size were set to be 1000 μm $\times$ 2000 μm and 2 μm, respectively. Here the time step was 6.67 fs with the Courant's restriction.

The coil is modeled in two-dimensional simulation in a cylindrical coordinate, thus the obtained resistance is one for a ring-shaped coil. The actual coil was modeled in a static calculation[104], and the ratio of 2D- and 3D- coil resistances, R_{3D}/R_{2D}, can be calculated to be 1.38. We used this scaling factor to convert the 2D resistance and voltage to 3D values during the iteration process. The simulation shows the temporal evolution of the coil inductance is negligible. Here we set the coil inductance to be 1.37 nH in the actual shape[104].

4.3.2 Electrical conductivity of Nickel wire

Ohmic heating is implemented as $c_V\rho\partial T/\partial t = \sigma(T)|E_\phi + E_{back,\phi}|^2$, where c_V and ρ are the isochoric specific heat and density, respectively. Thermal diffusion is too small to matter at the experimental timescale. The laser-driven coil that is often used in GXII and LULI facilities is made from nickel. The specific heat and the mass density were set to be 440 J/kg K and 7.81 g/cm^3, respectively. And we evaluated the electrical conductivity of nickel with the Lee-More-Desjarlais model because nickel has a lower atomic number and density than gold. Figure 4.4 shows the temperature dependence of liquid nickel calculated with the Lee-More-Desjarlais model. According to Lee-More's criteria [1] , the temperature above 35 eV is classified as region 3, and one below 35 eV is classified as region 5 at a mass density of 7.81 g/cm^3. However, the classification of the region 5 is not adequate. At first, we chose a parameter , p_5, to be 6.2$\times$10^8 for the conductivity,σ_5, in the region 5 to fit the experimental data[105]. A curve of σ_5 does not cross the conductivity,σ_3, for the region 3 at 35 eV. Thus we chose a parameter, p_4, to be 1.2$\times$10^9, to connect σ_5 to σ_3 at 35 eV. The parameters for each region are summarized in table 4.1.

[1] See Fig. B.4 in Appendix B

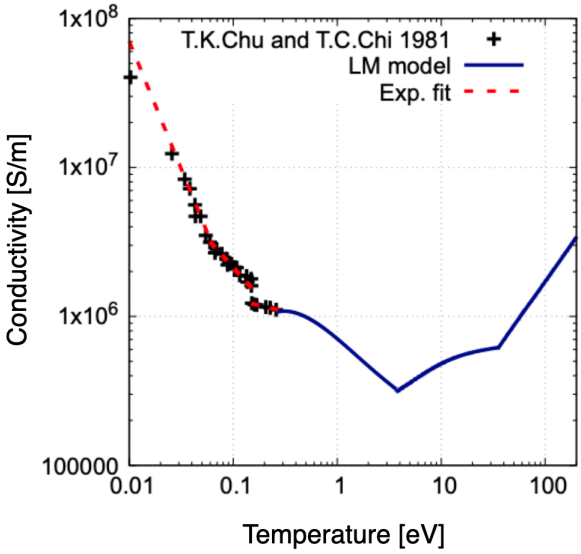

FIGURE 4.4: Temperature dependence of the electrical conductivity of liquid-dense nickel calculated by Lee-More-Desjarlais model. At a temperature below 0.3 eV, the experimental data were used[105].

TABLE 4.1: LMD model for liquid-dense nickel

Temperature [eV]	Region	Parameter
$T \leq 0.3$	Ref.[105]	-
$0.3 \leq T < 3.7$	5	$p_5 = 6.2 \times 10^8$
$3.7 \leq T < 35$	4	$p_4 = 1.2 \times 10^9$
$35 < T$	3	-

4.3.3 Calculation results

Figure 4.5(a) shows the temporal evolution of the coil current and voltage taking into account the temperature dependence of Ni conductivity. As the voltage rises up, the coil current also increases slowly and reaches the maximum at 4.2 ns. Because of the coil inductance, the coil current is delayed 1.4 ns to the voltage. Unlike the voltage evolution, the coil current differs from the Gaussian pulse because the coil resistance changes dramatically until 4.2 ns. After the peak time of 4.2 ns, the current starts to decay with the circuit time constant $L/R(t)$ which is longer than the shut-off time of the voltage.

Also, Fig. 4.5(b) shows a temporal evolution of the coil resistance including the current diffusion and the Joule heating. The coil resistance initially decreases due to the current diffusion until 800 ps. After 800 ps, the surface of the coil starts to be heated up drastically, and total resistance increases (conductivity decreases) and takes the maximum value of 3.1 Ω at 1.9 ns. This represents that the coil temperature increases up to $\sim$ 4 eV until this time according to Fig. 4.4. Note that the coil cross-section is small (ϕ 50 μm), consequently the current density almost diffuses over the cross-section 2 ns. The conductivity of nickel increases above 4 eV, thus the coil resistance starts to decrease over time. The small temporal fluctuation of the coil

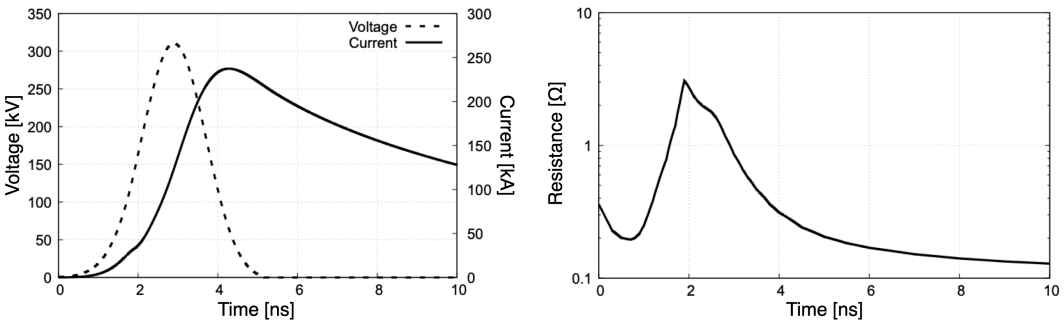

FIGURE 4.5: Temporal evolutions of (a) self-consistent voltage and current and (b) coil resistance. The coil current also increases slowly and reaches the maximum at 4.2 ns. The coil resistance changes drastically until 4.2 ns.

resistance does not affect the temporal evolution of the coil current much.

4.4 Magnetic diffusion into gold cone target

4.4.1 Calculation algorithm

Now we estimate the magnetic diffusion into a gold cone with the obtained coil current as shown in Fig. 4.5. The coil cross-section of the used laser-driven coil is sufficiently small, and we can consider that the generated magnetic field does not depend on the current density distribution much. The transient simulation shows a relation between the coil current and the magnetic field strength at the center of the coil as I [kA] $= 0.395 \times B_{cen}[T]$. Here we implemented the obtained coil current as a current source in the simulation to analyze the magnetic diffusion. The azimuthal electric field E_ϕ in this analysis was calculated with the following difference equation,

$$\begin{aligned} E_\phi^n(i,j) = & -\frac{1-e^{-\frac{\sigma}{\epsilon_0}\Delta t}}{\sigma} j_\phi^{n-1}(i,j) + e^{-\frac{\sigma}{\epsilon_0}\Delta t} E_\phi^{n-1}(i,j) \\ & + \frac{1-e^{-\frac{\sigma}{\epsilon_0}\Delta t}}{\sigma} \left(\frac{\partial H_r}{\partial z}(i,j) - \frac{\partial H_z}{\partial r}(i,j) \right)^{n-\frac{1}{2}}. \end{aligned} \tag{4.11}$$

The magnetic field was solved with the same difference equation (4.9)-(4.10) in the previous section. The target configuration (laser-driven coil and guiding cone) in this simulation is the same as that in the previous MFI integrated experiment[27, 28]. The simulation conditions are set to be same as the transient simulation discussed in the previous section.

The inductive heating was calculated the same as the method in the previous section: the mass density of gold was set to be 19.3 g/cm^3. The electrical conductivity of gold was calculated ranging 300 K - 100 eV with combination of the QMD simulation and the modified Sptizer model. The details are described in Chap. 2.

The thermal diffusion was neglected based on the following discussion. Wiedemann-Franz law $\kappa/\sigma = LT$ is approximately valid for solid state and also WDM states[106, 107], where κ and L are the thermal conductivity and Lorenz number, respectively. The

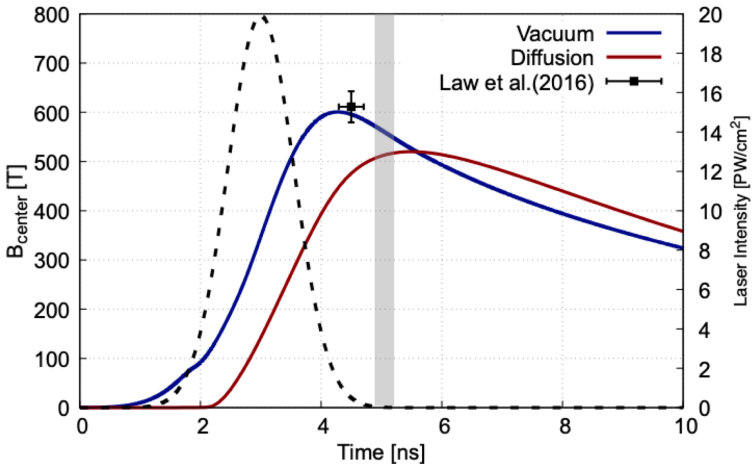

FIGURE 4.6: Temporal evolution of the incident laser pulse, the generated magnetic field, and the magnetic field penetrating the gold cone. The shaded area ranging 4.8 $\sim$ 5.2 ns is timings when the heating laser was irradiated in the previous MFI experiments[27].

thermal conductivity of gold at 3.4 eV is $\kappa = 454.7$ W/(m K) that can be obtained from Wiedemann-Franz law. The thermal diffusion time $c_V \rho l^2/\kappa$ was calculated to be 268 ns for $\rho = 19.3$ g/cm^3 and $l = 7$ μm, therefore the thermal diffusion is negligibly slow compared to the magnetic field diffusion.

The constant value of specific heat of 129 J/(K kg) was used instead of the time-dependent value in our calculation. This value is valid in a several-eV regime. The specific heat consists of two components, one caused by ion lattice vibration and the other by free electrons. The Dulong-Petit law states that the ion lattice specific heat is $3n_i k_B$. At high temperatures above the boiling point, the ion specific heat drops down to $3/2 \cdot n_i k_B$ because the lattice structure is broken and the degrees of freedom for lattice vibration vanish.

The specific heat of electrons is obtained using the chemical potential for a dense plasma, however, the electron specific heat is significantly smaller than the lattice specific heat for low temperature (less than the Fermi temperature $\hbar^2/2m_e \cdot (3\pi^2 n_e)^{2/3}$ ≈ 1 eV). When the temperature increases up to the order of 1 eV, the electron specific heat becomes comparable to the lattice specific heat and its value is $3/2 \cdot n_e k_B$. The average ionization degree for solid gold is calculated to be 1.16 at 3 eV from (2.18), thus the majority of gold atoms are singly ionized. Therefore, the specific heat of gold at several eV is approximately estimated as $3/2 \cdot (n_i + n_e) k_B \sim 3 n_i k_B$, which is almost the same as the cold specific heat.

4.4.2 Simulation results

Figure 4.6 shows the temporal evolution of the incident laser pulse (dashed), the generated magnetic field in a vacuum (solid-blue), and the magnetic field that penetrated the gold cone (solid-red), respectively. The incident laser is a 1.3-ns Gaussian pulse, and approaches the peak at 3 ns. This is same the condition as in Sec. 4.2. In a

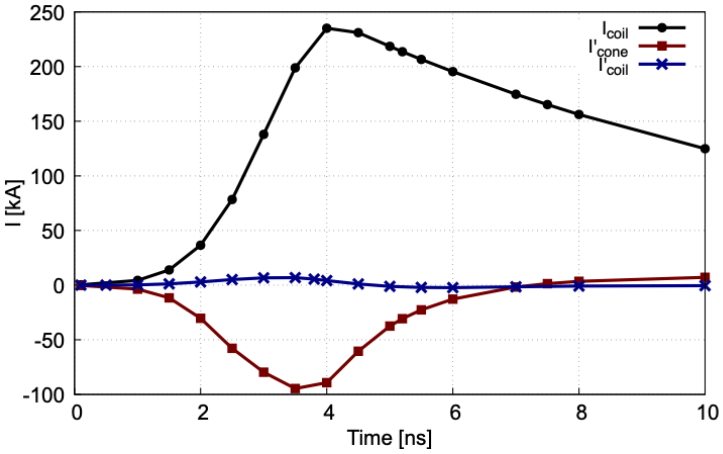

FIGURE 4.7: Temporal evolutions of (1) source current in a coil (black point), (2) the induced current that is caused in the cone-wall (red square), and (3) the induced current that would be caused in the coil due to the mutual induction between the coil and the guiding cone (blue cross), respectively.

vacuum, the magnetic field strength at the center of the coil is proportional to the coil current(I [kA] $= 0.395 \times B_{cen}$ [T]), and takes the same temporal evolution as the coil current. The magnetic field increases up to over time and reaches the maximum strength of 600 T at 4.2 ns. On the other hand, the magnetic field inside a gold cone is almost 0 T until 2.0 ns because the cone keeps high conductivity. When the cone is heated up to the melting temperature (0.12 eV), the magnetic field begins to diffuse into the gold cone and increases gradually. Then the magnetic field penetrating the gold cone reaches the maximum strength of 530 T at 5.5 ns. The maximum magnetic field penetrating the cone is delayed 2.5 ns to the laser peak.

In this calculation, we give the coil current as a current source, i.e., the effect of the mutual induction on the coil current is ignored. We show evidence that this assumption is valid. Figure 4.7 shows temporal evolutions of (1) source current in the coil, (2) the induced current that is caused in the cone-wall, and (3) the induced current that would be caused in the coil due to the mutual induction between the coil and the guiding cone, respectively. As we see in Fig. 4.6, the generated magnetic field begins to penetrate the cone-wall at 2 ns. This indicates that the magnetic field inside the guiding cone is completely canceled out by the magnetic field generated by the induced current in the cone. Thus, the induced current in the cone takes a similar amplitude to the source coil current. After 2 ns, the induced current in the cone also increases as the source coil current increases, but the ratio between the I_{coil} and I'_{cone} decreases. Then, the magnetic field inside the cone becomes not to be canceled sufficiently, causing the magnetic diffusion. In natural, the magnetic field generated by the induced current in the cone would also cause the induced current in the coil due the mutual induction. We estimate this induced current in the coil, I'_{coil}, by treating the induced current in the cone, I'_{cone} as a current source. The calculated I'_{coil} is also shown in Fig. 4.7, and is negligibly small compared to the source coil

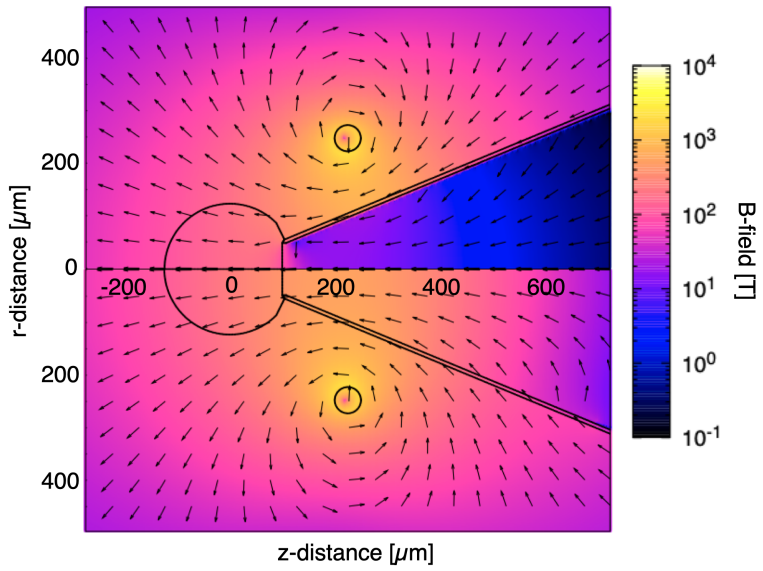

FIGURE 4.8: Spatial distributions of magnetic field at 5.2 ns for two cases: (a) the gold conductivity remains at the cold value ($\sigma = 4 \times 10^7$ S/m) and (b) the temperature dependence of gold conductivity is considered. The applied magnetic field can penetrate through the gold cone wall when the wall temperature increases above the melting point (0.12 eV).

current. For this reason, we conclude that the mutual induction on the coil can be ignored.

In the MFI experiments performed by Sakata *et al.*[27] and Matsuo *et al.*[28], a heating laser was irradiated 1.88 $\sim$ 2.22 ns after the incident laser peak of the laser-driven coil (shaded area in Fig. 4.6), and the maximum coupling efficiency was observed at 2.2 ns after the incident laser. Here we show the magnetic field distribution at 5.2 ns which is 2.2 ns after the laser peak (3 ns).

The upper panel of Fig. 4.8 shows the spatial profile of the magnetic field calculated without consideration of the electrical conductivity change; namely, the electrical conductivity of gold remains at its cold value of 4×10^7 S/m during this computation. In this case, the applied magnetic field cannot penetrate the 7-μm thick cone wall sufficiently because the diffusion time was evaluated as 8.8 ns. On the other hand, the lower panel in Fig. 4.8 shows the profile of the magnetic field with consideration of the temperature dependence of conductivity shown in Fig. 2.8. When the temperature dependence of the conductivity was taken into account, the applied magnetic field can penetrate through the 7-μm thick gold wall at this time.

Our calculation reveals that the temporal change in the electrical conductivity of the cone wall has a significant effect on the magnetic field strength at the cone tip. Figure 4.9 shows line profiles of the magnetic field strength along the cone axis calculated for three cases: the first case is to calculate the profile with the conductivity ($\sigma = 4 \times 10^7$ S/m) of cold gold (neglecting its temperature dependence), the second case is to calculate the profile with consideration of the temperature dependence shown in Fig. 2.8, and the third case is to calculate the profile for the conductivity

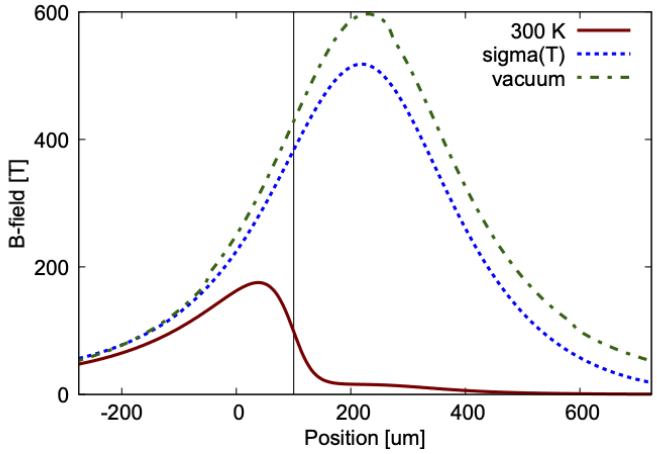

FIGURE 4.9: Line profiles of the magnetic field strength on the axis for three cases. The first case is to calculate the profile with the conductivity ($\sigma = 4 \times 10^7$ S/m) of cold gold (neglecting its temperature dependence), the second case is to calculate the profile with consideration of the temperature dependence shown in Fig. 2.8, and the third case is to calculate the profile for the conductivity ($\sigma = 1{\times}10^{-12}$ S/m) of an insulator. The magnetic field strengths at the tip of the cone are 102, 385, and 427 T, respectively.

($\sigma = 1{\times}10^{-12}$ S/m) of an insulator. The magnetic fields at the tip of the cone are 102 T, 385 T, and 427 T for the respective cases.

The REB guiding requires a magnetic field strength >350 T[79]. The field strength at the cone tip is strong enough to guide the REB to the core when the inductive heating was considered. Although it was assumed that a laser-driven coil was irradiated with a single beam of GEKKO-XII, of which the laser energy was 540 J[9], the laser-driven coil was irradiated at an energy three times larger in the MFI experiment[27]. The magnetic field at the tip of the cone in Ref.[27] could be larger than 350 T, which would be strong enough to guide the REB. Our numerical calculation is verified indirectly by the previous experimental result where laser-to-core coupling was improved twice by application of a strong laser-driven magnetic field to the gold-cone-attached target.

4.5 Summary

In summary, we have developed a 2D-EMD simulation code that considers the inductive heating and temperature dependence of gold conductivity to calculate 2D magnetic field profiles in a gold cone for the MFI scheme. The magnetic field diffuses slowly into the gold cone before the time at which its temperature reaches above the melting point. Consequently, the peak timing of the interior magnetic field strength is delayed 1.3 ns compared to that of the exterior magnetic field strength for a 7μm-thick gold wall and 2.5 ns compared to the incident laser peak. The calculation shows that the field strength at the tip of a gold cone is 385 T, which is sufficiently strong to guide the REB to the fuel core. Numerical analysis in this paper focused on a gold

cone used in the fast ignition inertial confinement fusion, however, the developed simulation code is generally a useful tool for designing and analyzing experiments using strong magnetic field.

Chapter 5

Summary

The goal of this research is to reveal how fast the intense magnetic pulse generated by the laser-driven coil penetrates a metal sample. In this dissertation, the following three topics have mainly been discussed.

1. *ab-initio* evaluation of electrical conductivity in the WDM regime.
2. Modeling of the laser-driven coil with considering the temporal evolution of the current density distribution and the electrical conductivity on the coil cross-section.
3. Magnetic pulse diffusion into a metal considering the temperature dependence of the electrical conductivity.

In Chap. 2, we estimate the electrical conductivity of warm dense gold over a wide-temperature-range 300 K - 100 eV combining the QMD simulation with the modified Spitzer model. For the techniques of strong magnetic-field generation such as a laser-driven coil, a large current of ~ 100 kA causes Joule heating in the coil and changes the coil resistance during the pulse. Also in the magnetized HEDP experiments with the intense magnetic pulse, the temperature of sample materials increases drastically due to the induction heating accompanied with the magnetic diffusion, and the electrical and thermal conduction also changes over time. The temperature dependence of the transport properties such as the electrical conductivity in a wide-temperature range is essential to evaluate the intense-field dynamics described above numerically.

In this research, we calculate the electrical conductivity at a temperature of several-eV and a solid-density with the QMD. However, its scope of application is limited to the region where temperature below 10 eV and density below 2×10^{23} cm^{-3}. Thus, the QMD is not applicable to estimate for example the WDM state in the core of HED planets. The modeling of this high-density WDM state requires exact experimental data. Also, we use the modified Spitzer model and Lee-More-Desjarlais model to calculate the conductivity at a temperature above 7 eV, but these models do not give the correct conductivity much at a temperature below 1 eV and a solid-density. One of the lacks of these models might be the treatment of conduction electrons taking the ionic correlation into account. The improvement of this point will provide more a widely-usable model in future researches.

In Chap. 3, we show the first measurements of a laser-generated magnetic field with a long-duration (10 ns) and high-power (0.5 TW) laser pulse. The results of proton deflectometry measured at different timings indicate that the magnetic field rises rapidly in ~ 1 ns and then increases slowly for the remainder of the laser pulse. The laser-driven diode model coupled with the simulation of ohmic heating and current diffusion shows good agreement with the experimental data. These are the first results of modeling the laser driven coil with an iterative solution method which includes dynamic resistance, current diffusion and space-charge current limitation self-consistently. The dynamics of current diffusion and ohmic heating are simulated with a 2D transient model using cylindrical geometry. The simulation results show that the localized current at the coil edges heats the edges immediately, causing the current density to shift inward as a result of reduced conductivity by ohmic heating.

The central deflection of the proton beam could not be accurately measured at later times in this experiment because the protons could not escape through the exit slots on the coil. We recommend that in future experiments the exit slots should be made large enough to accommodate the significant vertical and horizontal deflections of the protons. Future experiments with larger exit slots will be able to characterize the evolving magnetic field topology and draw conclusions about the dynamics of current diffusion experimentally with the through-hole method.

In Chap, 4, we have developed a 2D-EMD simulation code that considers the inductive heating and temperature dependence of gold conductivity to calculate 2D magnetic field profiles in a gold cone for the MFI scheme. The magnetic field diffuses slowly into the gold cone before the time at which its temperature reaches above the melting point. Consequently, the peak timing of the interior magnetic field strength is delayed 1.3 ns compared to that of the exterior magnetic field strength for a 7μm-thick gold wall and 2.5 ns compared to the incident laser peak. The calculation shows that the field strength at the tip of a gold cone is 385 T, which is sufficiently strong to guide the REB to the fuel core. Numerical analysis in this paper focused on a gold cone used in the fast ignition inertial confinement fusion, however, the developed simulation code is generally a useful tool for designing and analyzing experiments using strong magnetic field.

Appendix A

Application of laser-driven capacitor-coil to target normal sheath acceleration

A laser-driven accelerator generates protons with tens of MeV in energy by a compact, strong, and transient accelerating electric field produced as a result of laser–plasma interactions at relativistic intensities. In previous studies, two- and three-dimensional particle-in-cell simulations revealed that the application of a kT-level axial magnetic field results in an enhancement of proton acceleration via the target normal sheath acceleration mechanism due to reduced lateral electron divergence and improved electron heating efficiency. An experimental investigation of this scheme on the GEKKO-XII and the LFEX facilities found that the number and maximum energy of the accelerated protons decreased with increasing the temporal delay between the pulse driving the external magnetic-field and the pulse accelerating the protons, contrary to the theoretical and numerical expectations. We identify sources responsible for the degradation of the proton beam performance and we propose an alternative experimental setup to mitigate the degradation in future experiments.

A.1 Introduction

Protons with tens of MeV in energy are generated from a laser-produced compact plasma in the laser-driven proton acceleration scheme. Laser-driven protons can be used for various applications: radiography of transient electric and magnetic fields[108], dense matter radiography[109], neutron production via proton–nuclear reactions[110, 111], biomedical therapy[112], and isochoric heating of inertial confinement fusion plasmas[113, 114]. These applications require high flux and energetic protons as well as a high energy conversion efficiency from laser to protons. Experiments were performed to improve these parameters by using various target structures and laser conditions, e.g. an ultra-thin foil[115, 116, 117, 118], micro-structured foil[119, 120, 121], relativistic laser pulse with multi-pico-second duration[122], and interference of laser beams[123].

In the target normal sheath acceleration (TNSA) mechanism[29, 89], an intense laser pulse irradiates a flat foil and generates relativistic electrons at the laser-irradiated surface. A part of the relativistic electrons exit from the foil to a vacuum and generate a strong sheath electric field at the rear surface of the foil. This sheath field accelerates protons from the rear surface of the foil to the vacuum in the surface normal direction. The relativistic electrons diverge generally in the lateral direction , i.e. along the foil. This divergence weakens the strength of the sheath electric field.

Previous studies using multi-dimensional particle-in-cell (PIC) simulations found that application of a strong axial magnetic field to the TNSA scheme increases the maximum proton energy and coupling efficiency from the laser to protons[32, 124, 125] (the magnetic field was above 600 T in these studies). In general, a longitudinal applied magnetic field introduces the following two effects when it comes to relativistic electrons: (1) the magnetic field reduces the divergence of the relativistic electrons[24, 25] and (2) the magnetic field increases the energy gain for electrons moving with a laser pulse due to frequency matching between the cyclotron frequency and the frequency of transverse oscillations caused by the laser that is greatly reduced compared to the laser frequency due to the forward motion of the electrons[126]. Therefore, the expectation is that a strong applied magnetic field should enhance the strength of the sheath field, resulting in generation of a high-flux and high-energy proton beam.

As already stated, a strong magnetic field that can confine the relativistic electrons is required to realize this scheme experimentally. A laser-driven capacitor-coil[7, 8, 77, 76, 9, 47] can produce a 1-kT-level magnetic field. The pulse duration of this magnetic field is about 1 ns, sufficiently long relative to the time scale of proton acceleration. It was confirmed in the previous experiments that the magnetic field generated by a laser-driven magnetic field can indeed radially confine relativistic electrons within a small spot[27, 79].

In this paper, we report results of a recent experimental campaign that utilized GEKKO-XII (GXII) and LFEX laser systems with the goal of demonstrating the enhancement of TNSA in the presence of a magnetic field generated by a laser-driven capacitor-coil. Contrary to our expectations, the experimental results showed that the maximum proton energy and the number of accelerated protons decreased with the introduction of the magnetic field. In order to better understand this result, we performed additional shots where the capacitor-plates were present, but the coil was removed, such that no magnetic field was generated. In this setup, the TNSA performance was also reduced, which points to the laser-irradiated capacitor target as a potential culprit. In this paper, we examine various sources of the proton beam degradation (associated with the capacitor target) that were not accounted for in the PIC simulations of TNSA with an applied magnetic field[32, 124, 125]. We also propose an alternative target design based on our experimental findings that can mitigate these negative effects.

A.2 Experimental setup

The experiment was conducted at the GEKKO-XII (GXII) and LFEX facilities. The experimental setup is schematically shown in Fig. A.1. Three GXII beams were used to generate a strong magnetic field. Each GXII beam (800 ± 50 J of energy at 1053-nm wavelength) was focused to a 50-μm diameter spot on one of the capacitor-plates of the capacitor target. In a previous study that utilized just one GXII beam, the laser-driven capacitor-coil generated a 610 ± 30 T magnetic field at the coil center at 1.5 ± 0.15 ns after the peak of the GXII laser[9]. In our experiment, we used three GXII beams with a total energy of 2400 ± 100 J. The value of the magnetic field in this experiment is estimated to be 1060 T by assuming that the energy of the generated magnetic field scales linearly with the laser energy, i.e. $(610\ \mathrm{T})^2 \times 3 \approx (1060\ \mathrm{T})^2$. The value of 1060 T is strong enough to enhance the TNSA based on our preliminary PIC simulations. The coil had a 500 μm diameter, with the wire diameter being 50 μm.

The LFEX beam (350 ± 50 J of energy at 1053 nm) was irradiated a plastic (CH) foil to accelerate protons via the TNSA mechanism. The CH foil was placed on a 50 μm-thick tantalum to protect the CH foil from radiation and plasma generated at the capacitor-plate. The generated proton beam was recorded with a stack of radiochromic films (RCFs) at 35 mm from the CH foil along the foil normal direction. Holes were punched at the centers of the RCFs. The energy spectra of the laser-accelerated protons going through the holes were measured with the Thomson parabola energy spectrometer. The maximum proton energies were determined using the Thomson parabola energy spectrometer, which ensured a relatively small error compared to the RCF. The maximum energy was evaluated with the RCF when it was below 6 MeV and when the center of the proton beam was not aligned with the hole on the RCF stack. The energy spectra of the accelerated electrons were also measured at 21° from the normal axis of the rear surface of the CH foil.

An aluminum shield was placed 5 mm behind the foil to protect the rear surface of the CH foil from illumination by the uncompressed light of the LFEX beam reflected at the RCF stack surface. The LFEX system emits an uncompressed light pulse ahead of the compressed main pulse. This uncompressed light is specularly reflected on an optical grating surface. The direction of the uncompressed light is tilted a little from that of the compressed light. This is why the uncompressed light does not hit the CH foil, but illuminates the RCF stack behind the CH foil 45 ns before the compressed pulse illumination. The reflected uncompressed light can heat the rear surface of the CH foil, reducing the TNSA performance.

A.3 Results

We measured the energy spectra of the proton beam for various delays between the magnetic field generation and proton acceleration. For the initial delay setting, the GXII and LFEX pulse peaks reached the targets simultaneously. A positive value

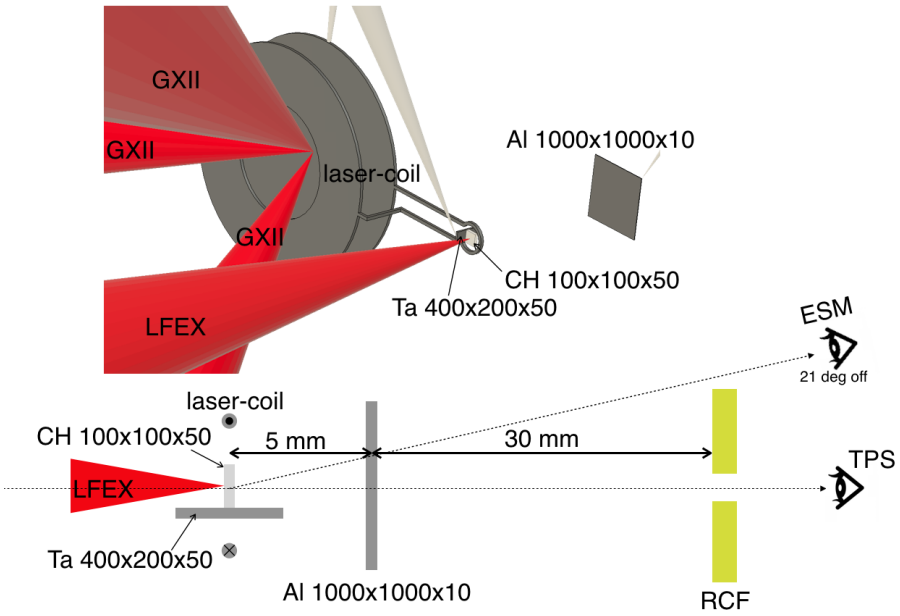

FIGURE A.1: Experimental setup for 3D design and 2D geometry. The CH foil as a proton source was placed on the tantalum plate that protected the CH foil from some types of radiation. The target were placed at the center of the coil. The CH foil and tantalum dimensions were $100 \times 100 \times 50$ μm and $400 \times 200 \times 50$ μm. The aluminum foil was placed 5 mm away from the CH foil, protecting the CH foil from the specular reflection of the uncompressed light of the LFEX. RCFs placed 30 mm away from the aluminum detected the proton beam. The RCFs had a hole at their center to pass protons to a Thomson parabola spectrometer.

for the delay means that the LFEX pulse peak arrives at the CH foil after the GXII pulse peak.

Figure A.2 shows the energy spectra of protons and electrons without the applied magnetic field and with the applied magnetic field for two delays (-260 ps and +180 ps). The proton spectra were measured along the normal direction to the rear surface of a CH foil. All of the proton spectra had a detection limit at 6 MeV because the Thomson parabola energy spectrometer did not detect protons with energies less than 6 MeV. The energy spectra without the laser-driven magnetic field showed the highest maximum energy and the largest number of accelerated protons. On the other hand, when a magnetic field was applied to the CH foil, the maximum energy and the number of protons decreased as the delay increased [see the red and blue markers in Fig. A.2(a)]. The degradation of the maximum energy and the number of protons indicate that the sheath electric field at the rear surface was weakened for unexpected reasons.

The energy spectra of the relativistic electrons were also observed at 21° from the normal direction to the CH foil. In the low energy range (below 1 MeV), the peak shifts towards higher energies in the presence of the magnetic field, as shown in Fig. A.2(b). This shift indicates the possibility of the existence of a plasma around

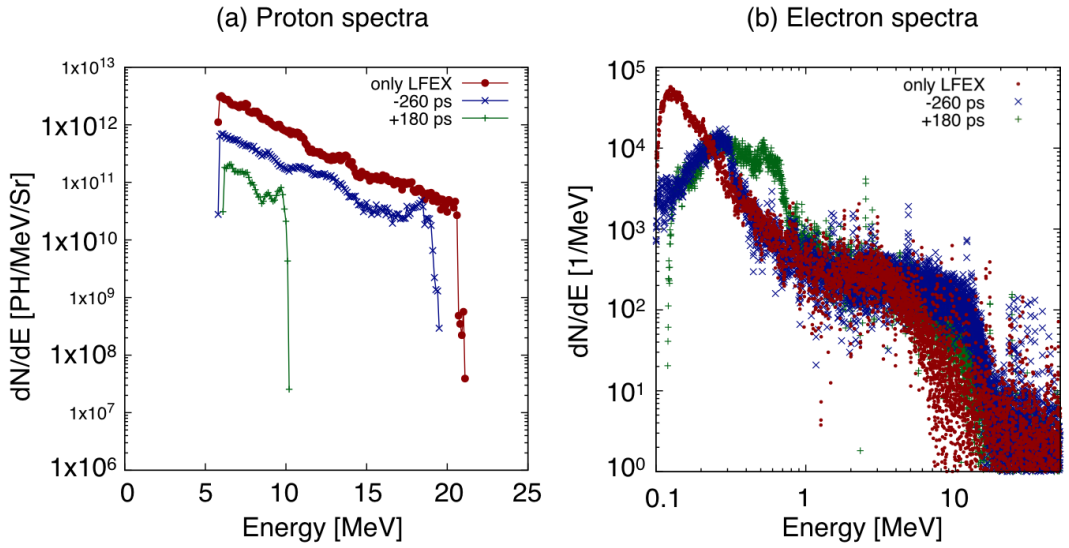

FIGURE A.2: Energy spectra of laser-produced (a) protons and (b) electrons for no magnetic field (red •) and two delays: −260 ps (blue ×), and +180 ps (green +), where a delay is a temporal separation between the application of a magnetic field and the proton acceleration. The proton spectra show that the maximum number and energy of protons decreased with the delay. The electron spectra show an energy shift to higher energy with the delay. This shift indicates the possibility of plasma existing around the CH foil. The plasma surrounding the CH foil can reduce the sheath field, resulting in the reductions seen in (a).

the CH foil. A plasma surrounding the CH foil can reduce the sheath electric field by Debye shielding, causing this shift.

When the laser-driven capacitor-coil is not irradiated by the GXII beams, the LFEX laser interacts with a plasma at a sharp boundary between the CH foil surface and the vacuum because of a high laser pulse contrast of 10^{-11}. When GXII beams irradiate the capacitor-plate of the laser-driven capacitor-coil, a hot plasma stream is incident on the CH foil from the laser-plasma interaction region on the capacitor-plate. LFEX interacts with this plasma stream around the CH foil, generating high-energy relativistic electrons. In addition, the long-scale plasma may decrease the number of low-energy components of the relativistic electrons. The low-energy component of less than 1 MeV is strongly affected by electric and magnetic fields, thus the relativistic electrons are decelerated and scattered by electromagnetic fields in a hot-plasma cloud, which decreases the number of laser-produced electrons entering the detector. As a result, the energy spectra appear to shift to high energy.

The solid line in Figure A.3 shows the dependence of the maximum proton energy on the delay between GXII and LFEX pulses in the presence of the laser-driven capacitor-coil. There is a local maximum for the positive delay at about 200 ps. It possibly indicates the beneficial impact of the applied magnetic field on the laser-driven ion acceleration. However, the proton energy corresponding to this maximum is substantially lower than the energy measured when using only the LFEX beam. The

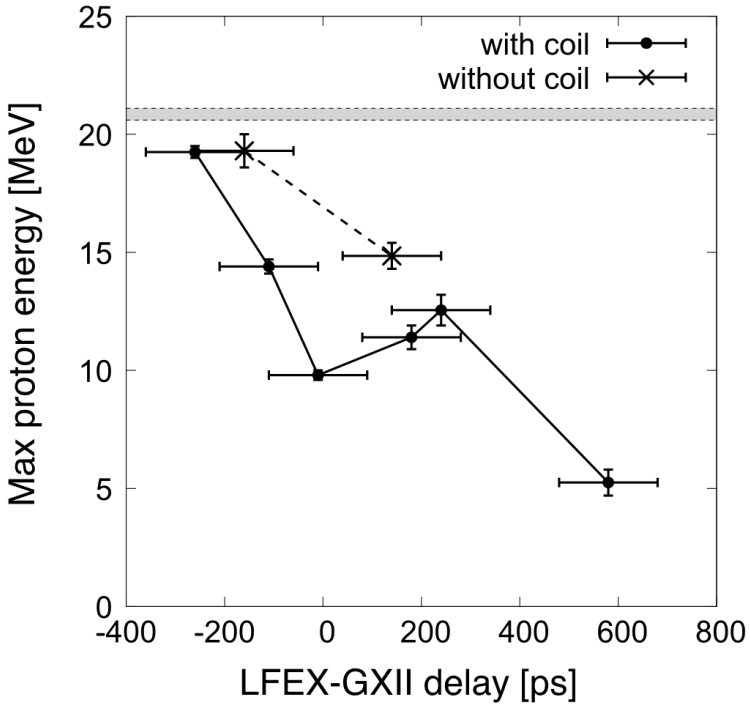

FIGURE A.3: Maximum proton energy as a function of the delay between GXII and LFEX. A positive delay corresponds to LFEX reaching the target after the peak of the GXII beams. The shaded area represents 20.9 ± 0.2 MeV, which is the proton energy range obtained when irradiating only the CH foil. The points and solid line represent the proton energy using a laser-driven capacitor-coil. The crosses and dashed line represent the proton energy when using only capacitor-plates. The maximum energy of the protons decreased with the delay.

maximum proton energy obtained by using only the LFEX pulse is 20.9 ± 0.2 MeV. This energy range is indicated with the shaded region in Fig. A.3.

We have performed two additional shots where the coil was removed, but the capacitor-plates were still irradiated by the GXII beams. The corresponding maximum proton energies are shown in Fig. A.3 with crosses and a dashed line. They are higher than the proton energies in the shots with the laser-driven capacitor-coil. These results indicate that the radiation from the coil heats the CH foil. The preheating due to the radiation causes thermal expansion of the rear surface, resulting in degradation of the TNSA.

A.4 Discussion

Here we estimate the possible sources of the degradation of the TNSA proton performance. The first is the plasma formation at the rear surface of the CH foil. Hot electrons are generated when the capacitor-plate is irradiated by the GXII beams. The GXII laser intensity was 9.40×10^{16} W/cm^2, which was high enough to generate hot electrons of possibly 100-keV temperature[127] and 10^{19}-cm^{-3} density, corresponding to 1% of the critical density for 1053-nm light. The CH foil was placed 3.5 mm

away from the laser focal position on the capacitor-plate. Hot electrons of 100 keV reached the CH foil within 50 ps after GXII irradiation. The Debye length of these hot electrons is evaluated to be 1 μm. This is short enough to suppress the sheath electric field whose typical scale length is 10 $\sim$ 100 μm.

In addition to the hot electrons, X-rays are emitted from the capacitor-plate when it is irradiated by the GXII beams. The energy flux of the X-rays depends on the plasma density and temperature. The bremsstrahlung emitted from the non-thermal hot electrons is calculated assuming that the plasma is fully ionized. Using the parameters for the hot electrons, 100 keV and 10^{19} cm^{-3}, the total energy of the radiation can be evaluated to be $1.42 \times 10^{-34} Z n_e^2 \sqrt{T[\mathrm{K}]}/4\pi = 1.77 \times 10^{-4}$ J. This energy is too weak to heat the CH foil.

Secondly, we estimate the contribution to the preheat from thermal radiation generated by GXII irradiation. The electron density and electron temperature of the plasma on the capacitor-plate are assumed to be 10^{21} cm^{-3} and 5 keV, respectively. Figure A.4 shows the spectra of the X-rays emitted at the source (dashed line) and at the CH foil position (solid line). The atomic kinetics are calculated under the steady-state collisional radiative equilibrium condition. These spectra were calculated with the *FLYCHK* code[128)].

The X-ray spectrum from the capacitor-plate mainly consists of a continuum, but also exhibits intense resonance lines; however, contributions of these resonance lines to the preheat are relatively small compared to the continuum component. The continuum X-rays passing through the tantalum radiation shield heat the CH foil. By integrating the X-ray spectra in the photon energy domain, we obtain the energy flux as 1.84 $\times 10^{21}$ erg/cm^3/sec/sr at the source and 8.02 $\times 10^{16}$ erg/cm^3/sec/sr at the CH position. A 50-μm-thick piece of tantalum can attenuate the radiation flux to 10^4 times weaker. Most of the radiation energy is absorbed within a 10-μm-depth of the tantalum. Surface vaporization and thermal expansion do not occur at the rear surface (CH foil side) of the tantalum shield. To estimate the total energy of the radiation, we assume a plasma column filling a region between the capacitor-plates, with t = 500 ps, V = 0.01 cm^3, and $\Omega_{pla} = 6 \times 10^{-3}$ sr, where t, V, and Ω_{pla} are the irradiation time, volume of the plasma column, and solid angle of the plasma for the CH foil. We obtain a total energy of 2.4×10^{-4} J. This value is also too small to cause preheating of the CH foil.

A few hundred kA of current flowing in a laser-driven capacitor-coil can heat the coil wire by Ohmic heating. Thus, preheating induced by the heated coil must be taken into account. The current, I, in the laser-driven capacitor-coil was measured to be 250 kA in a previous experiment[9)]. The resistivity of nickel increases up to 9.0×10^5 Ohm·m at 3000 K[105)]. This is about 10 times higher than at room temperature. The temperature of the nickel should become higher than 3000 K, but the resistivity changes only several times at around 10 eV. The expansion of the laser-driven capacitor-coil was measured by an optical shadowgraph technique in a previous experiment at the GXII facility[129)]. The energy of the GXII in the experiment was

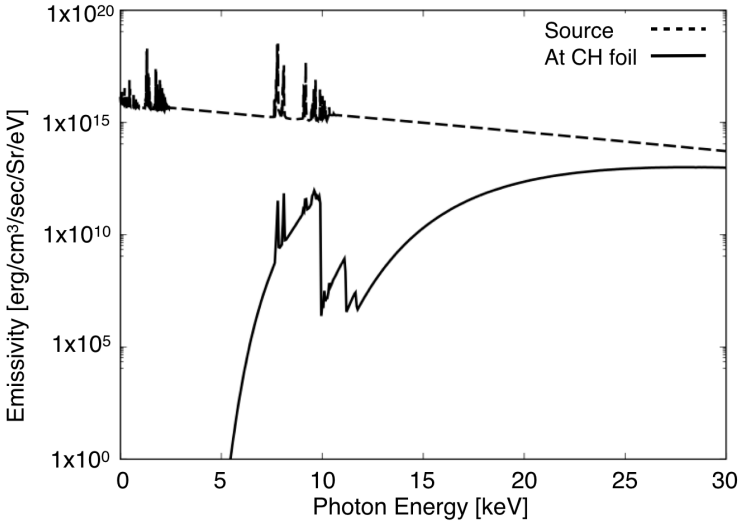

FIGURE A.4: Emissivity spectra of X-rays from a nickel-plasma at $n = 10^{21}$ cm^{-3}, $T = 5$ keV. The dashed line represents X-rays emitted from the thermal plasma that is generated on the capacitor-plates. The solid line represents the X-rays heating the CH foil. These X-rays are absorbed in the 50-μm-thick tantalum plate. The spectra were calculated with the *FLYCHK* code.

2860 J, which was similar to that in our experiment. The expansion speed of the coil surface was evaluated to be 20.8 μm/ns. Considering the resistivity change and the expansion above, the circuit resistance is taken to be 0.83 Ohm. The heating energy was calculated to be $\delta Q = RI^2\Delta t = 51.8$ J with a $\Delta t = 500$-ps duration of the current pulse. The temperature increase, ΔT, for this energy is estimated to be 83.2 eV using the relation $\delta Q = c_V \rho \Delta T$, where c_V is the specific heat of nickel, 440 J/kg/K. The expansion speed of a nickel plasma at 83.2 eV can be calculated to be 16.9 μm/ns, which is approximately close to the experimental result, 20.8 μm/ns. The surface of the coil wire, S_{wire}, is approximately 7.85×10^{-4} cm^2, and the solid angle, Ω_{wire}, for the CH foil is 0.08 sr. The total energy of self-emission from the surface of the entire wire is calculated to be $1.03 \times 10^{17} T^4 \cdot t \cdot S_{wire} \cdot \Omega_{wire}/4\pi = 2.4 \times 10^{-2}$ J. This is large enough to heat the CH foil. The estimation above may be an underestimation. The surface temperature should actually be higher than 80 eV because the current should be higher than 250 kA, and the skin effect induces a localized current at the surface boundary. This may have caused some inconsistency in the expansion speed between the experiment and the estimate. At later times, the wire temperature increases more, and would cause strong heating due to the T^4 dependence.

The estimates above identify that both radiation from the coil and hot electrons from the capacitor-plates reduce the maximum energy and the proton number as observed in Fig. A.2. Here, we propose an alternative schematic design, featuring an "attached-cone" and a "bent-coil", shown in Fig. A.5, to prevent the reductions.

The usage of the bent-coil can prevent the hot electrons from reaching the CH foil. A shortcoming of the laser-driven capacitor-coil used in this experiment is that the coil is located on the same plane as the capacitor-plate that generates the hot

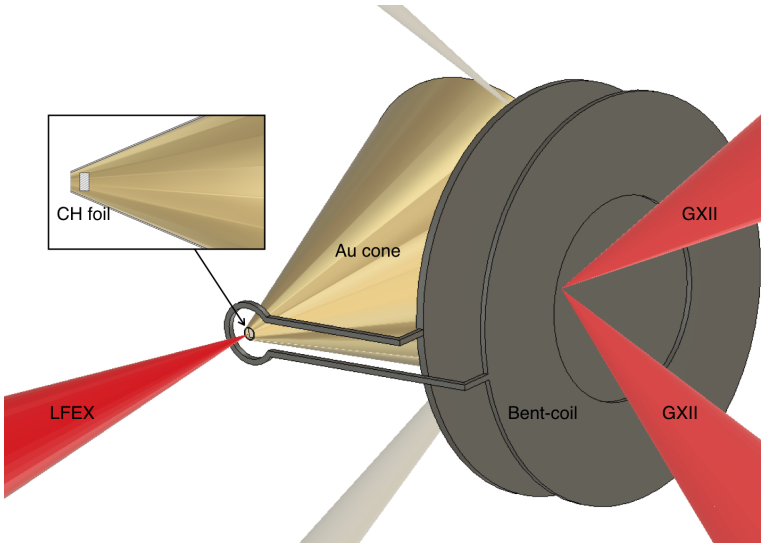

FIGURE A.5: Alternative design, "attached-cone" and "bent-coil", to address hot electron and X-ray pre-heating. The bent-coil can prevent the hot electrons from reaching the CH foil. The attached-cone can absorb the self-emitted X-ray sufficiently.

electrons and X-rays. For the bent-coil, the coil and its straight legs are perpendicular to the capacitor-plates. The laser interacts with the capacitor-plate surface in a direction opposite to that in which the coil is located. The plasma generated at the capacitor-plate will not reach the CH foil placed at the center of the coil. The thermal plasma expansion triggers some problems for magnetic-field measurements by proton-radiography[8, 124] and other methods, besides the enhancement of the TNSA. This may also be solved by the bent-coil.

The attached-cone can protect the CH foil from the heating due to radiation emitted from the coil. The attached-cone is made from 10-μm-thick gold that is sufficiently opaque for the radiation emitted from the coil. The CH foil placed inside the cone can retain the sharpness of the rear surface because the cone wall absorbs the radiation from the coil.

A.5 Summary

In summary, we reveals that the proposed scheme to enhance the proton acceleration by using a laser-driven capacitor-coil is quite sensitive to the hot electrons and X-rays produced by the high-power laser. The number and maximum energy of protons decreased by increasing the delay between the magnetic-field-generation laser pulse and the proton-acceleration laser. An energy shift to high energies was observed in the electron energy spectra as the delay increased. This result indicates the possibility of hot electron irradiation and X-ray preheating. Based on simple estimations, we identify that the sources of the degradations are the hot electrons and the radiation from the laser-driven capacitor-coil. In this paper, we propose an alternative schematic

design for the future experiment, including an attached-cone and a bent-coil, to reduce the degradation. The bent-coil can prevent the hot electrons from reaching the CH foil, while the attached-cone can absorb the X-rays from the coil. In a future experiment, this design will be tested for a successful enhancement of TNSA.

Appendix B

Static and Optical conductivity

B.1 Basis of electrical conduction

Free electrons determine electrical conduction. The magnetic diffusion and skin effect depend on the electrical conductivity. Assume a single electron in oscillating field, $\vec{E} \propto \mathrm{e}^{i\omega t}$, the electron motion can be obtained from the equation of motion,

$$\frac{\mathrm{d}\vec{p}}{\mathrm{d}t} = -m_e\dot{\vec{x}}/\tau - m\omega_0^2\vec{x} - e\vec{E}, \tag{B.1}$$

where ω_0 and τ^{-1} are a resonant frequency due to an atom and a collisional frequency. From this equation, the current density is expressed as

$$\vec{j} = \frac{n_e e^2}{m_e}(\omega_0^2 - \omega^2 - i\omega/\tau)^{-1}\dot{\vec{E}} \tag{B.2}$$

In a conductive material such as plasma and metal, the potential trapping can be neglected ($\omega_0 = 0$), then (B.3) can be reduced to

$$\vec{j} = \frac{n_e e^2\tau/m_e}{1 - i\omega\tau}\vec{E}. \tag{B.3}$$

The optical conductivity, $\sigma(\omega)$, is

$$\sigma(\omega) = \frac{\sigma_0}{1 - i\omega\tau}, \tag{B.4}$$

where $\sigma_0 = n_e e^2\tau/m_e$ is the static conductivity which can be obtained from the limiting process of the optical conductivity. This formula is known as Drude conductivity. In our research, static conductivity plays an important role. Here we introduce how to obtain the static electrical conductivity in WDM state.

B.2 Modified Spitzer-Harm model

In an ideal plasma, the density is two or more orders lower than solid density and the temperature is high enough to assume the fully-ionized, thus the two-bodies Coulomb scattering model is usually applied. In that model, the relaxation time can

be obtained as

$$\tau(n_e, T, Z) = (4\pi\epsilon)^2 \frac{2^{5/2}}{\pi^{3/2}} \frac{\sqrt{m_e}(k_B T)^{3/2}}{e^4 Z^2 n_i \ln\Lambda(n_e, T, Z)}, \tag{B.5}$$

and the conductivity is expressed as

$$\sigma(n_e, T, Z) = (4\pi\epsilon)^2 \frac{2^{5/2}}{\pi^{3/2}} \frac{(k_B T)^{3/2}}{\sqrt{m_e} e^2 Z \ln\Lambda(n_e, T, Z)} \tag{B.6}$$

The $\ln\Lambda$ in the formula above is known as the Coulomb logarithm and represents the sum or cumulative effects of all Coulomb collisions.

B.2.1 Coulomb logarithm

The conductivity in the WDM state is modeled by modifying this Spitzer conductivity in classical approaches. As explained above, the Spitzer conductivity is determined by the Coulomb collision between electron and ion. Thus, the treatment of the Coulomb logarithm that represents the Coulomb collision effect becomes important to model the WDM conductivity. The effect of the Coulomb collision is basically the momentum exchange during a collision as expressed as the second term of RHS of (B.1). The momentum exchange of the electron depends on the distance from the ion core. By taking this into account, the averaged momentum exchange with all ions can be expressed as

$$n_i \frac{\mathrm{d}}{\mathrm{d}t} \int \mathrm{d}x^3 p_{\parallel}(r), \tag{B.7}$$

where r is the distance from the ion core. This integral includes the integration on the cross-section that electron passes through,

$$\int_{b_{min}}^{b_{max}} \frac{\mathrm{d}r}{r} \equiv \ln\Lambda. \tag{B.8}$$

This expression is the most simple definition of the Coulomb logarithm. Here, b_{min} is a distance that the electron gets most closest to the ion core i.e the impact parameter, and b_{max} is the maximum distance that the ion core changes the electron momentum. The minimum impact parameter is usually chosen by the greater between the classical and quantum lengths. A classical and quantum impact parameters are expressed as

$$r_0 = \frac{Ze^2}{4\pi\epsilon_0 m_e v_e^2}, \tag{B.9}$$

and,

$$\lambda_{th} = \frac{h}{\sqrt{2m_e k_B T}} \tag{B.10}$$

respectively. The quantum impact parameter (B.10) is also known as the electron thermal wavelength. Whereas b_{max} is equal to the Debye length (2.8) because the ionic potential is shielded due to the Debye shielding in a classical plasma. Thus the Coulomb logarithm can be obtained as the ratio between the Debye length and impact parameter,

$$\ln \Lambda = \ln(\lambda_D / r_0) = \ln(12\pi n_e \lambda_D^3) \tag{B.11}$$

In the Lee-More model explained later, avoiding that the Coulomb logarithm vanishes when $\lambda_D \sim r_0$, the above expression is modified as

$$\ln \Lambda = \frac{1}{2} \ln \left(1 + \frac{b_{\max}^2}{b_{\min}^2}\right). \tag{B.12}$$

D.K.Kim and I.Kim used the Zollweg-Lieberman's Coulomb logarithm which can be used for only fully-ionized plasma in their model[130]:

$$\ln \Lambda = \frac{1}{2} \ln \left(1 + 1.4 \frac{a_z^2 + \lambda_D^2}{r_0^2}\right) \tag{B.13}$$

Zaghloul pointed out that this expression is an often-used inaccurate fitting formula for the classical cross-section integral[49] and used the Coulomb logarithm obtained from the classical binary cutoff theory[131],

$$\ln \Lambda = \frac{\pi}{2} \sin(1.5/\Lambda) \left(1 - \frac{2}{\pi} \left(\mathrm{S_i}(1.5/\Lambda) + \frac{\mathrm{C_i}(1.5/\Lambda)}{\tan(1.5/\Lambda)}\right)\right), \tag{B.14}$$

$$\Lambda \approx 2.4287 \frac{\lambda_D}{\lambda_{th}} \left(1 + \left(\frac{1}{2.4287} \frac{a_z/\lambda_D}{r_0/\lambda_{th}}\right)^4\right)^{0.25}, \tag{B.15}$$

where, $\mathrm{S_i}(x), \mathrm{C_i}(x)$ are sine and cosine integrals as shown in Fig. B.1. The effect of the Coulomb collision between electron and ion is correctly described by modifying the Coulomb logarithm like the above.

B.2.2 Ionization state

The Spitzer conductivity assumes the fully-ionized plasma and Z in (B.6) is usually treated as the atomic number. Whereas the WDM is a kind of a partially-ionized plasma, so the ionization state should be described. Here we introduce several ionization models.

Thomas-Fermi model

The most famous model is the Thomas-Fermi model. The Thomas-Fermi model provides physical properties such as ionic potential, Hartree (electron) potential, and

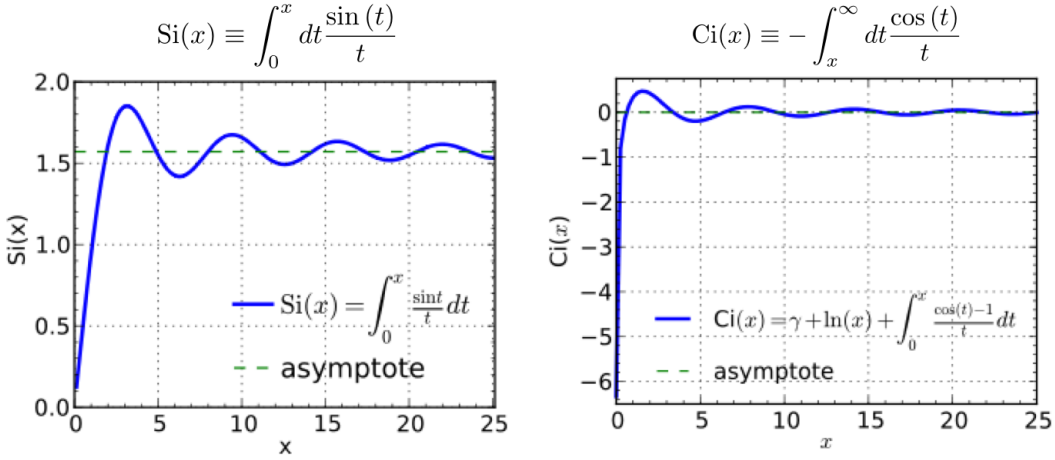

FIGURE B.1: Sine and cosine integrals. These functions are defined by each expression above each figures. The asymptotes of sine and cosine integral are $\pi/2$ and 0, respectively.

kinetic energy with only the electron density. The electron density in the Thomas-Fermi model is based on one in the Fermi model and includes the potential effect,

$$n_e(r) = \frac{4\pi}{h^3}(2m_e k_B T)^{3/2} F_{1/2}\Big(\frac{\mu(T) + eV(r)}{k_B T}\Big) \tag{B.16}$$

The ionic potential of a single atom and Hartree (electron) potential can be obtained only with the electron density, $n_e(r)$, as

$$U_{ion} = \int \mathrm{d}r^3 e n_e(r) V_{ion}(r) = \int \mathrm{d}r^3 n_e(r) \frac{Ze^2}{r}, \tag{B.17}$$

$$U_H = \int \mathrm{d}r^3 n_e(r) V_H(r) = \frac{1}{2} e^2 \int \mathrm{d}r^3 n_e(r) \int \mathrm{d}r'^3 \frac{n_e(r')}{|r - r'|}, \tag{B.18}$$

and total potential energy is

$$U_{ion} + U_H = e \int \mathrm{d}r^3 n_e(r) \Big(V_{ion}(r) + V_H(r)\Big) = e \int \mathrm{d}r^3 n_e(r) V(r). \tag{B.19}$$

Here, $V(r)$ is total potential and a solution of the Poisson equation,

$$\vec{\nabla}^2 V(r) = -\frac{1}{\varepsilon_0}\Big(Ze\delta(r) - e n_e(r)\Big). \tag{B.20}$$

The electron density satisfies both (B.20) and (B.16) simultaneously, and is a self-consistent solution of them. When the electron temperature is absolute zero ($T = 0$) or is sufficiently less than the Fermi temperature ($T_e \ll T_F$), the electron kinetic energy at a position r is calculated as

$$\langle t(r) \rangle = \int_0^{\varepsilon_F} \mathrm{d}\varepsilon D(\varepsilon) f(\varepsilon, 0) \varepsilon = \frac{3\hbar^2}{10 m_e} (3\pi^2)^{2/3} [n_e(r)]^{5/3} \tag{B.21}$$

The total kinetic energy, U_{kin}, can be expressed as a function of electron density,

$$U_{kin} = \int \mathrm{d}^3 r \langle t(r) \rangle = \frac{3\hbar^2}{10 m_e} (3\pi^2)^{2/3} \int \mathrm{d}^3 r [n_e(r)]^{5/3}. \tag{B.22}$$

Then, the total energy of the electron system can be expressed as a function of the electron density.

$$U_{ion}[n_e(r)] + U_H[n_e(r)] + U_{kin}[n_e(r)] = E_{tot}[n_e(r)] \tag{B.23}$$

This is the most important conclusion of the Thomas-Fermi model. Additionally, the kinetic energy in a finite temperature system is written as

$$\langle t(r) \rangle = \int_0^\infty \mathrm{d}\varepsilon D(\varepsilon) f(\varepsilon, T) \varepsilon = \frac{4\pi k_B T}{h^3} (2 m_e k_B T)^{3/2} F_{3/2}\Big(\frac{\mu(T) + eV(r)}{k_B T} \Big) \tag{B.24}$$

This expression is also an implicit functional of the electron density because the total potential is a functional of the electron density.

The electron density in the Thomas-Fermi model (B.16) is described by adding the ionic potential to the Fermi (free electron) gas model; electrons are trapped in a region defined within the Wigner-Seitz radius, in other words, each atom is independent in this model. Thus, in the Thomas-Fermi model, the ionization degree can be obtained with

$$Z_{\mathrm{TF}} = \frac{n_e(r_0)}{n_i} = \frac{4}{3} \pi r_0^3 n_e(r_0). \tag{B.25}$$

Here, the free electron density is treated as the electron density on the boundary surface, $n_f = n_e(r_0)$. The electron density, $n_e(r)$, in the Thomas-Fermi model generally requires a numerical calculation. The analytical fitting of this ionization degree was developed by More as shown in Fig. B.2[132]. Figure B.3 shows a comparison of each ionization model for 2.5-g/cm^3 aluminum. The TF ionization shows a good agreement with PROPACEOS [1] at a temperature above 10 eV as shown in Fig. B.3(a). On the other hand, TF ionization does not agree with PROPACEOS at a temperature below 10 eV. This inconsistency comes from the fact that the TF model ignores any inter-atomic interaction and confine all electrons within an ion sphere.

Smooth blend with TF and single-ionization Saha

Lee and More adopted this TF ionization in their conductivity model; however Desjarlais pointed out that the TF model does not describe the metal-insulator transition, a feature of WDM, and proposed an ionization model coupled with a single-ionization Saha model[133]. A single-ionization Saha equation is given by

$$\frac{n_1 n_e}{n_0} = 2 \frac{U_1}{U_0} \Big(\frac{2\pi m_e k_B T}{h^2} \Big)^{3/2} \exp\Big(- \frac{I_0^{\mathrm{eff}}}{k_B T} \Big). \tag{B.26}$$

[1] PRism OPACity and Equation Of State code. PROPACEOS can calculate the equation of state for elements $Z < 36$.

Table 10.2 Analytic formulas for the ionization degree $Z_{\text{ion}} = Q(Z, \rho, T)$ approximating the TF result 10.46. Formulas are given for cold ionization ($T = 0$), and for arbitrary ρ in units of g/cm^3 and T in eV (More 1985).

$T = 0$, any density	
$\rho_1 = \rho/(AZ)$	ρ in g/cm^3
$x = \alpha(\rho/ZA)^\beta$	$\alpha = 14.3139$
$Z_{\text{ion}} = Zx/(1 + x + \sqrt{1 + 2x})$	$\beta = 0.6624$
Any temperature and density	
$\rho_1 = \rho/(AZ)$	
$T_1 = T(\text{eV})/Z^{4/3}$	$a_1 = 0.003323$
$T_f = T_1/(1 + T_1)$	$a_2 = 0.9718$
$A = a_1 T_1^{a2} + a_3 T_1^{a_4}$	$a_3 = 9.26148 \times 10^{-5}$
$B = -\exp(b_0 + b_1 T_f + b_2 T_f^7)$	$a_4 = 3.10165$
$C = c_1 T_f + c_2$	$b_0 = -1.7630$
$Q_1 = A\rho_1^B$	$b_1 = 1.43175$
$Q = (\rho_1^C + Q_1^C)^{1/C}$	$b_2 = 0.31546$
$x = \alpha Q^\beta$	$c_1 = -0.366667$
$Z_{\text{ion}} = Zx/(1 + x + \sqrt{1 + 2x})$	$c_2 = 0.983333$

FIGURE B.2: Fitting function of Thomas-Fermi ionization of (B.25). This fitting formula was proposed by More[132], and re-printed by Atzeni[102].

This equation gives the ionization degree, Z_{Saha},

$$Z_{\text{Saha}} = \frac{n_e}{n_a} = \frac{1}{2}\left(\sqrt{K^2 + 4K} - K\right), \tag{B.27}$$

$$K = \frac{2}{n_a}\frac{U_1}{U_0}\left(\frac{2\pi m_e k_B T}{h^2}\right)^{3/2} \exp\left(-\frac{I_0^{\text{eff}}}{k_B T}\right), \tag{B.28}$$

where, I_0^{eff} is the effective first ionization energy. Note that $n_e = n_1$, $n_0 = n_a - n_e$. Combining Z_{Saha} with Z_{TF}, we can obtain the effective ionization degree,

$$Z_{\text{ion}} = Z_{\text{Saha}} + Z_{\text{Saha}}^{2/Z_{\text{TF}}^2}(Z_{\text{TF}} - Z_{\text{Saha}}). \tag{B.29}$$

This model describes ionization more correctly at low a temperature and density as shown in Fig. B.3(a). The corrected ionization (B.29) show a good agreement with PROPACEOS at temperature below 10 eV.

Non-ideal Saha equation

More exact ionization can be obtained from the non-ideal Saha equation expressed as

$$\frac{n_z n_e}{n_{z-1}} = 2\frac{U_z}{U_{z-1}}\left(\frac{2\pi m_e k_B T}{h^2}\right)^{3/2} \exp\left(-\frac{I_z^{\text{eff}}}{k_B T}\right), \tag{B.30}$$

where h, n_z, and U_z are the Planck constant, number density, and internal portion function for z-fold ions. In general, this equation cannot be solved analytically. Zaghloul introduced a simple formulation and solution strategy of Saha equation with an iterative method[134]. The Saha equation describes any ionization states, n_z, as a function of temperature and density. The word "ideal" means a situation that an electron is removed from a single atom infinitely far. In a many-body system such as plasma, the Debye screening and the pressure ionization should be taken into account.

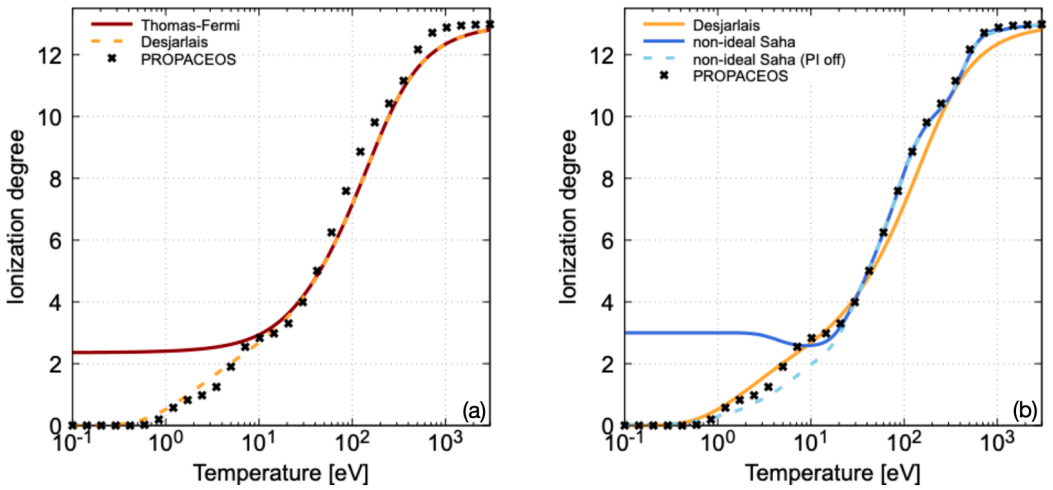

FIGURE B.3: Temperature dependence of ionization degree of 2.5-g/cm^3 aluminum. (a) shows the Thomas-Fermi ionization, Desjarlais correction, and PROPACEOS results. Thomas-Fermi model overestimates the ionization degree at low temperature ($<$ 10 eV), while Desjarlais correction reproduces the ionization degree at low temperature ($<$ 10 eV). (b) shows Desjarlais correction, non-ideal Saha, and PROPACEOS results. The non-ideal Saha calculate the ionization degree exactly at high temperature ($>$ 10 eV), but at low temperature ($<$ 10 eV), this model also overestimates the ionization degree as same as Thomas-Fermi ionization.

The most simple correction is to consider the screening effect. The correction term of the ionization energy is expressed as

$$\Delta I_z = \frac{(z+1)e^2}{4\pi\varepsilon_0 R^*}, \tag{B.31}$$

where, R^* is the screening length. This correction represents that the electron can escape from the ionic potential when it R^* away from the ion. For the screening length, R^*, in a classical plasma, the Debye lengths (2.6) - (2.8) are often used. In the low-density WDM, $F'_{1/2}/F_{1/2}$ are multiplied to (2.6) to describe the electron degeneracy. But, the Fermi integral requires a numerical calculation. Lee and More proposed

$$\frac{1}{\lambda_{DH}^2} = \frac{n_e e^2}{\varepsilon_0 k_B \sqrt{T_e^2 + T_F^2}} + \frac{n_i (Z_{\rm ion} e)^2}{\varepsilon_0 k_B T_i} \tag{B.32}$$

to avoid numerical calculation of $F'_{1/2}/F_{1/2}$[135]. This approximation gives an exact value within 5% error compared with the results of numerical calculation. But the screening length based on the Debye length is not correct at a high density where the Debye length is too short compared to the atomic radius. Zaghloul proposed the length for such a high density,

$$\sqrt{\lambda_{DH}^2 + \frac{2}{3}a_z^2}, \tag{B.33}$$

coupled with the result of the ion sphere model, where ion sphere radius is written as

$$a_z = \left(\frac{3(z+1)}{4\pi n_a(1+Z_{\text{ion}})}\right)^{1/3}. \tag{B.34}$$

The ionization degree calculated with the non-ideal Saha model is shown in Fig. B.3(b). The non-ideal Saha model provides the exact ionization degree for high temperatures above 10 eV compared to PROPACEOS. However, at a low temperature below 10 eV, the ionization degree is overestimated as same as TF ionization. The non-ideal Saha model is still not adequate in such a low-temperature and high-density state. As temperature decreases, ionization degree also decreases, but the screening length (B.33) converges to $2/3 \cdot a_z$ at low temperature and causes an excess pressure ionization in a region $2/3 \cdot a_z < r < a_z$ as shown in Fig. B.3(b). Changing a coefficient of 2/3 to 1 gives a lower ionization degree at low temperature as shown in the dashed blue line because the pressure ionization does not take place. The coefficient of a_z corresponds to the ratio of the pressure ionization at low temperature.

In another treatment of the non-ideal correction, D.K.Kim and I.Kim treated the correction term, ΔI_z, as

$$\Delta I_{z+1} = \left(\frac{\partial \Delta F_C}{\partial n_z}\right)_{T,V} - \left(\frac{\partial \Delta F_C}{\partial n_{z+1}}\right)_{T,V} - \left(\frac{\partial \Delta F_C}{\partial n_e}\right)_{T,V}, \tag{B.35}$$

considering the excess of the excess free energy as follow[50].

$$\Delta F_C = n_i k_B T\Big(f_C^{ii}(\Gamma_{ii}) + f_C^{ee}(\Gamma_{ee}, a_e/a_B)\Big) + n_e k_B T f_C^{ee}(\Gamma_{ee}, \Theta_e). \tag{B.36}$$

The above was explained more detail in Ref[136].

B.2.3 Contribution of Neutral collision

The electrical conductivity strongly depends on the Coulomb collision (electron-electron, ion-electron collision) described above. The collisions with neutral particles also take place in a partially-ionized plasma such as WDM and contribute to the electrical conduction. The conductivity due to the neutral collision is expressed as

$$\sigma_{en} = \sqrt{\frac{\pi}{8 m_e k_B T}} \frac{n_e e^2}{n_0 \bar{Q}_{en}}, \tag{B.37}$$

where, $\bar{Q}_{en}$ is a cross-section of neutral collisions. The effective conductivity is obtained from a following liner-mixture rule with the conductivity due to the Coulomb collisions.

$$\frac{1}{\sigma} = \frac{1}{\sigma_{ei}} + \frac{1}{\sigma_{en}} \tag{B.38}$$

This formula is commonly used to estimate the conductivity in the WDM. A value of 2.0×10^{-18} m^2 is often used as the cross-section of neutral collisions, $\bar{Q}_{en}$. More

rigorously, also the cross-section based on the Born approximation,

$$\bar{Q}_{en} = \frac{\pi^3(\alpha_D/2r_0a_B)^2}{A_k^2 + 3B_k kr_0 + 7.5C_k(kr_0)^2 - 3.4D_k(kr_0)^3 + 10.6668E_k(kr_0)^4} \tag{B.39}$$

is used to evaluate the neutral conductivity[133].

B.2.4 Electron degeneracy

The above describes only modifications of the Coulomb logarithm and the ionization degree in the Spitzer formula, not the electron degeneracy effect in the Spitzer formula itself. To describe the degeneracy effect, the electron correlation function,

$$\gamma(Z_{ion}) = \frac{3\pi}{32}\Big(1 + \frac{153Z_{ion}^2 + 509Z_{ion}}{64Z_{ion}^2 + 345Z_{ion} + 288}\Big), \tag{B.40}$$

is multiplied to the Spitzer formula.

B.3 Transport properties in linear response

In the linear response theory, physical transport properties can be expressed as

$$\vec{j}_i = \Sigma_k L_{ik}\vec{F}_k \tag{B.41}$$

where, $\vec{j}_i$ is a flux density, $\vec{F}_k$ is a driver. For the electrical and thermal transport,

$$\vec{j}_e = L_{11}\vec{E} + L_{12}\frac{1}{eT}(-\vec{\nabla}T) \tag{B.42}$$

$$\vec{j}_q = L_{21}\frac{1}{e}\vec{E} + L_{22}\frac{1}{e^2T}(-\vec{\nabla}T) \tag{B.43}$$

In the case of $\vec{\nabla}T = 0$,

$$\vec{j}_e = L_{11}\vec{E} \tag{B.44}$$

This equation corresponds to the Ohm's law, leading to $L_{11} = \sigma$, where σ is the electrical conductivity. Also, the Peltier coefficient can be obtained as

$$\Pi = \frac{|\vec{j}_q|}{|\vec{j}_e|} = \frac{1}{e}\frac{L_{21}}{L_{11}}. \tag{B.45}$$

In the case of $\vec{j}_e = 0$, the Seebeck coefficient can be obtained as follow.

$$\vec{E} = -\frac{1}{eT}\frac{L_{12}}{L_{11}}(-\vec{\nabla}T) = -S\vec{\nabla}T \tag{B.46}$$

Further, the heat flux can be written using equations above,

$$\vec{j}_q = \frac{1}{L_{11}} \frac{1}{e^2 T} (L_{11}L_{22} - L_{12}L_{21})(-\vec{\nabla} T) \tag{B.47}$$

This represents Fourier's law, thus, the thermal conductivity is

$$\kappa = \frac{1}{e^2 T} \frac{\det(L_{ij})}{L_{11}}. \tag{B.48}$$

As described above, the matrix L_{ij} can be obtained with the linear response theory and is important for the transport properties.

B.4 Lee-More model

Lee and More developed a semi-classical conductivity model which is the most famous and useful model to describes the transport properties in WDM state[135]. In this model, the electron occupation is approximately expressed as the perturbed Fermi-Dirac distribution,

$$f = f_0 - \tau_c \frac{\partial f_0}{\partial \varepsilon} \vec{v} \cdot \Big(- e\vec{E} + \frac{\varepsilon - \mu}{T} \vec{\nabla} T \Big). \tag{B.49}$$

where, f_0 is the Fermi-Dirac distribution. This equation can be derived from the linearized Boltzmann equation. From this equation, the Onsager coefficients, L_{ij}, can be obtained as

$$L_{ij} = L^{(m)} = e^2 \int \mathrm{d}p^3 \frac{2}{h^3} \Big(\frac{\partial f_0}{\partial \varepsilon} \Big) \varepsilon^m \tau_c |\vec{v}|^2 \tag{B.50}$$

where, $m = i + j - 2$ and τ_c is the collisional relaxation time in the Spitzer-Harm model. The coefficient $L^{(0)}$ provides the electrical conductivity,

$$\sigma = \frac{n_e e^2 \tau}{m} A^\alpha, \tag{B.51}$$

where the coefficient, A^α, in Eq.(B.51) is defined as

$$A^\alpha \big(\frac{\mu}{k_B T} \big) = \frac{4}{3} \frac{F_2(\mu/k_B T)}{[1 + e^{-\mu/k_B T}] F_{1/2}(\mu/k_B T)^2}. \tag{B.52}$$

Lee and More introduced the approximation fitting of A^α as,

$$A = \frac{\sum_{i=1}^{N} a_i \big(\ln (1 + e^{\mu/kT}) \big)^{i-1}}{1 + \sum_{i=2}^{M} b_i \big(\ln (1 + e^{\mu/kT}) \big)^{i-1}} \tag{B.53}$$

where, $a_1 = 3.39$, $a_2 = 3.47{\times}10^{-1}$, $a_3 = 1.29{\times}10^{-1}$, $b_2 = 5.11{\times}10^{-1}$, $b_3 = 1.24{\times}10^{-1}$.

In this model, the collisional relaxation time, τ, is selected depending on the temperature-density region. Fig. B.4 shows the divisions of τ by the temperature-density region and is introduced by Lee and More. The used formulas for each region

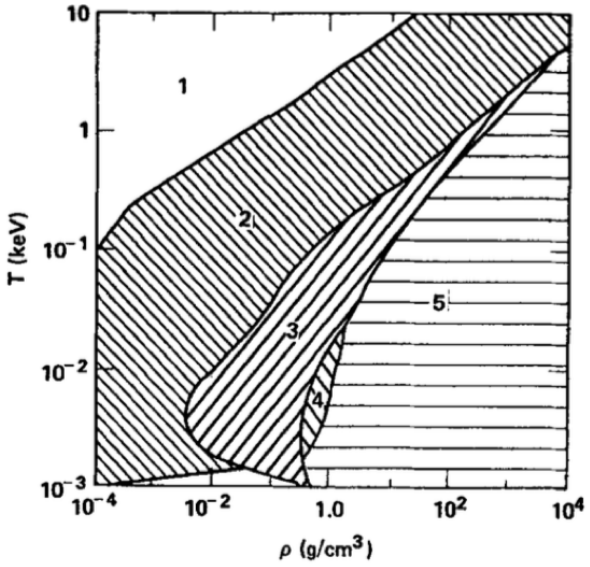

FIGURE B.4: $\rho - T$ phase diagram proposed by Lee and More. In the Lee-More model, the collisional relaxation time or Coulomb logarithm are different in each region.

TABLE B.1: Formulas in each region

region	argument	formula
1	screening length	$b_{\max} = \lambda_{DH}$
2	screening length	$b_{\max} = R_0$
3	Coulomb logarithm	$\ln \Lambda = 2.0$
4	mean free path	$l = R_0$
5	mean free path	$l = 50 \frac{T_m}{\gamma T} R_0,$

are summarized in table B.1. For regions 1-3, the collisional relaxation time τ is expressed as

$$\tau = \frac{3\sqrt{m}(k_B T)^{3/2}}{2\sqrt{2}\pi Z_{\text{ion}}^2 e^4 n_i \ln \Lambda} [1 + e^{-\mu/k_B T}] F_{1/2}\left(\frac{\mu}{k_B T}\right), \tag{B.54}$$

and this expression is similar to the modified Spitzer conductivity. Here, the Coulomb logarithm is used as (B.12) in this formula, thus the screening length is a key parameter in these regions. The state categorized in region 1 is similar to a classical plasma and the screening length is (B.32). The state categorized in region 2 is a little high density, and the screening length is approximately the inter-atomic distance (B.34). In the state categorized in region 3, the Coulomb logarithm is set to be 2 as a minimum value. Using (B.54) and (B.52), (B.51) can be expressed as

$$\sigma = \frac{\sqrt{2}}{\pi} \frac{(k_B T)^{3/2}}{\sqrt{m_e} e^2 Z_{\text{ion}} \ln \Lambda} \frac{F_2(\mu/k_B T)}{F_{1/2}(\mu/k_B T)}. \tag{B.55}$$

In the non-degeneracy limit ($\mu/k_BT \to -\infty$),

$$\lim_{x\to-\infty}\Big((1+e^{-x})F_{1/2}(x)\Big) = \frac{\sqrt{\pi}}{2}, \tag{B.56}$$

$$\lim_{x\to-\infty}\Big(\frac{4}{3}\frac{F_2(x)}{(1+e^{-x})F_{1/2}(x)^2}\Big) = \frac{32}{3\pi}, \tag{B.57}$$

(B.55) provides the Spitzer conductivity (B.6). This means that the electro-correlation function (B.40) corresponds to $F_2(\mu/k_BT)/F_{1/2}(\mu/k_BT)$, which describes the electron degeneracy. The Fermi-Dirac integral seen in (B.54),

$$F_n\big(\frac{\mu}{k_BT}\big) = (k_BT)^{-(n+1)}\int_0^\infty \mathrm{d}\varepsilon\ \varepsilon^n f(\varepsilon), \tag{B.58}$$

cannot be calculated analytically except for some special cases. Thus, some fitting formulas were developed[137, 138]. For example, the analytical fitting of Fermi-Dirac integral for $n = 1/2$ is given by

$$F_{1/2}(x) = \frac{\sqrt{\pi}}{2\big(\mathrm{e}^{-x}+\phi_1(x)\big)}, \tag{B.59}$$

$$\phi_1(x) = \frac{3}{4}\sqrt{\pi}\nu(x)^{-3/8}, \tag{B.60}$$

$$\nu(x) = 50 + x^4 + +33.6x(1-0.68\mathrm{e}^{-0.17(x+1)^2}). \tag{B.61}$$

In regions 4 and 5, the relaxation time is expressed as $\tau = l/\bar{v}_e$, where, the averaged electron velocity, $\bar{v}_e$, is defined as

$$\frac{1}{2}m_e\bar{v}_e^2 = \sqrt{\varepsilon_F^2 + \Big(\frac{3}{2}k_BT\Big)^2}. \tag{B.62}$$

In the region 4, the mean free path is p_4R_0, where p_4 is a fitting parameter. This should be chosen to fit the conductivity for the region 4 to one for the region 3 at the boundary between regions 3 and 5 shown in Fig. B.4. In region 5, the mean free path is $50p_5R_0T_m/T$, where p_5 is a fitting parameter and T_m is a melting point. The parameter, p_5, should be chosen to fit the conductivity for the region 5 to the experimental results.

B.5 Kubo-Greenwood conductivity

The Onsager kinetic coefficients, L_{ij}, are generally determined in a quantum linear response as follows.

$$L_{ij} = (-1)^{(i+j)}\frac{2\pi e^2\hbar^2}{3m_e^2\Omega\omega}\sum_{n,m,\vec{k}}\Big(f(\varepsilon_m^{\vec{k}}) - f(\varepsilon_n^{\vec{k}})\Big)\Big|\langle\psi_n^{\vec{k}}|\vec{\nabla}|\psi_m^{\vec{k}}\rangle\Big|^2$$
$$\times(\varepsilon_n^{\vec{k}}-\mu)^{(i-1)}(\varepsilon_m^{\vec{k}}-\mu)^{(j-1)}\delta(\varepsilon_n^{\vec{k}}-\varepsilon_m^{\vec{k}}-\hbar\omega), \tag{B.63}$$

where Ω is a system volume. This formula is also known as Chester-Thellung kinetic coefficients. Especially, the electrical conductivity obtained as L_{11},

$$\sigma(\omega) = \frac{2\pi e^2\hbar^2}{3m_e^2\Omega\omega} \sum_{n,m,\vec{k}} \left(f(\varepsilon_m^{\vec{k}}) - f(\varepsilon_n^{\vec{k}})\right) \left|\langle\psi_n^{\vec{k}}|\vec{\nabla}|\psi_m^{\vec{k}}\rangle\right|^2 \delta(\varepsilon_n^{\vec{k}} - \varepsilon_m^{\vec{k}} - \hbar\omega) \tag{B.64}$$

is called as Kubo-Greenwood (KG) conductivity which is widely used in warm dense matter physics. The Kubo-Greenwood conductivity represents an optical response to external excitation, namely, optical conductivity, thus this formula depends on the photon energy (light frequency) not only the electron temperature. The calculation of the optical conductivity with the Kubo-Greenwood formula requires the electron states, i.e system wave functions and dispersion relation (band structure) which includes the energy levels and the density of states. The static conductivity can be obtained by taking a limiting process of $\omega \to 0$ same as the Drude conductivity (B.4). The Onsager coefficients (B.63) also provide the thermal conductivity with the relation B.48. Note that $\kappa(\omega)$ has a physical meaning only for $\omega \to 0$.

One of the methods to estimate the optical conductivity experimentally is the laser pump-probing method[139, 140, 141] If the laser light irradiates the sample material, we can measure its reflected and transmitted light. The intensity of the transmitted light is attenuated to $\exp(-\omega n_i x/c)$, where n_i is the imaginary part of the refraction index. On the other hand, the reflectivity of incident light can be expressed as

$$\frac{(1-n_r)^2 + n_i^2}{(1+n_r)^2 + n_i^2} \tag{B.65}$$

thus, the real and imaginary parts of the refraction index, n_r and n_i, can be obtained from the reflected and transmitted light. The complex refraction index is related to the dielectric functions by the relations $\epsilon = n^2$, namely,

$$\epsilon_r = n_r^2 - n_i^2 \tag{B.66}$$

$$\epsilon_i = 2n_r n_i, \tag{B.67}$$

and the dielectric function is related to the optical conductivity with $i\omega\epsilon_0(1-\epsilon)$, namely,

$$\sigma_r = \omega\epsilon_0\epsilon_i \tag{B.68}$$

$$\sigma_i = \omega\epsilon_0(1-\epsilon_r). \tag{B.69}$$

Therefore, we can evaluate the optical conductivity with measuring the reflected and transmit light. This technique is often used to measure the optical conductivity of two-temperature warm dense matter.

List of Works

Publications

Principal author (reviwed)

1. H. Morita, B. B. Pollock, C. S. Goyon, G. J. Williams, K. F. F. Law, S. Fujioka, and J. D. Moody, "Dynamics of laser-generated magnetic fields using long laser pulses", Physical Review E, 103, 033201 (2021)

2. H. Morita, A. Arefiev, T. Toncian, J. J. Santos, D. Golovin, S. Shokita, T. Mori, K. F. F. Law, H. Li, R. Takizawa, K. Matsuo, A. Morace, A. Yogo, and S. Fujioka, "Application of laser-driven capacitor-coil to target normal sheath acceleration", High Energy Density Physics, 37, 100874 (2020)

3. H. Morita, A. Sunahara, Y. Arikawa, H. Azechi, and S. Fujioka, "Numerical analysis of pulsed magnetic field diffusion dynamics in gold cone target", Physics of Plasmas, 25, 094505(2018)

Co-author (reviwed)

1. K. F. F. Law, Y. Abe, A. Morace, Y. Arikawa, S. Sakata, S. Lee, K. Matsuo, H. Morita, Y. Ochiai, C. Liu, A. Yogo, K. Okamoto, D. Golovin, M. Ehret, T. Ozaki, M. Nakai, Y. Sentoku, J. J. Santos, E. Humieres, P. Korneev, and S. Fujioka, "Relativistic magnetic reconnection in laser laboratory for testing an emission mechanism of hard-state black hole system", Physical Review E, 102, 033202(2020)

2. S. Lee, D. Kawahito, N. Iwata, Y. Sentoku, K. F. F. Law, S. Sakata, H. Morita, K. Matsuo, Y. Arikawa, K. Shigemori, T. Sano, H. Nagatomo, K. Mima, H. Azechi, R. Kodama, and S. Fujioka, "Two-color laser-plasma interactions for efficient production of non-thermal hot electrons", High Energy Density Physics, 36, 100843(2020)

3. H. Li, S. Sakata, T. Johzaki, X. Tang, K. Matsuo, S. Lee, K. F. F. Law, Y. Arikawa, Y. Ochiai, C. Liu, J. Nishibata, R. Takizawa, H. Morita, H. Azechi, Y. Sentoku, and S. Fujioka, "Enhanced relativistic electron beams guiding effect and laser heating induced by self-generated magnetic field in fast ignition", High Energy Density Physics, 36, 100773(2020)

4. K. Matsuo, N. Higashi, N. Iwata, S. Lee, S. Sakata, T. Johzaki, H. Sawada, Y. Iwasa, K. F. F. Law, H. Morita, Y. Ochiai, M. Hata, S. Kojima, Y. Abe, A. Sunahara, T. Shiroto, A. Morace, A. Yogo, M. Nakai, H. Sakagami, T. Ozaki, K. Yamanoi, T. Norimatsu, Y. Nakata, S. Toktia, J. Kawanaka, H. Shiraga, K. Mima, H. Azechi, T. Sano, H. Nagatomo, R. Kodama, Y. Arikawa, Y. Sentoku, and S. Fujioka, "Creation of Peta-Pascal Pressure by Direct Interaction between Multi-Pico-Second Intense Laser Pulse and Dense Plasma" Physical Review Letter, 108, 091104(2019)

5. C. Liu, K. Matsuo, S. Ferri, H. K. Chung, S. Lee, S. Sakata, K. F. F. Law, H. Morita, B. B. Pollock, J. D. Moody, and S. Fujioka, "Design of Zeeman spectroscopy experiment with magnetized silicon plasma generated in the laboratory", High Energy Density Physics, 33, 100710(2019)

6. S. Kojima, M. Hata, N. Iwata, Y. Arikawa, A. Morace, S. Sakata, S. Lee, K. Matsuo, K. F. F. Law, H. Morita, Y. Ochiai, A. Yogo, H. Nagatomo, T. Ozaiki, T. Johzaki, A. Sunahara, H. Sakagami, Z. Zhang, S. Tosaki, Y. Abe, J. Kawanaka, S. Tokita, M. Nakai, H. Nishimura, H. Shiraga, H. Azechi, Y. Sentoku, and S. Fujioka, "Electromagnetic field growth triggering super-ponderomotive electron acceleration during multi-picosecond laser-plasma interaction", Communications Physics, 2, 99 (2019)

7. S. Sakata, T. Johzaki, S. Lee, H. Morita, K. Matsuo, R. Kodama, Y. Arikawa, Y. Sentoku, and S. Fujioka, "Simple Analysis of Laser-to-Core Energy Coupling Efficiency with Magnetized Fast Isochoric Laser Heating", Plasma and Fusion Research, 14, 3404138(2019)

8. S. Sakata, S. Lee, H. Morita, T. Johzaki, H. Sawada, Y. Iwasa, K. Matsuo, K. F. F. Law, A. Yao, M. Hata, A. Sunahara, S. Kojima, Y. Abe, H. Kishimoto, A. Syuhada, T. Shiroto, A. Morace, A. Yogo, N. Iwata, M. Nakai, H. Sakagami, T. Ozaki, K. Yamanoi, T. Norimatsu, Y. Nakata, S. Tokita, N. Miyanaga, J. Kawanaka, H. Shiraga, K. Mima, H. Nishimura, M. Bailly-Grandvaux, J. J. Santos, H. Nagatomo, H. Azechi, R. Kodama, Y. Arikawa, Y. Sentoku, and S. Fujioka, "Magnetized Fast Isochoric Laser Heating for Efficient Creation of Ultra-High-Energy-Density States", Nature Communications, 9, 3937(2018).

CONFERENCE PRESENTATIONS

International conferences

1. H. Morita, T. Ogitsu, S. Hu, S. Fujioka, and F. Graziani, "Ab-initio Calculation for Electrical Conductivity of Warm Dense Gold", OPTICS and PHOTONICS International Congress 2020, HEDSp-05, 2020.4.20-24, online

2. H. Morita, A. Arefiev, J. J. Santos, T. Toncian, K. F. F. Law, D. Golovin, S. Shokita, T. Mori, R. Takizawa, J. Nishibata, H. Li, C. Liu, Y. Arikawa, M.

Alessio, A. Yogo, and S. Fujioka, “Application of Laser-driven Strong Magnetic Field to Proton Acceleration via Target Normal Sheath Acceleration”, 11th International Conference on Inertial Fusion Sciences and Applications, 2P81, 2019.09.23, Osaka

3. J. D. Moody, H. Morita, B. B. Pollock, C. S. Goyon, G. J. Williams, D. A. Mariscall, S. Patankar, G. B. Logan, J. S. Ross, M. W. Scherlock, S. Fujioka, K. F. F. Law, and V. Tikhonchuk, “Time-dependence of laser-driven magnetic field generation for long laser drive conditions”, 60th Annual Meeting of the American Physical Society, 2018.11.8, Portland, Oregon

4. A. Sunahara, H. Morita, T. Johzaki, H. Nagatomo, S. Fujioka, and A. Hassanein, “Diffusion of external magnetic fields into the cone-in-shell target in the fast ignition”, 59th Annual Meeting of the APS, 2017.10.25, Milwaukee, Wisconsin

Domestic conferences

1. H.Morita, T.Ogitsu, S.Hu, S.Fujioka, and F.Graziani, “Ab-initio Calculation for Electrical Conductivity of Warm Dense Gold”, 76th Annual Meeting of the Physical society of Japan, 19aD13-5, 2020.3.19, Aichi

2. H. Morita, A. Arefiev, J. J. Santos, T. Toncian, K. F. F. Law, D. Golovin, S. Shokita, T. Mori, R. Takizawa, J. Nishibata, H. Li, C. Liu, Y. Arikawa, M. Alessio, A. Yogo, and S. Fujioka, “Application of Laser-driven Strong Magnetic Field to Proton Acceleration via Target Normal Sheath Acceleration”, 2019 Autumn Meeting of the Physical society of Japan, 10aK22-11, 2019.09.22, Gifu

3. H. Morita, B. B. Pollock, C. S. Goyon, G. J. Williams, K. F. F. Law, V. Tikhonchuk, S. Fujioka, and J. D. Moody, “Dynamics of Laser-driven Magnetic Field gerenrated with Long Pulse Laser Irradiation”, 74th Annual Meeting of the Physical society of Japan, 15aK310-10, 2019.03.15, Fukuoka

4. H. Morita, B. B. Pollock, K. F. F. Law, A. Sunahara, Y. Arikawa, J. D. Moody, and S. Fujioka, “Generation of long-pulse Magnetic Field and its Diffusion into Gold cone-guide Target for MFI scheme”, 12th Joint Conference on Fusion Energy of the Japan Society of Plasma Science and Nuclear Fusion Research, 28P-118, 2018.06.28, Shiga

5. H. Morita, K. F. F. Law, S. Sakata, K. Matsuo, S. Lee, S. Kishimoto, S. Kambayashi, Y. Ochiai, Y. Arikawa, T. Jhozaki, A. Sunahara, H. Azechi, and S. Fujioka, “Magnetic Field Diffusion Dynamics with Consideration of Inductive Heating and Dependence of Conductivity on Material Temperature”, Plasma Conference 2017, 23Ep-07, 2017.11.23, Hyogo

6. H.Morita, K.F.F.Law, S.Sakata, K.Matsuo, S.Lee, H.Kishimoto, Y.Arikawa, A.Sunahara, A.Yogo, H.Azechi, S.Fujioka, "Magnetic diffusion into the Fusion target", 72th Annual Meeting of the Physical society of Japan, 20aC32-4, 2017.03.20, Osaka

Symposium and workshops

1. H. Morita, A. Sunahara, B. B. Polock, K. F. F. Law, S. Sakata, K. Matsuo, S. Lee, Y. Arikawa, J. D. Moody, T. Johzaki, H. Azechi, and S. Fujioka, "Duration and Strength Dependencies for Pulsed Magnetic Field Diffusion", JIFT Japan-US workshop on Theory and simulation on the high field and high energy density physics, 2018.03.28, Hiroshima, Japan

Honors and Awards

1. Accepted in research fellowship for young scientists of Japan Society for the Promotion of Science 2020
2. Accepted in Japan/U.S. Cooperation in Fusion Research and Development 2019
3. Accepted in Osaka University scholarship for overseas research activities 2018
4. Accepted in highly Ph.D. education program at Osaka university 2017

Bibliography

[1] H. J. Schneider-muntau, J. Toth and H. W. Weijers, *Generation of the Highest Continuous Magnetic Fields*, IEEE Trans. Appl. Supercond., **14**, 2 (2004):pp. 1245–1252

[2] K. Kindo, *100 T magnet developed in Osaka*, Phys. B Condens. Matter, **294-295**, (2001):pp. 585–590

[3] A. I. Bykov, M. I. Dolotenko, N. P. Kolokolchikov, V. D. Selemir and O. M. Tatsenko, *VNIIEF achievements on ultra-high magnetic fields generation*, Phys. B Condens. Matter, **294-295**, (2001):pp. 574–578

[4] S. Takeyama and E. Kojima, *A copper-lined magnet coil with maximum field of 700 T for electromagnetic flux compression*, J. Phys. D. Appl. Phys., **44**, 425003 (2011)

[5] F. S. Felber, M. M. Malley, M. A. Palmer and A. L. Velikovich, *Compression of ultrahigh magnetic fields in a gas-puff Z pinch*, Phys. Fluids, **31**, 2053 (1988)

[6] J. P. Knauer, O. V. Gotchev, P. Y. Chang, D. D. Meyerhofer, O. Polomarov, R. Betti, J. A. Frenje, C. K. Li, M. J. Manuel, R. D. Petrasso, J. R. Rygg and F. H. Śguin, *Compressing magnetic fields with high-energy lasers*, Phys. Plasmas, **17**, 056318 (2010)

[7] S. Fujioka, Z. Zhang, K. Ishihara, K. Shigemori, Y. Hironaka, T. Johzaki, A. Sunahara, N. Yamamoto, H. Nakashima, T. Watanabe, H. Shiraga, H. Nishimura and H. Azechi, *Kilotesla Magnetic Field due to a Capacitor-Coil Target Driven by High Power Laser*, Sci. Rep., **3**, 1170 (2013)

[8] J. J. Santos, L. Giuffrida, S. Fujioka, Z. Zhang, P. Korneev, R. Bouillaud, S. Dorard, D. Batani, M. Chevrot, J. E. Cross, R. Crowston, J. l. Dubois, J. Gazave, G. Gregori, E. Humières, S. Hulin, K. Ishihara, S. Kojima, E. Loyez, J. R. Marquès, A. Morace, P. Nicolaï, O. Peyrusse, A. Poyé, D. Raffestin, J. Ribolzi, M. Roth, G. Schaumann, F. Serres, V. T. Tikhonchuk, P. Vacar and N. Woolsey, *Laser-driven platform for generation and characterization of strong quasi-static magnetic fields*, New J. Phys., **17**, 083051 (2015)

[9] K. F. F. Law, A. Morace, S. Sakata, K. Matsuo, S. Kojima, S. Lee, X. Vaisseau, Y. Arikawa, A. Yogo, K. Kondo, Z. Zhang, C. Bellei, J. J. Santos, S. Fujioka, H. Azechi, K. F. F. Law, A. Morace, S. Sakata, K. Matsuo and S. Kojima,

Direct measurement of kilo-tesla level magnetic field generated with laser-driven capacitor-coil target by proton deflectometry, Appl. Phys. Lett., **108**, 091104 (2016)

[10] C. Courtois, A. D. Ash, D. M. Chambers, R. A. D. Grundy and N. C. Woolsey, *Creation of a uniform high magnetic-field strength environment for laser-driven experiments*, J. Appl. Phys., **98**, 054913 (2005)

[11] G. Fiksel, W. Fox, L. Gao and H. Ji, *A simple model for estimating a magnetic field in laser-driven coils*, Appl. Phys. Lett., **109**, 134103 (2016)

[12] V. T. Tikhonchuk, M. Bailly-Grandvaux, J. J. Santos and A. Poyé, *Quasi-stationary magnetic field generation with a laser-driven capacitor-coil assembly*, Phys. Rev. E, **96**, 023202 (2017)

[13] K. F. F. Law, Y. Abe, A. Morace, Y. Arikawa, S. Sakata, S. Lee, K. Matsuo, H. Morita, Y. Ochiai, C. Liu, A. Yogo, K. Okamoto, D. Golovin, M. Ehret, T. Ozaki, M. Nakai, Y. Sentoku, J. J. Santos, E. Humières, P. Korneev and S. Fujioka, *Relativistic magnetic reconnection in laser laboratory for testing an emission mechanism of hard-state black hole system*, Phys. Rev. E, **102**, 033202 (2020)

[14] S. P. D. Mangles, P. A. Norreys, M. Wei, M. Zepf and K. Krushelnick, *Laboratory measurements of 0.7 GG magnetic fields generated during high-intensity laser interactions with dense plasmas*, Phys. Rev. E, **70**, 026401 (2004)

[15] C. Plechaty, R. Presura, S. Stein, D. Martinez, S. Neff, V. Ivanov and Y. Stepanenko, *Penetration of a laser-produced plasma across an applied magnetic field*, High Energy Density Phys., **6**, (2010):pp. 258–261

[16] B. Albertazzi, A. Ciardi, M. Nakatsutsumi, T. Vinci, J. Béard, R. Bonito, J. Billette, M. Borghesi, Z. Burkley, S. N. Chen, T. E. Cowan, T. Herrmannsdörfer, D. P. Higginson, F. Kroll, S. A. Pikuz, K. Naughton, L. Romagnani, C. Riconda, G. Revet, R. Riquier, H. P. Schlenvoigt, I. Y. Skobelev, A. Y. Faenov, A. Soloviev, M. Huarte-Espinosa, A. Frank, O. Portugall, H. Pépin and J. Fuchs, *Laboratory formation of a scaled protostellar jet by coaligned poloidal magnetic field*, Science (80-.)., **346**, 6207 (2014)

[17] D. B. Schaeffer, W. Fox, D. Haberberger, G. Fiksel, A. Bhattacharjee, D. H. Barnak, S. X. Hu, K. Germaschewski and R. K. Follett, *High-Mach number, laser-driven magnetized collisionless shocks*, Phys. Plasmas, **24**, 122702 (2017)

[18] T. Byvank, J. T. Banasek, W. M. Potter, J. B. Greenly, C. E. Seyler and B. R. Kusse, *Applied axial magnetic field effects on laboratory plasma jets: Density hollowing, field compression, and azimuthal rotation*, Phys. Plasmas, **24**, 122701 (2017)

[19] P. Mabey, B. Albertazzi, G. Rigon, J.-R. Marquès, C. A. J. Palmer, J. Topp-Mugglestone, P. Perez-Martin, F. Kroll, F.-E. Brack, T. E. Cowan, U. Schramm, K. Falk, G. Gregori, E. Falize and M. Koenig, *Laboratory Study of Bilateral Supernova Remnants and Continuous MHD Shocks*, Astrophys. J., **896**, 167 (2020)

[20] K. Matsuo, H. Nagatomo, Z. Zhang, P. Nicolai, T. Sano, S. Sakata, S. Kojima, S. H. Lee, K. Fai, F. Law, Y. Arikawa, Y. Sakawa, T. Morita and Y. Kuramitsu, *Magnetohydrodynamics of laser-produced high-energy-density plasma in a strong external magnetic field*, Phys. Rev. E, **95**, 053204 (2017)

[21] L. J. Perkins, B. G. Logan, G. B. Zimmerman and C. J. Werner, *Two-dimensional simulations of thermonuclear burn in ignition-scale inertial confinement fusion targets under compressed axial magnetic fields*, Phys. Plasmas, **20**, 072708 (2013)

[22] J. S. Green, V. M. Ovchinnikov, R. G. Evans, K. U. Akli, H. Azechi, F. N. Beg, C. Bellei, R. R. Freeman, H. Habara, R. Heathcote, M. H. Key, J. A. King, K. L. Lancaster, N. C. Lopes, T. Ma, A. J. MacKinnon, K. Markey, A. McPhee, Z. Najmudin, P. Nilson, R. Onofrei, R. Stephens, K. Takeda, K. A. Tanaka, W. Theobald, T. Tanimoto, J. Waugh, L. Van Woerkom, N. C. Woolsey, M. Zepf, J. R. Davies and P. A. Norreys, *Effect of laser intensity on fast-electron-beam divergence in solid-density plasmas*, Phys. Rev. Lett., **100**, 1 (2008):pp. 1–4

[23] K. L. Lancaster, J. S. Green, D. S. Hey, K. U. Akli, J. R. Davies, R. J. Clarke, R. R. Freeman, H. Habara, M. H. Key, R. Kodama, K. Krushelnick, C. D. Murphy, M. Nakatsutsumi, P. Simpson, R. Stephens, C. Stoeckl, T. Yabuuchi, M. Zepf and P. A. Norreys, *Measurements of energy transport patterns in solid density laser plasma interactions at intensities of 5 × 1020Wcm-2*, Phys. Rev. Lett., **98**, 125002 (2007)

[24] H. B. Cai, S. P. Zhu and X. T. He, *Effects of the imposed magnetic field on the production and transport of relativistic electron beams*, Phys. Plasmas, **20**, 072701 (2013)

[25] T. Johzaki, T. Taguchi, Y. Sentoku, A. Sunahara, H. Nagatomo, H. Sakagami, K. Mima, S. Fujioka and H. Shiraga, *Control of an electron beam using strong magnetic field for efficient core heating in fast ignition*, Nucl. Fusion, **55**, 5 (2015)

[26] T. Johzaki, H. Nagatomo, A. Sunahara, Y. Sentoku, H. Sakagami, M. Hata, T. Taguchi, K. Mima, Y. Kai, D. Ajimi, T. Isoda, T. Endo, A. Yogo, Y. Arikawa, S. Fujioka, H. Shiraga and H. Azechi, *Integrated simulation of magnetic-field-assist fast ignition laser fusion*, Plasma Phys. Control. Fusion, **59**, 014045 (2017)

[27] S. Sakata, S. Lee, H. Morita, T. Johzaki, H. Sawada, Y. Iwasa, K. Matsuo, K. F. F. Law, A. Yao, M. Hata, A. Sunahara, S. Kojima, Y. Abe, H. Kishimoto, A. Syuhada, T. Shiroto, A. Morace, A. Yogo, N. Iwata, M. Nakai, H. Sakagami, T. Ozaki, K. Yamanoi, T. Norimatsu, Y. Nakata, S. Tokita, N. Miyanaga, J. Kawanaka, H. Shiraga, K. Mima, H. Nishimura, M. Bailly-Grandvaux, J. J. Santos, H. Nagatomo, H. Azechi, R. Kodama, Y. Arikawa, Y. Sentoku and S. Fujioka, *Magnetized fast isochoric laser heating for efficient creation of ultra-high-energy-density states*, Nat. Commun., **9**, 3937 (2018)

[28] K. Matsuo, N. Higashi, N. Iwata, S. Sakata, S. Lee, T. Johzaki, H. Sawada, Y. Iwasa, K. F. F. Law, H. Morita, Y. Ochiai, S. Kojima, Y. Abe, M. Hata, T. Sano, H. Nagatomo, A. Sunahara, A. Morace, A. Yogo, M. Nakai, H. Sakagami, T. Ozaki, K. Yamanoi, T. Norimatsu, Y. Nakata, S. Tokita, J. Kawanaka, H. Shiraga, K. Mima, H. Azechi, R. Kodama, Y. Arikawa, Y. Sentoku and S. Fujioka, *Petapascal Pressure Driven by Fast Isochoric Heating with a Multipicosecond Intense Laser Pulse*, Phys. Rev. Lett., **124**, 035001 (2020)

[29] S. C. Wilks, A. B. Langdon, T. E. Cowan, M. Roth, M. Singh, S. Hatchett, M. H. Key, D. Pennington, A. MacKinnon and R. A. Snavely, *Energetic proton generation in ultra-intense laser-solid interactions*, Phys. Plasmas, **8**, 542 (2001)

[30] M. Passoni and M. Lontano, *Theory of Light-Ion Acceleration Driven by a Strong Charge Separation*, Phys. Rev. Lett., **101**, 115001 (2008)

[31] M. Passoni, C. Perego, A. Sgattoni, D. Batani, M. Passoni, C. Perego, A. Sgattoni and D. Batani, *Advances in target normal sheath acceleration theory*, Phys. Plasmas, **20**, 060701 (2013)

[32] A. Arefiev, T. Toncian and G. Fiksel, *Enhanced proton acceleration in an applied longitudinal magnetic field*, New J. Phys., **18**, 105011 (2016)

[33] A. E. Raymond, C. F. Dong, A. McKelvey, C. Zulick, N. Alexander, A. Bhattacharjee, P. T. Campbell, H. Chen, V. Chvykov, E. Del Rio, P. Fitzsimmons, W. Fox, B. Hou, A. Maksimchuk, C. Mileham, J. Nees, P. M. Nilson, C. Stoeckl, A. G. R. Thomas, M. S. Wei, V. Yanovsky, K. Krushelnick, and L. Willingale, *Relativistic-electron-driven magnetic reconnection in the laboratory*, Phys. Rev. E, **98**, 043207 (2018)

[34] S. X. Luan, W. Yu, F. Y. Li, D. Wu, Z. M. Sheng, M. Y. Yu and J. Zhang, *Laser propagation in dense magnetized plasma*, Phys. Rev. E, **94**, 053207 (2016)

[35] T. Sano, Y. Tanaka, N. Iwata, M. Hata, K. Mima, M. Murakami and Y. Sentoku, *Broadening of cyclotron resonance conditions in the relativistic interaction of an intense laser with overdense plasmas*, Phys. Rev. E, **96**, 043209 (2017)

[36] C. Liu, K. Matsuo, S. Ferri, H. K. Chung, S. Lee, S. Sakata, K. F. F. Law, H. Morita, B. Pollock, J. Moody and S. Fujioka, *Design of Zeeman spectroscopy experiment with magnetized silicon plasma generated in the laboratory*, High Energy Density Phys., **33**, 100710 (2019)

[37] K. Higuchi, D. B. Hamal and M. Higuchi, *Nonperturbative description of the butterfly diagram of energy spectra for materials immersed in a magnetic field*, Phys. Rev. B, **97**, 195135 (2018)

[38] R. S. Craxton, K. S. Anderson, T. R. Boehly, V. N. Goncharov, D. R. Harding, J. P. Knauer, R. L. McCrory, P. W. McKenty, D. D. Meyerhofer, J. F. Myatt, A. J. Schmitt, J. D. Sethian, R. W. Short, S. Skupsky, W. Theobald, W. L. Kruer, K. Tanaka, R. Betti, T. J. B. Collins, J. A. Delettrez, S. X. Hu, J. A. Marozas, A. V. Maximov, D. T. Michel, P. B. Radha, S. P. Regan, T. C. Sangster, W. Seka, A. A. Solodov, J. M. Soures, C. Stoeckl and J. D. Zuegel, *Direct-drive inertial confinement fusion: A review*, Phys. Plasmas, **22**, 110501 (2015)

[39] M. Tabak, J. Hammer, M. E. Glinsky, W. L. Kruer, S. C. Wilks, J. Woodworth, E. M. Campbell, M. D. Perry and R. J. Mason, *Ignition and high gain with ultrapowerful lasers*, Phys. Plasmas, **1**, 5 (1994)

[40] R. Kodama, P. A. Norreys, K. Mima, A. E. Dangor, R. G. Evans, H. Fujita, Y. Kitagawa, K. Krushelnick, T. Miyakoshi, N. Miyanaga, T. Norimatsu, S. J. Rose, T. Shozaki, K. Shigemori, A. Sunahara, M. Tampo, K. A. Tanaka, Y. Toyama, T. Yamanaka and M. Zepf, *Fast heating of ultrahigh-density plasma as a step towards laser fusion ignition*, Nature, **412**, 23 (2001):pp. 798–802

[41] W. Theobald, A. A. Solodov, C. Stoeckl, K. S. Anderson, F. N. Beg, R. Epstein, G. Fiksel, E. M. Giraldez, V. Y. Glebov, H. Habara, S. Ivancic, L. C. Jarrott, F. J. Marshall, G. McKiernan, H. S. McLean, C. Mileham, P. M. Nilson, P. K. Patel, F. Pérez, T. C. Sangster, J. J. Santos, H. Sawada, A. Shvydky, R. B. Stephens and M. S. Wei, *Time-resolved compression of a capsule with a cone to high density for fast-ignition laser fusion*, Nat. Commun., **5**, 5785 (2014)

[42] L. C. Jarrott, M. S. Wei, C. McGuffey, A. A. Solodov, W. Theobald, B. Qiao, C. Stoeckl, R. Betti, H. Chen, J. Delettrez, T. Döppner, E. M. Giraldez, V. Y. Glebov, H. Habara, T. Iwawaki, M. H. Key, R. W. Luo, F. J. Marshall, H. S. Mclean, C. Mileham, P. K. Patel, J. J. Santos, H. Sawada, R. B. Stephens, T. Yabuuchi and F. N. Beg, *Visualizing fast electron energy transport into laser-compressed high-density fast-ignition targets*, Nat. Phys., **12**, (2016):pp. 499–504

[43] S. C. Wilks, W. L. Kruer, M. Tabak and A. B. Langdon, *Absorption of ultra-intense laser pulses*, Phys. Rev. Lett., **69**, 9 (1992):pp. 1383–1386

[44] F. N. Beg, A. R. Bell, A. E. Dangor, C. N. Danson, A. P. Fews, M. E. Glinsky, B. A. Hammel, P. Lee, P. A. Norreys and M. Tatarakis, *A study of picosecond laser-solid interactions up to 1019W cm-2*, Phys. Plasmas, **4**, 2 (1997):pp. 447–457

[45] D. J. Strozzi, M. Tabak, D. J. Larson, L. Divol, A. J. Kemp, C. Bellei, M. M. Marinak and M. H. Key, *Fast-ignition transport studies: Realistic electron source, integrated particle-in-cell and hydrodynamic modeling, imposed magnetic fields*, Phys. Plasmas, **19**, 072711 (2012)

[46] J. Wang, Z. Q. Zhao, B. Zhu, Z. M. Zhang, L. H. Cao, W. M. Zhou and Y. Q. Gu, *Refluxed electrons direct laser acceleration in ultrahigh laser and relativistic critical density plasma interaction*, Phys. Plasmas, **22**, 013106 (2015)

[47] C. Goyon, B. B. Pollock, D. P. Turnbull, A. Hazi, L. Divol, W. A. Farmer, D. Haberberger, J. Javedani, A. J. Johnson, A. Kemp, M. C. Levy, B. Grant Logan, D. A. Mariscal, O. L. Landen, S. Patankar, J. S. Ross, A. M. Rubenchik, G. F. Swadling, G. J. Williams, S. Fujioka, K. F. Law and J. D. Moody, *Ultrafast probing of magnetic field growth inside a laser-driven solenoid*, Phys. Rev. E, **95**, 033208 (2017)

[48] R. P. Drake, *High-Energy-Density-Physics*, Springer, Chap. 1 Introduction to High-Energy-Density-Physics, p. 6

[49] M. R. Zaghloul, *A simple theoretical approach to calculate the electrical conductivity of nonideal copper plasma*, Phys. Plasmas, **15**, 042705 (2008)

[50] D.-K. Kim and I. Kim, *Calculation of ionization balance and electrical conductivity in nonideal aluminum plasma*, Phys. Rev. E, **68**, 056410 (2003)

[51] Z. Fu, L. Jia, X. Sun and Q. Chen, *Electrical conductivity of warm dense tungsten*, High Energy Density Phys., **9**, (2013):pp. 781–786

[52] M. Payne, M. Teter, D. Allan, T. Arias and J. Joannopoulos, *Iterative minimization techniques for ab initio total-energy calculations: molecular dynamics and conjugate gradients*, Rev. Mod. Phys., **64**, 4 (1992)

[53] D. Vanderbilt, *Soft self-consistent pseudopotentials in a generalized eigenvalue formalism*, Phys. Rev. B, **41**, 11 (1990)

[54] P. E. Blöchl, *Projector augmented-wave method*, Phys. Rev. B, **50**, 24 (1994)

[55] S. Mazevet, M. Torrent, V. Recoules and F. Jollet, *Calculations of the transport properties within the PAW formalism*, High Energy Density Phys., **6**, (2010):pp. 84–88

[56] D. J. Chadi and M. L. Cohen, *Special points in the brillouin zone*, Phys. Rev. B, **8**, 12 (1973):pp. 5747–5753

[57] H. J. Monkhorst and J. D. Pack, *Special points for Brillouin-zone integrations*, Phys. Rev. B, **13**, 12 (1976)

[58] F. Graziani, M. P. Desjarlais, R. Redmer and S. B. Trickey, *Frontiers and Challenges in Warm Dense Matter*, Springer, Progress in Warm Dense Matter and Planetary Physics, p. 209

[59] M. P. Desjarlais, J. D. Kress and L. A. Collins, *Electrical conductivity for warm, dense aluminum plasmas and liquids*, Phys. Rev. E, **66**, 025401 (2002)

[60] R. Matula, *Resistivity of Copper, Gold, Palladium, and Silver*, J. Phys. Chem. Ref. Data, **8**, 4 (1979)

[61] G. Kresse and J. Hafner, *Ab initio molecular dynamics for liquid metals*, Phys. Rev. B, **47**, 1 (1993):pp. 558–561

[62] G. Kresse and J. Furthmuller, *Efficient iterative schemes for ab initio total-energy calculations using a plane-wave basis set*, Phys. Rev. B, **54**, 16 (1996)

[63] S. Nosé, *A unified formulation of the constant temperature molecular dynamics methods*, J. Chem. Phys., **81**, 1 (1984):pp. 511–519

[64] X. Gonze, F. Jollet, F. Abreu Araujo, D. Adams, B. Amadon, T. Applencourt, C. Audouze, J. M. Beuken, J. Bieder, A. Bokhanchuk, E. Bousquet, F. Bruneval, D. Caliste, M. Côté, F. Dahm, F. Da Pieve, M. Delaveau, M. Di Gennaro, B. Dorado, C. Espejo, G. Geneste, L. Genovese, A. Gerossier, M. Giantomassi, Y. Gillet, D. R. Hamann, L. He, G. Jomard, J. Laflamme Janssen, S. Le Roux, A. Levitt, A. Lherbier, F. Liu, I. Lukačević, A. Martin, C. Martins, M. J. Oliveira, S. Poncé, Y. Pouillon, T. Rangel, G. M. Rignanese, A. H. Romero, B. Rousseau, O. Rubel, A. A. Shukri, M. Stankovski, M. Torrent, M. J. Van Setten, B. Van Troeye, M. J. Verstraete, D. Waroquiers, J. Wiktor, B. Xu, A. Zhou and J. W. Zwanziger, *Recent developments in the ABINIT software package*, Comput. Phys. Commun., **205**, (2016):pp. 106–131

[65] J. P. Perdew, K. Burke and M. Ernzerhof, *Generalized gradient approximation made simple*, Phys. Rev. Lett., **77**, 18 (1996):pp. 3865–3868

[66] M. Pozzo, M. P. Desjarlais and D. Alfè, *Electrical and thermal conductivity of liquid sodium from first-principles calculations*, Phys. Rev. B, **84**, 054203 (2011)

[67] B. Holst, V. Recoules, S. Mazevet, M. Torrent, A. Ng, Z. Chen, S. E. Kirkwood, V. Sametoglu, M. Reid and Y. Y. Tsui, *Ab initio model of optical properties of two-temperature warm dense matter*, Phys. Rev. B, **90**, 035121 (2014)

[68] A. Ng, P. Sterne, S. Hansen, V. Recoules, Z. Chen, Y. Y. Tsui and B. Wilson, *dc conductivity of two-temperature warm dense gold*, Phys. Rev. E, **94**, 033213 (2016)

[69] Dongxiao Liu, Wei Fan, Lianqiang Shan, Chao Tian, Bi Bi, Feng Zhang, Zongqiang Yuan, Weiwu Wang, Hongjie Liu, Lei Yang, Lingbiao Meng, Leifeng Cao, Weimin Zhou, and Yuqiu Gu. Ab initio simulations for expanded gold fluid in metal-nonmetal transition regime. Phys. Plasmas, Vol. 26, No. 12, 2019.

[70] I. M. Bespalov and A. Y. Polishchuk, *Method for calculating the degree of ionization and the thermal and electrical conductivity over a wide range of density and temperature*, Sov. Tech. Phys. Lett., **15**, (1989):pp. 39–41

[71] A. Kramida, Y. Ralchenko, J. Reader and N. A. Team, *NIST Atomic Spectra Database (version 5.5.6)*, National Institute of Standards and Technology, Gaithersburg, MD. (2018)

[72] O. Portugall, N. Puhlmann, H. U. Müller, M. Barczewski, I. Stolpe and M. Von Ortenberg, *Megagauss magnetic field generation in single-turn coils: New frontiers for scientific experiments*, J. Phys. D. Appl. Phys., **32**, (1999):pp. 2354–2366

[73] B. Albertazzi, J. Béard, A. Ciardi, T. Vinci, J. Albrecht, J. Billette, T. Burris-Mog, S. N. Chen, D. Da Silva, S. Dittrich, T. Herrmannsdörfer, B. Hirardin, F. Kroll, M. Nakatsutsumi, S. Nitsche, C. Riconda, L. Romagnagni, H. P. Schlenvoigt, S. Simond, E. Veuillot, T. E. Cowan, O. Portugall, H. Pépin and J. Fuchs, *Production of large volume, strongly magnetized laser-produced plasmas by use of pulsed external magnetic fields*, Rev. Sci. Instrum., **84**, 4 (2013)

[74] R. V. Shapovalov, G. Brent, R. Moshier, M. Shoup, R. B. Spielman and P. A. Gourdain, *Design of 30-T pulsed magnetic field generator for magnetized high-energy-density plasma experiments*, Phys. Rev. Accel. Beams, **22**, 080401 (2019)

[75] P. Hu, G. Y. Hu, Y. L. Wang, H. B. Tang, Z. C. Zhang and J. Zheng, *Pulsed magnetic field device for laser plasma experiments at Shenguang-II laser facility*, Rev. Sci. Instrum., **91**, 014703 (2020)

[76] L. Gao, H. Ji, G. Fiksel, W. Fox, M. Evans and N. Alfonso, *Ultrafast proton radiography of the magnetic fields generated by a laser-driven coil current*, Phys. Plasmas, **23**, 043106 (2016)

[77] B. J. Zhu, Y. T. Li, D. W. Yuan, Y. F. Li, F. Li, G. Q. Liao, J. R. Zhao, J. Y. Zhong, F. B. Xue, S. K. He, W. W. Wang, F. Lu, F. Q. Zhang, L. Yang, K. N. Zhou, N. Xie, W. Hong, H. G. Wei, K. Zhang, B. Han, X. X. Pei, C. Liu, Z. Zhang, W. M. Wang, J. Q. Zhu, Y. Q. Gu, Z. Q. Zhao, B. H. Zhang, G. Zhao and J. Zhang, *Strong magnetic fields generated with a simple open-ended coil irradiated by high power laser pulses*, Appl. Phys. Lett., **107**, 261903 (2015)

[78] X. X. Pei, J. Y. Zhong, Y. Sakawa, Z. Zhang, K. Zhang, H. G. Wei, Y. T. Li, Y. F. Li, B. J. Zhu, T. Sano, Y. Hara, S. Kondo, S. Fujioka, G. Y. Liang, F. L.

Wang and G. Zhao, *Magnetic reconnection driven by Gekko XII lasers with a Helmholtz capacitor-coil target*, Phys. Plasmas, **23**, 032125 (2016)

[79] M. Bailly-Grandvaux, J. J. Santos, C. Bellei, P. Forestier-Colleoni, S. Fujioka, L. Giuffrida, J. J. Honrubia, D. Batani, R. Bouillaud, M. Chevrot, J. E. Cross, R. Crowston, S. Dorard, J. L. Dubois, M. Ehret, G. Gregori, S. Hulin, S. Kojima, E. Loyez, J. R. Marquès, A. Morace, P. Nicolaï, M. Roth, S. Sakata, G. Schaumann, F. Serres, J. Servel, V. T. Tikhonchuk, N. Woolsey and Z. Zhang, *Guiding of relativistic electron beams in dense matter by laser-driven magnetostatic fields*, Nat. Commun., **9**, 102 (2018)

[80] T. Sano, M. Hata, D. Kawahito, K. Mima and Y. Sentoku, *Ultrafast wave-particle energy transfer in the collapse of standing whistler waves*, Phys. Rev. E, **100**, 053205 (2019)

[81] V. V. Korobkin and S. Motylev, *Laser method for producing strong magnetic fields*, Soviet Technical Physics Letters, **5**, 474 (1979)

[82] J. F. Seely, *Pulsed megagauss fields produced by laser-driven coils*, Applied Physics B, **31**, 1 (1983)

[83] H. Daido, F. Miki, K. Mima, M. Fujita, K. Sawai, H. Fujita, Y. Kitagawa, S. Nakai and C. Yamanaka, *Generation of a Strong Magnetic Field by an Intense CO2 Laser Pulse*, Phys. Rev. Lett., **56**, 8 (1986)

[84] P. Mora, *Thin-foil expansion into a vacuum*, Phys. Rev. E, **72**, 056401 (2005)

[85] G. Williams, S. Patankar, D. A. Mariscal, V. T. Tikhonchuk, J. Bude, C. Carr, C. Goyon, B. Norton, A. M. Rubenchik, G. F. Swadling, E. Tubman and J. Moody, *Laser intensity scaling of the magnetic field from a laser-driven coil target*, J. Appl. Phys., **17**, 083302 (2020)

[86] N. F. Chen, M. F. Kasim, L. Ceurvorst, N. Ratan, J. Sadler, M. C. Levy, R. Trines, R. Bingham and P. Norreys, *Machine learning applied to proton radiography of high-energy-density plasmas*, Phys. Rev. E, **95**, 043305 (2017)

[87] M. F. Kasim, L. Ceurvorst, N. Ratan, J. Sadler, N. Chen, A. Sävert, R. Trines, R. Bingham, P. N. Burrows, M. C. Kaluza and P. Norreys, *Quantitative shadowgraphy and proton radiography for large intensity modulations*, Phys. Rev. E, **95**, 023306 (2017)

[88] N. L. Kugland, D. D. Ryutov, C. Plechaty, J. S. Ross and H. S. Park, *Invited Article: Relation between electric and magnetic field structures and their proton-beam images*, Rev. Sci. Instrum., **83**, 101301 (2012)

[89] Y. Sentoku, T. E. Cowan, A. Kemp and H. Ruhl, *High energy proton acceleration in interaction of short laser pulse with dense plasma target*, Phys. Plasmas, **10**, 5 (2003)

[90] A. B. Zylstra, C. K. Li, H. G. Rinderknecht, F. H. Séguin and R. D. Petrasso, *Using high-intensity laser-generated energetic protons to radiograph directly driven implosions directly driven implosions*, Rev. Sci. Instrum., **83**, 013511 (2012)

[91] S. Atzeni and J. Meyer-Ter-Vehn, *The Physics of Inertial Fusion*, Oxford University Press Inc., Chap. 11 Beat-target interaction, pp. 389–396

[92] T. Sato, Y. Iwamoto, S. Hashimoto, T. Ogawa, T. Furuta, S. ichiro Abe, T. Kai, P. E. Tsai, N. Matsuda, H. Iwase, N. Shigyo, L. Sihver and K. Niita, *Features of Particle and Heavy Ion Transport code System (PHITS) version 3.02*, J. Nucl. Sci. Technol., **55**, 6 (2018):pp. 684–690

[93] L. Lancia, B. Albertazzi, C. Boniface, A. Grisollet, R. Riquier, F. Chaland, K. C. Le Thanh, P. Mellor, P. Antici, S. Buffechoux, S. N. Chen, D. Doria, M. Nakatsutsumi, C. Peth, M. Swantusch, M. Stardubtsev, L. Palumbo, M. Borghesi, O. Willi, H. Pépin and J. Fuchs, *Topology of megagauss magnetic fields and of heat-carrying electrons produced in a high-power laser-solid interaction*, Phys. Rev. Lett., **113**, 235001 (2014)

[94] Y. Abe, A. Morace, Y. Arikawa, S. Shokita, S. R. Mirfayzi, D. Golovin, K. Law, S. Fujioka, A. Yogo, S. Tojo and M. Nakai, *Dosimetric calibration of GAFCHROMIC HD-V2, MD-V3, and EBT3 film for dose ranges up to 30 MGy*, unpublished

[95] E. J. Tuohy, T. H. Lee and H. P. Fullerton, *Transient Resistance of Conductors*, IEEE Transactions on Power Apparatus and Systems, **87**, 094505 (1968)

[96] P. A. Gourdain, M. B. Adams, J. R. Davies and C. E. Seyler, *Axial magnetic field injection in magnetized liner inertial fusion*, Phys. Plasmas, **24**, 102712 (2017)

[97] J. Moody, A. Johnson, J. Javedani, E. Carroll, J. Fry, B. Kozioziemski, S. Kucheyev, B. Logan, B. Pollock, H. Sio, D. Strozzi, W. Stygar, V. Tang and S. Winters, *Transient magnetic field diffusion considerations relevant to magnetically assisted indirect drive inertial confinement fusion*, Phys. Plasmas, **27**, 112711 (2020)

[98] H. Morita, A. Sunahara, Y. Arikawa, H. Azechi and S. Fujioka, *Numerical analysis of pulsed magnetic field diffusion dynamics in gold cone target*, Phys. Plasmas, **25**, 094505 (2018)

[99] J. Clérouin, P. Noiret, P. Blottiau, V. Recoules, B. Siberchicot, P. Renaudin, C. Blancard, G. Faussurier, B. Holst and C. E. Starrett, *A database for equations of state and resistivities measurements in the warm dense matter regime*, Phys. Plasmas, **19**, 082702 (2012)

[100] V. Tikhonchuk, J. Santos and P. Korneev, *Generation of strong magnetic fields with lasers: from nano- to picoseconds*, Invited Talk at the 35th European Conference on Laser Interaction with Matter in Rethymno, Greece (2018)

[101] D. Forslund, J. Kindel and K. Lee, *Theory of Hot-Electron Spectra at High Laser Intensity*, Phys. Rev. Lett., **39**, 5 (1977):pp. 284–287

[102] S. Atzeni and J. Meyer-Ter-Vehn, *The Physics of Inertial Fusion*, Oxford University Press Inc., Chap. 10 Hot Dense Matter, pp. 332–335

[103] S. Christian, C. Andreas and F. Wolfgang, *Review of fdtd time-stepping schemes for efficient simulation of electric conductive media*, Microw. Opt. Technol. Lett., **25**, 1 (2000):pp. 16–21

[104] F. Schillaci, M. D. Marco, L. Giuffrida, S. Fujioka, Z. Zhang, G. Korn and D. Margarone, *Numerical simulations to model laser-driven coil-capacitor targets for generation of kilo-Tesla magnetic fields*, AIP Adv., **8**, 025103 (2018)

[105] M. Yousuf, P. C. Sahu and G. K. Rajan, *High-pressure and high-temperature electrical resistivity of ferromagnetic transition metals: Nickel and iron*, Phys. Rev. B, **34**, 11 (1986)

[106] V. Recoules and J. P. Crocombette, *Ab initio determination of electrical and thermal conductivity of liquid aluminum*, Phys. Rev. B, **72**, 104202 (2005)

[107] V. Vlček, N. De Koker and G. Steinle-Neumann, *Electrical and thermal conductivity of Al liquid at high pressures and temperatures from ab initio computations*, Phys. Rev. B, **85**, 184201 (2012)

[108] M. Borghesi, D. H. Campbell, A. Schiavi, M. G. Haines, O. Willi, A. J. MacKinnon, P. Patel, L. A. Gizzi, M. Galimberti, R. J. Clarke, F. Pegoraro, H. Ruhl and S. Bulanov, *Electric field detection in laser-plasma interaction experiments via the proton imaging technique*, Phys. Plasmas, **9**, 5 (2002)

[109] A. J. MacKinnon, P. K. Patel, M. Borghesi, R. C. Clarke, R. R. Freeman, H. Habara, S. P. Hatchett, D. Hey, D. G. Hicks, S. Kar, M. H. Key, J. A. King, K. Lancaster, D. Neely, A. Nikkro, P. A. Norreys, M. M. Notley, T. W. Phillips, L. Romagnani, R. A. Snavely, R. B. Stephens and R. P. Town, *Proton radiography of a laser-driven implosion*, Phys. Rev. Lett., **97**, 045001 (2006)

[110] K. L. Lancaster, S. Karsch, H. Habara, F. N. Beg, E. L. Clark, R. Freeman, M. H. Key, J. A. King, R. Kodama, K. Krushelnick, K. W. Ledingham, P. McKenna, C. D. Murphy, P. A. Norreys, R. Stephens, C. Stöeckl, Y. Toyama, M. S. Wei and M. Zepf, *Characterization of LiBe neutron yields from laser produced ion beams for fast neutron radiography*, Phys. Plasmas, **11**, 7 (2004):pp. 3404–3408

[111] S. Kar, K. Markey, P. T. Simpson, C. Bellei, J. S. Green, S. R. Nagel, S. Kneip, D. C. Carroll, B. Dromey, L. Willingale, E. L. Clark, P. McKenna, Z. Najmudin, K. Krushelnick, P. Norreys, R. J. Clarke, D. Neely, M. Borghesi and M. Zepf, *Dynamic control of laser-produced proton beams*, Phys. Rev. Lett., **100**, 105004 (2008)

[112] S. V. Bulanov and V. S. Khoroshkov, *Feasibility of Using Laser Ion Accelerators in Proton Therapy*, Plasma Phys. Reports, **28**, 5 (2002):pp. 493–496

[113] M. Roth, T. E. Cowan, M. H. Key, S. P. Hatchett, C. Brown, W. Fountain, J. Johnson, D. M. Pennington, R. A. Snavely, S. C. Wilks, K. Yasuike, H. Ruhl, F. Pegoraro, S. V. Bulanov, E. M. Campbell, M. D. Perry and H. Powell, *Fast ignition by intense laser-accelerated proton beams*, Phys. Rev. Lett., **86**, 3 (2001):pp. 436–439

[114] J. C. Fernández, J. J. Honrubia, B. J. Albright, K. A. Flippo, D. C. Gautier, B. M. Hegelich, M. J. Schmitt, M. Temporal and L. Yin, *Progress and prospects of ion-driven fast ignition*, Nucl. Fusion, **49**, 065004 (2009)

[115] I. J. Kim, K. H. Pae, I. W. Choi, C. L. Lee, H. T. Kim, H. Singhal, J. H. Sung, S. K. Lee, H. W. Lee, P. V. Nickles, T. M. Jeong, C. M. Kim and C. H. Nam, *Radiation pressure acceleration of protons to 93 MeV with circularly polarized petawatt laser pulses*, Phys. Plasmas, **23**, 070701 (2016)

[116] P. Antici, E. Boella, S. N. Chen, D. S. Andrews, M. Barberio, J. Böker, F. Cardelli, J. L. Feugeas, M. Glesser, P. Nicolaï, L. Romagnani, M. Scisciò, M. Starodubtsev, O. Willi, J. C. Kieffer, V. Tikhonchuk, H. Pépin, L. O. Silva, E. D. Humières and J. Fuchs, *Acceleration of collimated 45 MeV protons by collisionless shocks driven in low-density, large-scale gradient plasmas by a 1020W/cm2, 1 μm laser*, Sci. Rep., **7**, 16463 (2017)

[117] D. Wang, Y. Shou, P. Wang, J. Liu, C. Li, Z. Gong, R. Hu, W. Ma and X. Yan, *Enhanced proton acceleration from an ultrathin target irradiated by laser pulses with plateau ASE*, Sci. Rep., **8**, 2536 (2018)

[118] A. Higginson, R. J. Gray, M. King, R. J. Dance, S. D. Williamson, N. M. Butler, R. Wilson, R. Capdessus, C. Armstrong, J. S. Green, S. J. Hawkes, P. Martin, W. Q. Wei, S. R. Mirfayzi, X. H. Yuan, S. Kar, M. Borghesi, R. J. Clarke, D. Neely and P. McKenna, *Near-100 MeV protons via a laser-driven transparency-enhanced hybrid acceleration scheme*, Nat. Commun., **9**, 724 (2018)

[119] H. Schwoerer, S. Pfotenhauer, O. Jäckel, K.-U. Amthor, B. Liesfeld, W. Ziegler, R. Sauerbrey, K. W. D. Ledingham and T. Esirkepov, *Laser-plasma acceleration of quasi-monoenergetic protons from microstructured targets*, Nature, **439**, (2006):pp. 445–448

[120] O. Klimo, J. Psikal, J. Limpouch, J. Proska, F. Novotny, T. Ceccotti, V. Floquet and S. Kawata, *Short pulse laser interaction with micro-structured targets: Simulations of laser absorption and ion acceleration*, New J. Phys., **13**, 053028 (2011)

[121] M. Blanco, C. Ruiz and M. Vranic, *Table-top laser-based proton acceleration in nanostructured targets*, New J. Phys., **19**, 033004 (2017)

[122] A. Yogo, K. Mima, N. Iwata, S. Tosaki, A. Morace, Y. Arikawa, S. Fujioka, T. Johzaki, Y. Sentoku, H. Nishimura, A. Sagisaka, K. Matsuo, N. Kamitsukasa, S. Kojima, H. Nagatomo, M. Nakai, H. Shiraga, M. Murakami, S. Tokita, J. Kawanaka, N. Miyanaga, K. Yamanoi, T. Norimatsu, H. Sakagami, S. V. Bulanov, K. Kondo and H. Azechi, *Boosting laser-ion acceleration with multi-picosecond pulses*, Sci. Rep., **7**, 42451 (2017):p. 10

[123] A. Morace, N. Iwata, Y. Sentoku, K. Mima, Y. Arikawa, A. Yogo, A. Andreev, S. Tosaki, X. Vaisseau, Y. Abe, S. Kojima, S. Sakata, M. Hata, S. Lee, K. Matsuo, N. Kamitsukasa, T. Norimatsu, J. Kawanaka, S. Tokita, N. Miyanaga, H. Shiraga, Y. Sakawa, M. Nakai, H. Nishimura, H. Azechi, S. Fujioka and R. Kodama, *Enhancing laser beam performance by interfering intense laser beamlets*, Nat. Commun., **10**, 2995 (2019)

[124] J. J. Santos, M. Bailly-Grandvaux, M. Ehret, A. V. Arefiev, D. Batani, F. N. Beg, A. Calisti, S. Ferri, R. Florido, P. Forestier-Colleoni, S. Fujioka, M. A. Gigosos, L. Giuffrida, L. Gremillet, J. J. Honrubia, S. Kojima, P. Korneev, K. F. Law, J. R. Marquès, A. Morace, C. Mossé, O. Peyrusse, S. Rose, M. Roth, S. Sakata, G. Schaumann, F. Suzuki-Vidal, V. T. Tikhonchuk, T. Toncian, N. Woolsey and Z. Zhang, *Laser-driven strong magnetostatic fields with applications to charged beam transport and magnetized high energy-density physics*, Phys. Plasmas, **25**, 056705 (2018)

[125] K. Weichman, J. J. Santos, S. Fujioka, T. Toncian and A. V. Arefiev, *Generation of focusing ion beams by magnetized electron sheath acceleration*, Sci. Rep., **10**, 18966 (2020)

[126] A. V. Arefiev, A. P. Robinson and V. N. Khudik, *Novel aspects of direct laser acceleration of relativistic electrons*, J. Plasma Phys., **81**, 475810404 (2015)

[127] W. Priedhorsky, D. Lier, R. Day and D. Gerke, *Hard-X-ray measurements of 10.6-μm laser-irradiated targets*, Phys. Rev. Lett., **47**, 23 (1981):pp. 1661–1664

[128] H. K. Chung, M. H. Chen, W. L. Morgan, Y. Ralchenko and R. W. Lee, *Generalized population kinetics and spectral model for rapid spectroscopic analysis for all elements*, High Energy Density Physics, **1**, (2005)

[129] S. Egashira *et al.*, (private communication)

[130] R. J. Zollweg and R. W. Liebermann, *Electrical conductivity of nonideal plasmas*, J. Appl. Phys., **62**, 9 (1987):pp. 3621–3627

ANNOTATION:

[131] M. R. Zaghloul, M. A. Bourham and J. M. Doster, *Energy-averaged electron–ion momentum transport cross section in the Born Approximation and Debye–Huckel potential*, Phys. Lett. A, **266**, (2000):pp. 34–40

[132] R. M. More, *Pressure Ionization, Resonances, and the Continuity of Bound and Free States*, Adv. At. Mol. Phys., **21**, (1985):pp. 305–356

ANNOTATION:

[133] M. P. Desjarlais, *Practical Improvements to the Lee-More Conductivity Near the Metal-Insulator Transition*, Contrib. to Plasma Phys., **41**, 2-3 (2001):pp. 267–270

[134] M. R. Zaghloul, M. A. Bourham and J. M. Doster, *Simple formulation and solution strategy of the Saha equation for ideal and nonideal plasmas*, J. Phys. D. Appl. Phys., **33**, 977 (2000)

[135] Y. T. Lee and R. M. More, *An electron conductivity model for dense plasmas*, Phys. Fluids, **27**, 1273 (1984)

[136] M. R. Zaghloul, *On the Calculation of the Electrical Conductivity of Hot Dense Nonideal Plasmas*, Plasma Phys. Reports, **46**, 5 (2020):pp. 574–586

[137] D. Bednarczyk and J. Bednarczyk, *The approximtion of the Fermi-Dirac integral F1/2*, Phys. Lett., **64**, 4 (1978):pp. 409–410

[138] X. Aymerich-Humet, F. Serra-Mestres and J. Millán, *An analytical approximation for the Fermi-Dirac integral F3/2(η)*, Solid State Electron., **24**, 10 (1981):pp. 981–982

[139] K. Widmann, T. Ao, M. E. Foord, D. E. Price, A. D. Ellis, P. T. Springer, and A. Ng, *Single-State Measurement of Electrical Conductivity of Warm Dense Gold*, Phys. Rev. Lett., **92**, 12 (2004)

[140] Y. Ping, D. Hanson, I. Koslow, T. Ogitsu, D. Prendergast, E. Schwegler, G. W. Collins, and A. Ng, *Dielectric function of warm dense gold*, Phys. Plasmas, **15**, 056303 (2008)

[141] Z. Chen, B. Holst, S. E. Kirkwood, V. Sametoglu, M. Reid, Y. Y. Tsui, V. Recoules, and A. Ng, *Evolution of ac Conductivity in Nonequilibrium Warm Dense Gold*, Phys. Rev. Lett., **110**, 135001 (2013)